Technische Universität München

Max-Planck-Institut für Physik
(Werner-Heisenberg-Institut)

Study of a DEPFET Vertex Detector and of Supersymmetric Smuons at the ILC

Xun Chen

Vollständiger Abdruck der von der Fakultät für Physik
der Technischen Universität München
zur Erlangung des akademischen Grades eines
Doktors der Naturwissenschaften (Dr. rer. nat.)
genehmigten Dissertation.

Vorsitzender:		Univ.-Prof. Dr. M. Ratz
Prüfer der Dissertation:	1.	Hon.-Prof. A. C. Caldwell, PhD
	2.	Univ.-Prof. Dr. R. Krücken

Die Dissertation wurde am 27.10.2008
bei der Technischen Universität München eingereicht und
durch die Fakultät für Physik am 21.01.2009 angenommen.

In memory of my mother and grandmother

Abstract

This thesis is devoted to the study of the performance of a pixel vertex detector based on DEPFET technology at the International Linear Collider (ILC). The ILC is the proposed next generation e^+e^- collider to explore the physics at the Terascale. At the ILC with its well-defined initial state of collisions, possible discoveries at the Large Hadron Collider can be verified and studied more accurately. It is expected that the precision measurements of the ILC will answer many fundamental questions about the universe, such as the generation of particle masses and the origin of electroweak spontaneous symmetry breaking. The ambitious physics goals present challenges to the ILC detectors. Several detector concepts have been proposed in recent years. A crucial device for all these concepts is the pixel vertex detector. It provides precise impact parameter information of charged particles, jet flavor tagging and improves overall tracking efficiency. To meet the requirements of the ILC environment, the vertex detector will be arranged in a concentric multi-layer array around the interaction point to cover as large a solid angle as possible. Endcap disks are considered in some designs. Silicon pixel sensor technologies must be employed to provide excellent point resolution. The DEPFET technology, which integrates the first level of amplification into a depleted silicon bulk, is one of the promising candidates. The DEPFET sensor is very sensitive with a high signal-to-noise ratio. Power consumption is minimized due to the internal storage of signal charges. The good radiation tolerance makes it capable of working close to the interaction point.

In this thesis, we discuss the detailed simulation of the DEPFET vertex detector, following the general vertex detector layout proposed by the TESLA collaboration. The simulation is used to evaluate the impact parameter resolution. We also discuss the DEPFET test beam analysis on two-track resolution. The whole analysis procedures, ranging from readout of raw data to tracking, are described in detail. At last, we discuss the analysis of right-handed smuon pair production at the ILC with full simulation and reconstruction. The decay channel of smuon, $\tilde{\mu}_R^{\pm} \to \mu^{\pm}\tilde{\chi}_1^0$ allows the precise determination of $m_{\tilde{\mu}_R}$ through the energy spectrum of final muons. The ILC vertexing and tracking system is crucial for this analysis. In addition, the scalar nature of the smuon can be revealed by studying its angular distribution. These studies show that the DEPFET vertex detector will well meet the requirement posed by the ILC physics program.

Contents

Chapter 1

Introduction

The standard model of elementary particle physics provides the best description of nature at current stage. However, some very fundamental questions remain unanswered. The incompleteness of the standard model itself and observations of recent astrophysical experiments indicate the existence of new physics beyond the standard model. A number of theories have been proposed to describe the new physics. Most of their predictions can be tested by the high energy experiments at the Terascale, i.e. at energies around and above 1 TeV (10^{12} eV). The Large Hadron Collider (LHC), that has just started operation at CERN, will explore the physics at the Terascale for the first time. To complement the discoveries of the LHC, the International Linear Collider (ILC), an electron-positron collider, has been proposed. Benefitting from the well-defined initial beam energies, luminosity and polarization, and the low backgrounds, the ILC experiments will achieve unprecedented accuracy to verify and extend the discoveries of the LHC and give us a deeper insight into nature.

A next generation of linear electron-positron collider operated at the center-of-mass energy of a few hundred GeV to 1 TeV has been proposed since the 1980s. In 2004, the ILC project has started officially, based on three existing regional linear collider projects, i.e. the Next Linear Collider (NLC) [1], the Global Linear Collider (GLC) [2] and the Teraelectronvolt Energy Superconducting Linear Accelerator (TESLA) [3]. The superconducting radio-frequency (SCRF) technology has been chosen by the International Technology Recommendation Panel (ITRP) for the acceleration of electrons and positrons [4]. The ILC accelerator has been designed to meet the basic parameters required for the planned physics program [5]. The ILC will be operated up to a maximum center-of-mass energy of $\sqrt{s} = 500$ GeV and a peak luminosity of $2 \times 10^{34}\mathrm{cm}^{-2}\mathrm{s}^{-1}$ in the first stage. The integrated luminosity is required to be 500 fb^{-1} within the first four years during the phase of operation at 500 GeV. Both electron and positron beams are polarized. Beam energy and polarization must be stable. Subsequently, an energy upgrade to $\sqrt{s} \sim 1$ TeV is foreseen.

The ILC baseline configuration has been summarized in the ILC Reference Design Report (RDR) [6] released in 2007. The overall length of the ILC complex is around 31 km. One interaction point is designed to be shared by two detectors via a "push-pull" system.

The physics goals present a challenge to the designs and technologies of detectors at the ILC. Three detector concepts have been proposed and studied so far [7,8,9], applying different structures and technologies. A pixel vertex detector is required by all these concepts. The vertex detector is used to provide accurate impact parameter determination, excellent vertex resolution, jet flavor tagging and to improve the overall tracking performance. The physics program requires the vertex detector efficiency, angular coverage and impact parameter resolution to be raised beyond the current state of the art. To meet the requirements, new pixel sensor technologies are proposed and investigated. The concept of DEPFET (DEPleted Field Effect Transistor) pixel [10] is one of them. By integrating the first stage of amplification into a fully depleted bulk, the DEPFET sensor has a high signal-to-noise ratio with minimum power consumption. Also a high readout rate can be achieved for the DEPFET sensor matrix. These features make DEPFET an ideal candidate for the ILC vertex detector.

In this thesis, we study the performance of a pixel vertex detector based on DEPFET technology at the ILC, with the detailed simulation of the DEPFET detector, the analysis of DEPFET test beam data, and the analysis of smuon production at the ILC with full simulation.

The thesis is organized as follows: In chapter 2 a brief overview of the physics to be explored at the ILC is given. In chapter 3, we introduce the widely accepted particle flow algorithm and three detector concepts for ILC. Chapter 4 is devoted to the DEPFET technology. The principle of DEPFET, design of DEPFET ladders for the application at the ILC, steering and readout electronics and radiation tolerance are introduced. An overview of the software tools used in the simulation and optimization of a DEPFET pixel vertex detector at the ILC is given in chapter 5. In chapter 6, the detailed simulation of the DEPFET pixel vertex detector in two detector concepts is discussed. A study on the impact parameter resolution is performed. The DEPFET test beam analysis on two-track resolution is discussed in chapter 7. The analysis starts from the processing of raw data. Hits are found after the subtraction of pedestals and calculation of noise. Tracks are reconstructed by using a rough model after the pre-alignment. Reconstructed track candidates are used in the final analysis of two-track resolution. As one possible application of vertexing and tracking at the ILC, the production of right-handed scalar muon is analyzed and discussed in chapter 8 based on full simulation. The masses of right-handed smuons and neutralinos are determined by the muon energy spectrum. The angular distribution of smuons is studied.

The detailed parameters used for the simulation of the DEPFET vertex detector is given in appendix A. Appendix B is a "How-to" about using ISAJET in a PYTHIA based event generator. We discuss the solution of the intersection of two cones in detail in appendix C, which are required in the analysis of angular distribution of smuons.

Chapter 2

Physics at the ILC

Currently, the Standard Model (SM) is the most successful theory in particle physics. It incorporates all the elementary particles observed so far, and describes their electromagnetic, strong and weak interactions. The predictions of the SM have been tested by a large variety of high energy experiments to an unprecedented accuracy. But the hypothetical Higgs boson [11], which plays an important role in the spontaneous electroweak symmetry breaking (EWSB) and the generation of masses, is not observed yet. The SM also leaves some fundamental questions unanswered. For instance, it does not incorporate gravity. It does not explain what the dark matter is, which dominates over visible matter in the universe and was confirmed by recent astrophysical observations. It also lacks an explanation of the masses of neutrinos. In addition, the huge hierarchy between the electroweak scale and the Planck scale cannot be explained within the framework of the SM [12]. All these problems indicate the existence of new physics beyond the SM. Such new physics usually introduces new interactions, new particles or new symmetries, which are supposed to come into play at the Terascale, a scale that will be probed by the Large Hadron Collider at CERN for the first time. The emphasis of the LHC is on discoveries of new particles due to its high center-of-mass energy. The ILC, with its precision measurements, is essential for understanding the new physics at the Terascale.

Possible discovery scenarios at the ILC have been discussed in detail in the ILC Reference Design Report (RDR) [13]. The interplay between the LHC and ILC will be important for the discovery of new physics and, in particular, the disentangling of different models [14]. For instance, the study of the hypothetical Higgs boson is one of the most important tasks for both colliders. It is believed that the LHC is very likely to discover the Higgs boson if it exists within the energy range of a few hundred GeV. If a Higgs-like particle is discovered by the LHC, the ILC will measure its properties precisely to verify its true identity. The measurements of ILC will determine its mass, spin, parity, decay channels, and couplings to other particles. The precise determination of the Higgs properties is crucial to reveal the mechanism that generates the particle masses. If no Higgs-like particles are observed at the LHC, this might be due to one of the following two reasons: 1. The Higgs boson exists but is missed by the LHC; 2. There is no Higgs. The precision measurements carried out at the

ILC will be capable to distinguish between the two scenarios and give the right answer.

In the following, an overview of the physics to be explored at the ILC is given with emphasis on Higgs physics and supersymmetry. More detailed discussions can be found in the ILC RDR and the report of the LHC/LC study group [14].

2.1 Higgs physics

The spontaneous breaking of the electroweak symmetry is realized in the SM by the Higgs mechanism [11], where the neutral component of a complex isospin doublet acquires a non-vanishing vacuum expectation value. This results in a physical scalar particle after the symmetry breaking, i.e. the Higgs boson. Gauge bosons and fermions acquire masses through coupling to the Higgs boson. The Higgs boson is the only missing particle of the SM. Actually, even if the Higgs mechanism is confirmed to be the origin of particle masses, the number of Higgs particles is still to be determined. For instance, the one doublet of two scalar fields introduced by the minimal standard model leaves one Higgs boson, while the minimal supersymmetric extension of the SM with two doublets contains two CP-even neutral Higgs bosons, a CP-odd Higgs boson and a pair of charged Higgs particles. The search for Higgs bosons is an important task of present and future particle colliders. Precise determination of their properties is essential to understand the origin of the EWSB.

2.1.1 The Higgs boson in the SM

In the standard model, the one doublet with two complex scalar fields leaves one massive Higgs boson with $J^{PC} = 0^{++}$ after the EWSB [11,15]. The mass of the Higgs boson is the only free parameter of the model, however, experiments and theories give some constraints on this parameter. The current lower limit of the Higgs mass is given as $M_H \gtrsim 114.4$ GeV[1] at 95% confidence level by direct search at the LEP experiments [16]. The combined measurements from the LEP experiments also give upper limit of $M_H = 144$ GeV at 95% confidence level by using the updated top quark mass [17]. The fitting results of M_H are illustrated in Fig. 2.1. The accurate data of LEP, SLC and Tevatron provide an indirect limitation to M_H [18]. On the theoretical side, Higgs mass $M_H \lesssim 700$ GeV is required to preserve unitarity [19]. Another constraint comes from the quartic Higgs self-coupling, which at the scale M_H is fixed by M_H and grows logarithmically with the energy scale. If M_H is small, the energy cut-off Λ at which the coupling grows beyond any bound and new phenomena should occur, is large; if M_H is large, the cut-off Λ is small. The requirement of $M_H \lesssim \Lambda$, gives a triviality upper bound for the Higgs mass.

At the ILC, the main production mechanisms of the SM Higgs boson are the Higgs-strahlung $e^+e^- \to ZH \to f\bar{f}H$ [19, 20] and the WW fusion $e^+e^- \to \bar{\nu}_e\nu_e H$ [21] processes as shown in Fig. 2.2(a). The Higgs-strahlung process, which cross section scales as $1/s$, dominates at low energies while the WW fusion process becomes more important at higher energy as

[1] The natural units $\hbar = c = 1$ are used throughout in this thesis.

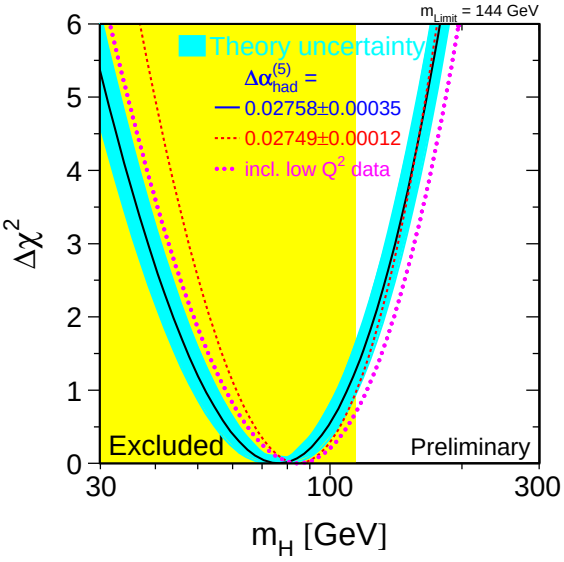

Figure 2.1: The $\Delta\chi^2 = \chi^2 - \chi^2_{min}$ vs. M_H curve obtained by the LEP experiments [17]. The line is the fit result using all high-Q^2 data. The blue band represents the estimated theoretical error.

its cross section rises like $\log(s/M_H^2)$. The second diagram of Fig. 2.2(a) and 2.2(b) show the sub-leading Higgs production channels, including the ZZ fusion $e^+e^- \to e^+e^-H$ [21], associated production with top quarks $e^+e^- \to t\bar{t}H$ [22] and double Higgs production [23] in the Higgs-strahlung $e^+e^- \to ZHH$ and fusion $e^+e^- \to \bar{\nu}\nu HH$ processes. These channels have smaller production rates but are useful for the study of Higgs properties.

In the SM, the profile of the Higgs boson depends on its mass [15]. If $M_H \lesssim 140$ GeV, the main decay mode is the decay into $b\bar{b}$ pairs with a branching ratio of $\mathcal{O}(80\%)$. If M_H is larger, the Higgs boson mainly decays into $WW^{(*)}$ and $ZZ^{(*)}$ pairs, with one of the gauge bosons being virtual if below the WW threshold.

The Higgs mass can be determined in a model-independent way through the Higgs-strahlung process by calculating the l^+l^- recoil mass in $e^+e^- \to ZH \to Hl^+l^-$. This even works for invisible Higgs decays. For a precise mass determination, further statistics can be gained by including hadronic Z decays. The $b\bar{b}q\bar{q}$ and $b\bar{b}ll$ channels can be used to reconstruct the Higgs mass directly as the decay $H \to b\bar{b}$ is dominant for low M_H, i.e. $M_H \lesssim 140$ GeV. The ILC vertex detector will provide excellent b-tagging efficiency for this study. The spin and parity of the SM Higgs boson can be determined through the Higgs-strahlung process. By scanning the cross section near threshold, the discovering of the relation $\sigma(e^+e^- \to HZ) \propto \lambda^{1/2}$ where $\lambda = s - (M_z + M_H)^2$, would rule out $J^P = 0^-, 1^-, 2^-$ and higher spin $3^\pm, \cdots$, because the cross section rises with higher power of $\lambda^{1/2}$. The possibilities of $1^+, 2^+$ can be ruled out by studying angular correlations [24]. The CP nature of the Higgs boson can be tested by measuring the its couplings to fermions. The decay channel $H \to \tau^+\tau^-$ for $M_H \lesssim 140$ GeV

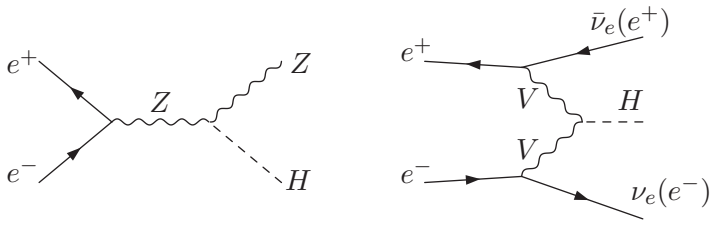

(a) Higgs-strahlung(left), WW fusion and ZZ fusion (right).

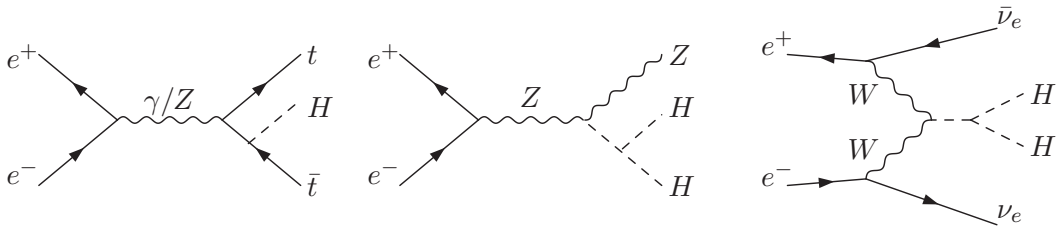

(b) Associated Higgs production with top quarks (left), double Higgs production in Higgs-strahlung (middle) and fusion (right).

Figure 2.2: The production of SM Higgs boson at the ILC.

is suggested [25]. Higgs couplings to gauge bosons can be determined by measuring the production cross sections in Higgs-strahlung and fusion. The Higgs decay branching ratios to heavy quarks and $\tau^+\tau^-$ can be measured so that the prediction of the Higgs mechanism can be tested. The vertex detector is vital in tagging H decays to b and c quarks and τ's. The Higgs coupling constants, such as the Higgs Yukawa coupling and trilinear Higgs coupling, can be determined in a model-independent way. That is crucial to understand the generation of mass and useful to explore physics beyond the SM.

2.1.2 Higgs bosons in theories beyond the SM

Two isospin doublets with opposite hypercharge are required to cancel anomalies and give mass to up and down fermions separately by the minimal supersymmetric extension of the SM (MSSM), which will be introduced in section 2.2. Five physical Higgs bosons are left after the EWSB [26]. Two of them, h^0 and H^0, are CP-even, the one denoted by A^0 is CP-odd, and the other two, $H^\pm$ are charged. The coupling of the CP-odd Higgs boson A^0 to down (up) type fermions is (inversely) proportional to $\tan\beta$, which is the ratio of the vacuum expectation values of the two Higgs doublets. The down (up) coupling of both the CP-even Higgs bosons H^0 and h^0 are enhanced (suppressed) at large $\tan\beta$ compared to the SM. If M_{A^0} is large, the mass of the lightest h^0 boson reaches its upper limit and its coupling to fermions and gauge bosons are SM-like. The ILC experiment is capable to distinguish it from the SM Higgs boson by determining its properties accurately. The decay patterns of

MSSM Higgs bosons [26] are more complicated than that of the SM Higgs boson and depend on $\tan\beta$ and Higgs masses. The h^0 boson mainly decays into fermion pairs since its mass is smaller than 140 GeV [27]. The H^0 and A^0 bosons also mainly decay into fermion pairs in general, except for the situation when H^0 is SM-like. The branching ratios of the three neutral bosons to $b\bar{b}$ are of the order of $\sim 90\%$ for large $\tan\beta$ value. At large masses, the top decay channels for H^0 and A^0 open up, while these modes are suppressed for large $\tan\beta$. Heavier H^0 can decay into gauge boson or h^0 boson pairs and heavy A^0 can decay into $h^0 Z$ final state. The charged Higgs particles decay into fermion pairs, mainly $t\bar{b}$ and $\tau\nu_\tau$. The h^0 and H^0 bosons can be produced in Higgs-strahlung and fusion processes at the ILC. Another important process for the production of neutral Higgs particles is $e^+e^- \to A^0 + h^0/H^0$. The charged Higgs bosons can be produced in $e^+e^- \to H^+H^-$ processes.

The h^0 can be detected in the entire range of the MSSM parameter space through the Higgs-strahlung, WW-fusion and associated production with A^0. All the MSSM Higgs bosons can be discovered if their masses are less than the beam energy. A precision of the order of 0.2% on the H^0 and A^0 masses is expected [13]. Using a complete scan of the MSSM $[M_A, \tan\beta]$ parameter space, it can be shown that the h^0 Higgs in 95% of the MSSM solutions can be distinguished from the SM case for $M_A \lesssim 600$ GeV [3].

The Higgs sector may be more complex for other extensions of SUSY. Additional Higgs bosons will emerge with new fields. Nevertheless, one Higgs boson with mass below 200 GeV and significant couplings to gauge bosons should exist in a general SUSY model [28]. It can be detected in the Higgs-strahlung process at the ILC with a center-of-mass energy $\sqrt{s} \gtrsim 350$ GeV.

The discovery potential of Higgs bosons in non-SUSY scenarios beyond the SM at the ILC is also discussed in the ILC RDR. The ILC will be a valuable tool to explore the mechanism of EWSB in these scenarios [13].

2.2 Supersymmetry

As one of the most promising theoretical extensions of the standard model (SM), supersymmetry (SUSY) [29] predicts the existence of a supersymmetric partner for each known particle that differs in spin by $\frac{1}{2}$ [30]. If they exist, some of these partners are expected to be produced and found in the energy range of the ILC. The most economical globally supersymmetric extension of the SM is the minimal supersymmetric Standard Model (MSSM) [31], which introduces the minimal set of new particles by only associating each known boson with one new fermion and each known fermion with one new boson. At least two complex Higgs doublets are needed to give mass to fermions in MSSM.

A discrete symmetry called R-parity [32] is introduced and usually assumed to be preserved in MSSM. All the SM particles have the R-parity number $+1$, or R-even, while all the superpartners have the R-parity number -1, or R-odd. The conservation of R-parity leads to two consequences: the supersymmetric particles are created in pairs, and the lightest supersymmetric particle (LSP) is stable.

Since super partners are not observed at current achieved energies, SUSY must be broken explicitly or spontaneously. The most common mechanism of the breaking of SUSY at low energy in MSSM is called the "hidden sector one". In this scenario, there are two sectors. The visible one contains the usual matter, and the "hidden" sector contains the field which leads to the breaking of supersymmetry. The two sectors exchange some fields called "messengers", which mediate SUSY breaking from the hidden sector to the visible one. The minimal supergravity (mSUGRA) scenario [33], in which the gravity field acts as the mediation field, is widely used as the benchmark scenario in analyses.

The mSUGRA model has only four free parameters and one sign:

$$m_0, m_{1/2}, A_0, \tan\beta, sign(\mu),$$

where m_0 is the scalar (sfermion and Higgs) mass, $m_{1/2}$ is the gaugino (bino, wino and gluino) mass, and A_0 is the trilinear scalar interaction. They are all defined at the GUT scale. $\tan\beta$ is the ratio of the vacuum expectation values (v.e.v) of the two Higgs doublets. μ is the supersymmetric Higgs mass parameter. All the soft SUSY-breaking parameters at the weak scale are obtained via renormalization group equations (RGE). The masses of the physical states, including the neutralinos $\tilde{\chi}^0_{1,2,3,4}$, the charginos $\tilde{\chi}^\pm_{1,2}$, the scalar partners $\tilde{f}_{1,2}$ of the SM fermions and the five MSSM Higgs bosons h^0, H^0, A^0 and $H^\pm$, are obtained by diagonalyzing the relevant mass matrices. The LSP is the lightest neutralino $\tilde{\chi}^0_1$.

Scanning over the whole parameter space in phenomenological studies is a formidable task. For this reason, different sets of benchmark points and parameter lines in the MSSM parameter space corresponding to different scenarios in the search for SUSY are proposed. For example, the "Snowmass Points and Slopes" (SPS) presented [34] in 2001 are widely used. The SPS1a point benchmark follows the mSUGRA scenario. It has the following input parameters,

$$m_0 = -A_0 = 100 \text{ GeV}, \ m_{1/2} = 250 \text{ GeV}, \ \tan\beta = 10 \text{ and } \mu > 0,$$

and is used in the studies of right-handed scalar muon production discussed in chapter 8. The SUSY particle mass spectrum at the SPS1a point is given in Fig. 2.3 [34]. The production cross sections for various SM and SUSY processes as a function of the center-of-mass energy in this scenario are also given in the right of Fig. 2.3.

If the supersymmetrical particles are produced at the ILC, their masses, spins and parities, decay widths and branching ratios can be measured precisely. These measurements can verify their identities and be used to reconstruct the low-energy soft SUSY-breaking parameters in a model independent way.

The charginos $\tilde{\chi}^\pm_{1,2}$ can be produced in pairs, $e^+e^- \to \tilde{\chi}^+_i\tilde{\chi}^-_j$ via s-channel γ/Z and t-channel sneutrino exchange. The light charginos $\tilde{\chi}^\pm_1$ decay into fermion pairs and neutralinos, $\tilde{\chi}^\pm_1 \to f\bar{f}'\tilde{\chi}^0_1$. Heavier ino states decay into lighter charginos and neutralinos. The chargino masses can be determined in the process $e^+e^- \to \tilde{\chi}^+_1\tilde{\chi}^-_1 \to l^\pm\nu q\bar{q}'\tilde{\chi}^0_1\tilde{\chi}^0_1$. The pair production of neutralinos, $e^+e^- \to \tilde{\chi}^0_i\tilde{\chi}^0_j$, proceeds via s-channel Z boson and t- and u- channel $\tilde{e}_{L,R}$ exchanges. Because the $\tilde{\chi}^0_2$ decays into $f\bar{f}\tilde{\chi}^0_1$, the process $e^+e^- \to \tilde{\chi}^0_2\tilde{\chi}^0_1 \to l^+l^-\tilde{\chi}^0_1\tilde{\chi}^0_1$ will be used to determine the mass difference of the two neutralinos. Heavier neutralinos and

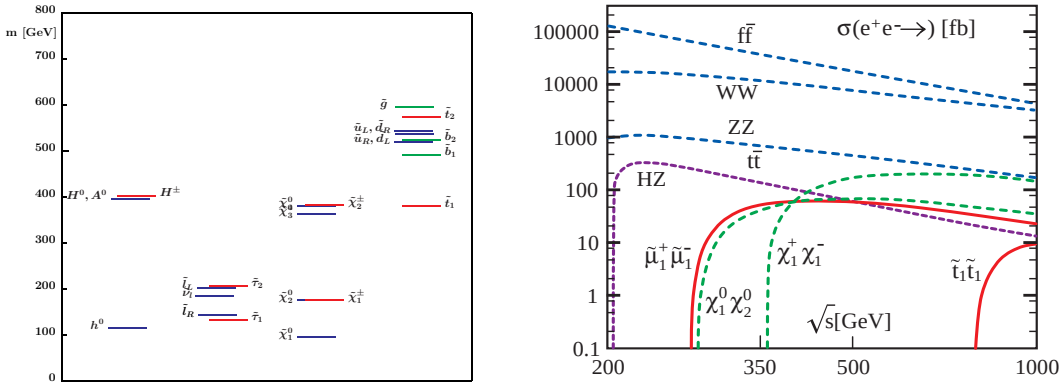

Figure 2.3: The spectrum of SUSY and Higgs particle at the benchmark SPS1a point (left) and the production cross sections for different processes in e^+e^- collisions (right) in this scenario.

charginos are not accessible in pair production at the ILC in the SPS1a and many other SUSY scenarios unless the ILC center-of-mass energy is upgraded to 1 TeV.

The sleptons, $\tilde{e}^\pm_{L,R}$, $\tilde{\mu}^\pm_{L,R}$ and $\tilde{\tau}_{1,2}$ can be produced in pairs at the ILC. The production of smuons and staus is mediated by s-channel γ/Z exchanges. The production of selectrons proceeds through t-channel exchanges of neutralinos or charginos. In the SPS1a scenario, the decays of all sleptons directly into the LSP, $\tilde{l} \rightarrow l\tilde{\chi}^0_1$, are the dominant ones. The slepton masses can be measured in threshold scans or obtained from the endpoint energies of the leptons from slepton decays[2]. The confirmation of the $\sin^2\theta$ law for the angular distribution of the sleptons will reveal their scalar nature. In the stau sector, large mixing is expected as the mixing of sfermions is proportional to m_f. The mixing angle can be extracted from two measurements of the cross section $\sigma(e^+e^- \rightarrow \tilde{\tau}_1\tilde{\tau}_1)$ with different beam polarizations.

In some scenarios, the lightest top or bottom squarks may be detected at the ILC. The masses and mixing angles of $\tilde{t}$ and $\tilde{b}$ may be extracted from production cross sections measured with polarized beams. The measurement of top quark polarization in squark decays can provide information on $\tan\beta$.

2.3 Other scenarios

High luminosity of the ILC experiment provides the possibility to investigate the SM more carefully. The interactions amongst gauge bosons can be measured more precisely than in previous experiments. Thus, the ILC allows to constrain new physics at scales far above the direct reach of the collider, through quantum corrections. Precision measurements of the effective weak mixing angle and the W boson mass are another important task. With the GigaZ mode (high luminosity running on the Z peak), the ILC can produce 10^9 Z decays in one year or run at the W pair production threshold to measure the W boson mass

[2]See detailed discussion in chapter 8.

precisely [35]. Virtual effects of new physics beyond the SM can be probed. QCD can be tested at high energy scales in the e^+e^- environment at the ILC. The strong coupling α_s will be measured accurately. Precision measurements of the masses and interactions of the top quark in a model-independent way at the ILC may reveal new physics beyond the SM. New decay modes of the top quark predicted by some theories may be discovered.

Besides SUSY, there are many theoretical models beyond the SM, such as models with extra dimensions, models without Higgs, and little Higgs model. These models introduce new particles and interactions at the Terascale which are possibly observed at the LHC. However, it is likely not possible to pin down the underlying theory at the LHC. If new signals are indeed observed, the nature of the new physics can be determined by the precision measurements or indirect searches at the ILC.

The ILC will play an important role in the search for dark matter. New physics beyond the SM may result in new stable but invisible particles, which are considered to be the candidates of dark matter. These particles may be produced at the ILC. An excellent candidate is the LSP in many SUSY scenarios. The precision measurements at the ILC are very likely able to reveal the nature of dark matter.

Chapter 3

Detectors for the International Linear Collider

Owing to the well defined center-of-mass energy, initial helicity states and low backgrounds of e^+e^- collisions, the experimental conditions of ILC provide an ideal environment for precise measurements of particle productions and decays as well as the discovery of new physical phenomena. As the ILC detectors will record data without any trigger, the bias resulting from such trigger selections will not emerge. The ambitious physics program at the ILC presents unprecedented challenges for the detector performance. The jet energy resolution, track momentum and impact parameter resolution are required to be much better than those achieved at previous e^+e^- collision experiments. For example, the precise reconstruction of the invariant masses of W, Z, H bosons and other heavy particles from multi-jet final states requires the di-jet mass resolution to be comparable to the natural width of the parent particles, which can be achieved with a jet energy resolution $\Delta E/E$ to $3 \sim 4\%$ ($30\%/\sqrt{E}$ for jet energies of 100 GeV) [36]. Studies on multi-jet final states and possible SUSY processes requires nearly full solid angle coverage for the tracking system. The momentum resolution $\Delta p_t/p_t^2$ is required to reach 5×10^{-5} $(\mathrm{GeV}/c)^{-1}$ for the precise determination of the Higgs mass from the dilepton recoil mass spectrum [37,38,39] and measurements of slepton masses [38,39]. To achieve these goals, novel detector technologies and event reconstruction methods are required.

In the past decade, the International Linear Collider physics and detector communities have invested much effort in the research and development of detectors for the Linear Collider and made impressive progress in many detector technologies. In 2001, several documents summarized the early detector concepts with design studies performed in Europe [3], Asia [40] and North America [41]. In the last few years, several ILC detector concepts have been proposed and studied. The SiD [7] and ILD [8] concepts use traditional solenoidal magnetic field and adopt the particle flow concept, which requires high granularity calorimeters to separate close-by showers, while the 4th concept [9] puts more emphasis on compensating calorimetry with a dual readout system.

In this chapter, brief introductions to the particle flow algorithm and the detector concepts

are given.

3.1 The Particle Flow Algorithm

The most promising strategy for event reconstruction at the ILC is widely believed to be the particle flow algorithm (PFA). In contrast to the pure calorimetric approach, PFA implies the reconstruction of the four momenta of all visible particles in each event.

In PFA, the reconstructed jet energy is given by the sum of all the individual particles within it, and thus the jet resolution is given by

$$\sigma^2_{jet} = \sigma^2_{charged} + \sigma^2_{\gamma} + \sigma^2_{h^0} + \sigma^2_{confusion}, \tag{3.1}$$

where $\sigma_{charged}, \sigma_{\gamma}$ and σ_{h^0} are the energy resolutions of charged particles, photons and neutral hadrons, respectively. The term $\sigma_{confusion}$ reflects confusion in the reconstruction of calorimetric clusters due to the misassignment of hits. Measurements at LEP show that around 62% of jet energy is carried by charged particles, around 27% by photons, around 10% by neutral hadrons, and 1% by neutrinos [42, 43]. A good tracking system guarantees that $\sigma_{charged}$ is much smaller than the other terms. In perfect PFA, the jet energy resolution is dominated by the energy resolution of photons and neutral hadrons. For the perfect PFA, a jet energy resolution of $0.19/\sqrt{E(GeV)}$ is obtained if one assumes an energy resolution of $0.15/\sqrt{E(GeV)}$ for photons and $0.55/\sqrt{E(GeV)}$ for hadrons [44, 45] as expected for ILC detectors. But the term $\sigma_{confusion}$ degrades the overall particle flow performance in real detectors. Clearly, efficient separation of close-by showers is vital for PFA. Hence both the electromagnetic and hadronic calorimeters should be characterized by fine granularity in both the transverse and longitudinal direction. Following the PFA approach, the momenta of charged particles are measured using the tracking system, while the energies of neutral particles are measured using the calorimeter. Thus detector concepts driven by PFA combine precise tracking with imaging calorimeters.

3.2 Detector Concepts

Four detector concepts emerged in the last few years. Three of them, the SiD [7], LDC [46] and GLD [47] concepts are based on the PFA concept, aimed at reconstruction of all visible particles in each event. The 4th concept puts emphasis upon excellent energy resolution in the calorimeter. Recently LDC and GLD concepts united to form the ILD concept [8].

All these different concepts have several common features. Pixel technology based vertex detectors are adopted by all the concepts to provide excellent vertex reconstruction and serve as a part of the tracking system. Each concept has its own sophisticated main tracking system for precise tracking in the high multiplicity environment. Calorimeters are placed inside the coil to ensure good energy resolution. High magnetic fields ranging from 3 to 5 T are used to ensure excellent momentum measurements of tracks.

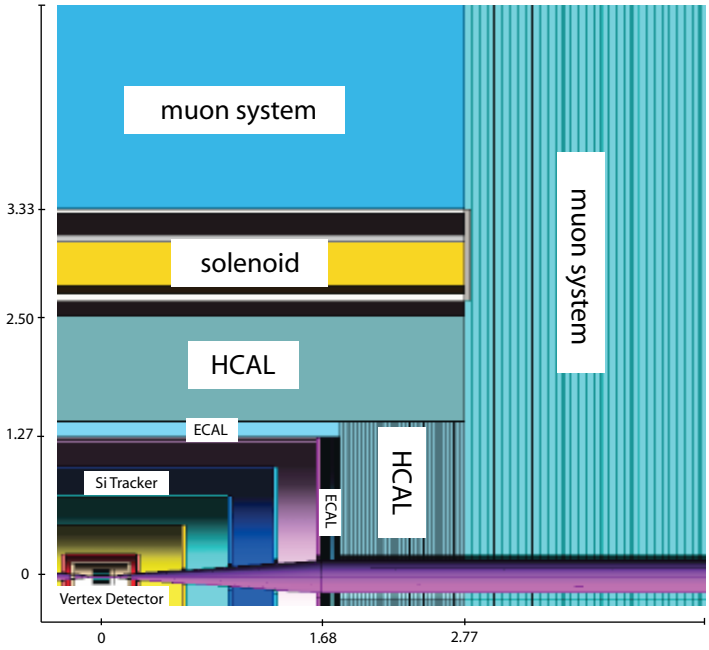

Figure 3.1: The schematic view of a quadrant of SiD. The scale shown is in meters.

3.2.1 The SiD Concept

The SiD (Silicon Detector) concept is based on silicon tracking and a silicon-tungsten sampling calorimeter, complemented by a powerful pixel vertex detector, an outer hadronic calorimeter and a muon system. The general purpose detector is designed to meet the requirements of the ILC physics goals by taking full advantage of silicon technology. The detector is also capable of identifying the individual bunch crossings, separated by 150 ns. The detector geometry is compact as the finely grained silicon-tungsten electromagnetic calorimeter is expensive. High tracking precision is achieved by the large magnetic field of 5 T and silicon tracking devices with excellent spatial point resolution.

A schematic view of SiD is presented in Fig. 3.1. The detector has the following components from the inside to the outside:

- The pixel vertex detector consists of a central barrel with five silicon pixel layers and four endcap layers on each side to cover small angles, which provide good hermeticity for $|\cos\theta| < 0.99$. The radius of the innermost layer of the barrel is 14 mm.

- The main tracker consists of five silicon strip layers in the barrel region and five disks in each of the endcap regions. Both the layers and the disks are supported with low mass carbon fiber/rohacell structures. In the barrel, only axial information of hits is measured. The strip pitch of the barrel sensor is 50 μm. The end disks will provide 3-D space hits for pattern recognition. The strip pitch will vary with radius. The spatial point resolution is of $\mathcal{O}(10)$ μm.

- The electromagnetic calorimeter (ECal) consists of 30 layers of tungsten radiator and large-area silicon diode detectors for both barrel and endcaps. The silicon detectors are segmented into pixels of area 12 mm^2 to provide pattern recognition of showers and particle separation. The calorimeter also provides information for the tracking of long-lived charged particles by a new calorimeter-assisted tracking method.
- The hadronic calorimeter (HCal) is located outside of the ECal and has barrel and endcap parts. The HCal has a sandwich structure using steel as absorber and resistive plate chambers (RPC) as sensitive medium. Scintillators, Gas Electron Multipliers (GEMs) and Micromegas are considered as alternative detector technologies. The two endcaps are inserted into the barrel structure. The thickness of each steel plate is 20 mm. There are in total 34 layers, leading to a depth of four nuclear interaction lengths.
- The tracking system and calorimeters are placed inside a magnetic field of 5 T provided by a superconducting solenoid. The operational CMS solenoid [48] provides a proof-of-concept for the SiD solenoid.
- The flux return consists of iron plates with a thickness of 10 cm. Muon systems are installed inside the gaps of the flux return. RPCs and scintillator strips are considered as the technology for muon detection.
- The forward systems consist of a BeamCal, a luminosity calorimeter and a GamCal. They are placed in the forward region of the endcap ECal with $|\cos\theta| > 0.99$ to measure the luminosity normalization or the instantaneous luminosity by catching very forward pairs or measuring beamstrahlung photons downstream the main detector. They are not illustrated in the figure.

The ongoing activities of the SiD concept include the optimization of the overall detector design, the detailed design of the subsystems, developing of design tools for performance studies and the physics analysis based on full Monte Carlo analysis.

3.2.2 The ILD Concept

The ILD (International Large Detector) concept has emerged as a result of unification of the LDC (Large Detector Concept) and the GLD (Gaseous Large Detector) detector concepts. The ILD detector & physics group was founded with the intention to cooperate in the preparation of the Letters of Intent (LoI).

The reason for the merging of LDC and GLD is simple. Both concepts use the PFA as the basic reconstruction paradigm, and they have similar structure. Large Time Projection Chambers (TPCs) serve as the main tracker in both concepts. The main difference comes from the overall size and the magnetic field. GLD adopts a magnetic field of 3 T with larger geometry size, while a magnetic field of 4 T is foreseen for LDC.

Fig. 3.2 and Fig. 3.3 give the schematic view of the quadrants of LDC and GLD, respectively. The structure of ILD inherits from those of LDC and GLD, but with some modifications.

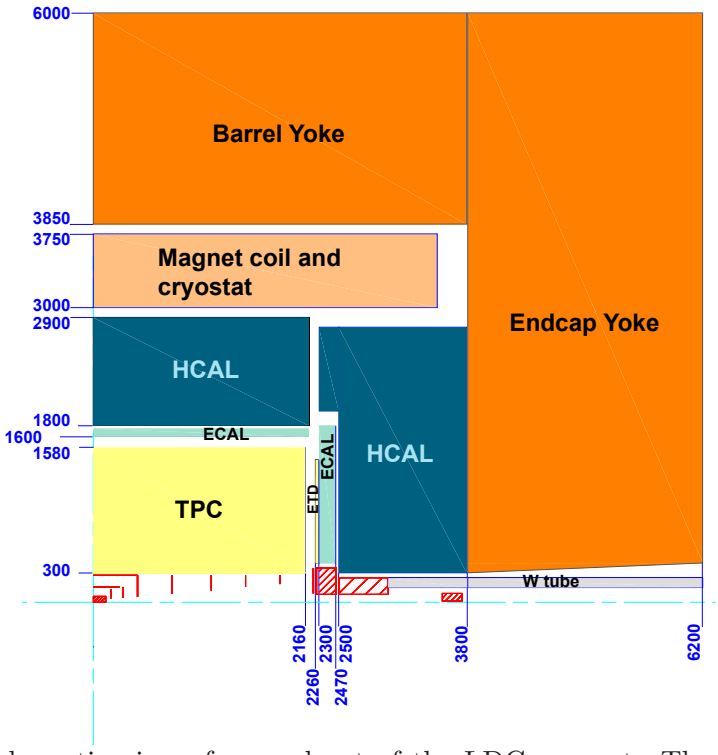

Figure 3.2: The schematic view of a quadrant of the LDC concept. The scale shown is in millimeters.

The overall dimensions of the detector are the subject of current optimization studies, using as criteria PFA performance and cost. The final ILD detector has the following components:

- A pixel vertex detector around the interaction point. In GLD, a vertex detector consists of three layers of doublets and one endcap disk on each side, where each doublet is made of two sensor layers. The basic layout of the vertex detector in LDC has a barrel structure of five sensor layers. The two proposals are kept in ILD and are under development.

- The inner silicon detectors, which include the intermediate silicon detector and the forward tracker. The former provides additional hits to bridge the gap between TPC and vertex detector, the latter makes tracking in the forward/backward region of the detector possible. Silicon strips and pixels are consider as the technology for the inner silicon detector. Its designs vary considerably between LDC and GLD. A set of studies are being performed to decide on the final layout.

- The TPC. Both LDC and GLD rely on a large volume TPC for tracking and the differences are small. The TPC is capable of providing up to 200 space points per track, enabling excellent 3D point resolution, and in addition, particle identification via the measurement of specific energy loss (dE/dx).

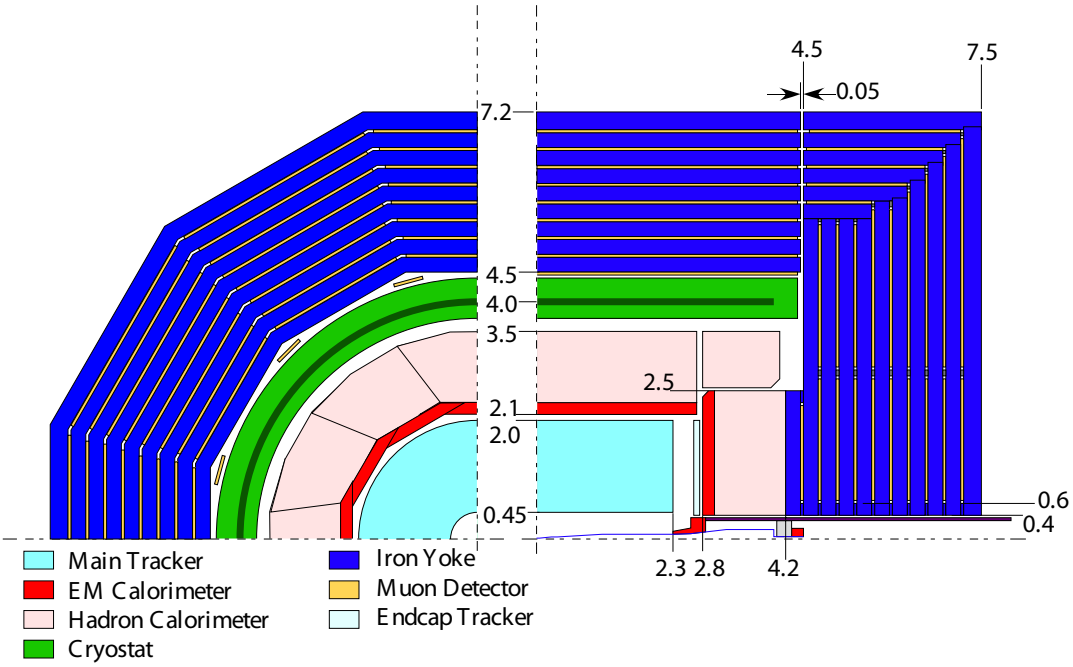

Figure 3.3: Schematic view of a quadrant of the GLD concept. The left figure shows the $r\phi$-view and the right shows the rz-view. The scale shown is in meters. The vertex detector is omitted.

- The calorimeters. The basic layouts in the two concepts are the same. ECal and HCal are inside the coil. Barrel and endcaps are separated. For the ECal, LDC adopts the W-Silicon technology, while GLD uses Pb-scintillator sampling devices. The LDC HCal is based on Fe-scintillator, and GLD HCal uses Pb-scintillator. The final choice of technologies for ILD calorimeters will depend on the performance evaluation and cost.
- Large volume superconducting coil. The optimal value of the magnetic field is to be determined. A detector model with a B-field of 3.5 T is under study.
- Muon detectors. They are instrumented inside the iron return yoke. Possible technologies are scintillator strips or large area RPCs.
- The forward detectors. Layouts of forward detectors in LDC and GLD differ in detail, but are similar in principle. Their purpose is to measure the luminosity spectrum and monitor beam condition.

The optimization studies of ILD have started from the basic layout of LDC and GLD, adjusting their parameters. The goal is to design a high-performance detector at reasonable

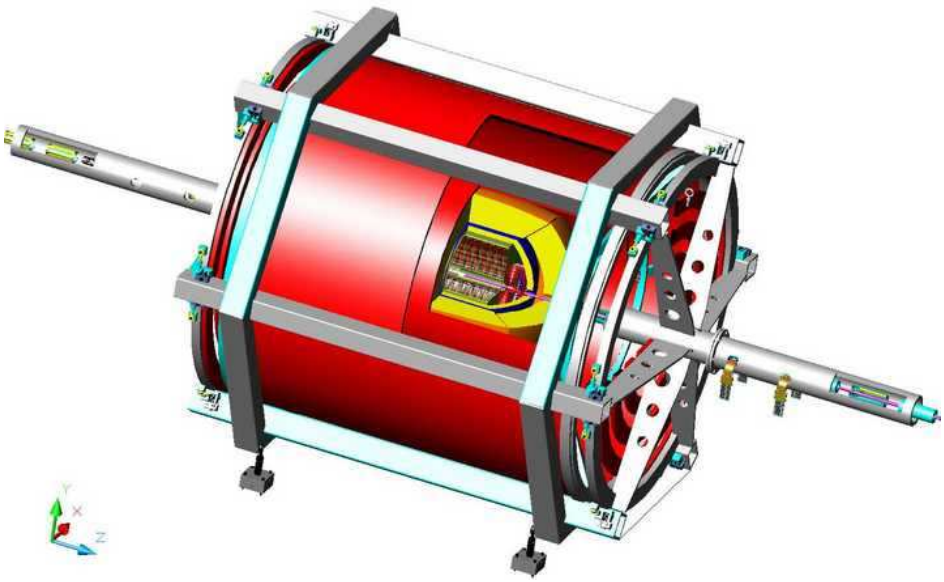

Figure 3.4: Cut-away view of the 4th concept detector. Components from the inside to outside are vertex detector, TPC (green), calorimeter (yellow) and solenoids (red).

cost.

3.2.3 The 4th Concept

The Fourth Concept is different from other two concepts in several respects. It utilizes a novel implementation of compensating calorimetry, which is insensitive to fluctuations in the fraction of electromagnetic energy in showers so that high precision measurement of hadrons and hadron jets can be performed. It also adopts a unique structure of dual-solenoid system. The outer solenoid is used to return the magnetic flux by the inner one. A low mass detector is hence achieved as no iron returning yoke is necessary.

The principle of dual-readout calorimetry is to use two types of fibers, scintillator and quartz, to measure the energy deposited in the calorimeter. The fraction of electromagnetic energy can be obtained by comparing the two signals. Thereby, "software compensation" and excellent hadron energy resolution can be obtained. Compared to the particle flow calorimetry, which requires highly granular calorimeters in both longitudinal and transverse direction, the dual-readout calorimeter has only transverse segmentation.

Fig. 3.4 gives a cut-away view of the 4th concept detector. The detector has the following components:

- A vertex detector, which has the same design as the SiD detector with small changes in dimensions.
- A TPC, which is similar to that used in ILD. The concept includes the option of a low

mass, cluster-counting KLOE-style drift chamber for readout. The TPC is used as the main tracker.

- The dual-readout calorimeters. The detector is based on copper absorber structure.
- The large radius solenoids. The tracking system and calorimeters are placed inside the 3.5 T axial field provided by the solenoids. The B-field of the outer solenoid is opposite to that of the inner solenoid.
- The muon system, which consists of high resolution drift tubes placed in the region between the two solenoid.
- The endcap "wall of coils" which confines the flux of the two solenoids.

The full detector simulation, calibration and physics analysis of the 4th concept are based on the framework of ILCroot, which is being continuously upgraded.

Chapter 4

The DEPFET Vertex Detector

A high precision pixel vertex detector is necessary in all of the detector concepts proposed for the ILC. It is required to provide accurate impact parameter determination, precise vertex resolution and efficient jet flavor tagging including charge determination in a wide range of $\cos\theta$. It is also expected to provide additional tracker hits to improve the overall tracking efficiency. As the vertex detector is very close to the interaction point (IP), it should be robust against the strong machine-induced background, synchrotron radiation, back scattered photons and neutrons.

The physics requirements push the technology of the vertex detector sensors to a new level. Several different pixel sensor architectures are proposed and demonstrated to be compliant to the requirements of the ILC experiment. The DEPFET (abbreviation for **DEP**leted **F**ield **E**ffect **T**ransistor) technology, is one of them [10, 49].

The concept of DEPFETs was proposed in 1987 [50]. After development in the nineties [51, 52], it is now fabricated in new MOS technology and will be used, for instance, in experiments for X-Ray astronomy, in addition to particle physics. The basic principle of DEPFET is the integration of an amplifying field effect transistor (FET) into a fully depleted bulk in such a way that signal charges are collected in the "internal gates" of the transistors. The full depletion of the substrate results in fast charge collection. The amplification of the integrated FET guarantees low noise even at large bandwidth. The pixels in a matrix can be readout by rows in a rolling shutter mode, achieving high frame readout rate (50μs/frame). Due to the internal storage of signal charges, a row is active only when it is readout. Hence, power consumption is minimized. These features make DEPFET an ideal candidate for the ILC vertex detector.

This chapter is a brief introduction to the DEPFET technology and its application in the ILC experiment. More detailed information can be found in the report by the DEPFET collaboration [49].

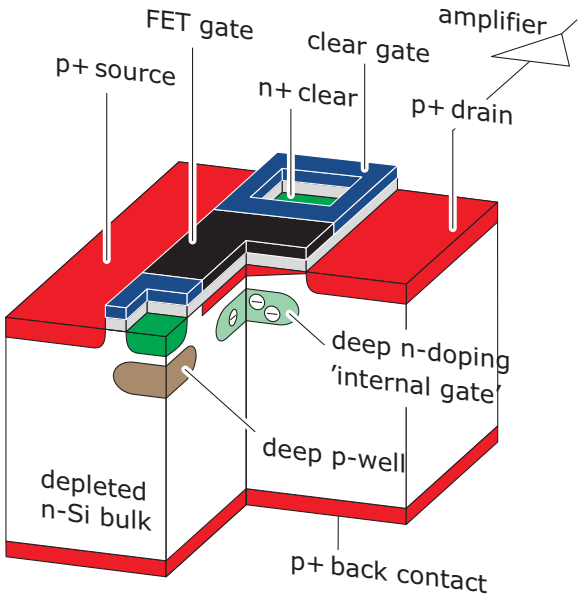

Figure 4.1: The operation principle of a DEPFET pixel.

4.1 Principle of DEPFET

The DEPFET sensor combines the properties of detection and amplification in one device. The principle of operation is shown in Fig. 4.1. A p-type MOS or junction FET is integrated onto a silicon detector substrate, which becomes fully depleted by applying a sufficiently high negative voltage to the p-doped contact in the backside. By sideward depletion, a potential minimum for electrons is formed below the transistor channel at the depth of 1 μm. When incident radiation passes the sensor, electron-hole pairs are generated by ionization inside the bulk. They are separated by the electric field. Holes drift to the p-doped contact, while electrons accumulate in the potential minimum called internal gate and thus increase the charge density by induction. The effect leads to a modulation of the transistor current. The readout does not change the charge density, thus it can be repeated several times. The so called clear process is used to remove signal charges and thermal electrons in the internal gate. It is realized by applying a positive pulse to the n-doped contact, which provides a punch-through into the internal gate. A p-doped layer is implanted beneath the clear contact to prevent signal charge from reaching the clear contact during the charge collection phase. The amplification of the signal charge occurs at the position where the signal is generated. Consequently, the signal loss resulting from charge transfer can be avoided. As the bulk is full depleted, it is sensitive to incident radiation. The whole non-structured backside can be used as an entrance window. All these factors improve the spectroscopic performance especially for low energy photons. The small input capacitance allows low noise operation even at room temperature [49].

The DEPFET sensors can be operated individually or as a pixel array. The latter property

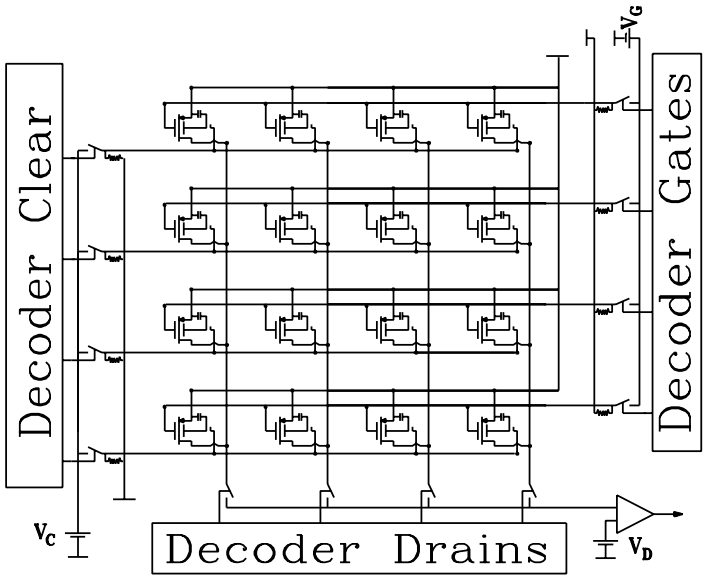

Figure 4.2: An schematic example of the DEPFET pixel matrix operated by rows.

makes DEPFET applicable as vertex detector at the ILC. Fig. 4.2 gives an example of the DEPFET array operated by rows via the external gates. The external gates are only used to switch the pixels on and off. There is no current flow in the non-selected DEPFET row. So the power consumption of the matrix is very low. For application at the ILC, the readout amplifiers at the end of each column are connected to drains of the DEPFETs. A typical measurement process includes the collection of charges (Collect), the readout of signals (Read) and the clear of internal gate (Clear). Pedestal subtraction can be obtained by the Read-Clear-Read sequence. It is obvious that the clear process should completely remove the charges in the internal gate to avoid reset noise. The signals of pixels in a column are readout sequentially by a chip. Contrary to the CCD, the signal charge is not moved, hence wrong assignment of position information for the signal is completely avoided.

The properties of DEPFETs have been demonstrated with DEPFET prototype matrices produced in 2004. MOS devices are used for the large matrices to reach the performance requirements. Complete clearing and operation with constant clear-gate potential have been achieved with small DEPFET matrices, using a precisely positioned laser spot [53]. An intrinsic noise value of 1.6 electrons has been measured with linear, ILC like DEPFETs, albeit at long integration times (10 μs). Higher noise is expected at a bandwidth of 50 MHz as needed at ILC. By calculation and extrapolation of measurements, the intrinsic noise of DEPFET is well below 100 electrons at 50 MHz [49]. A signal to noise ratio of 40:1 can be achieved.

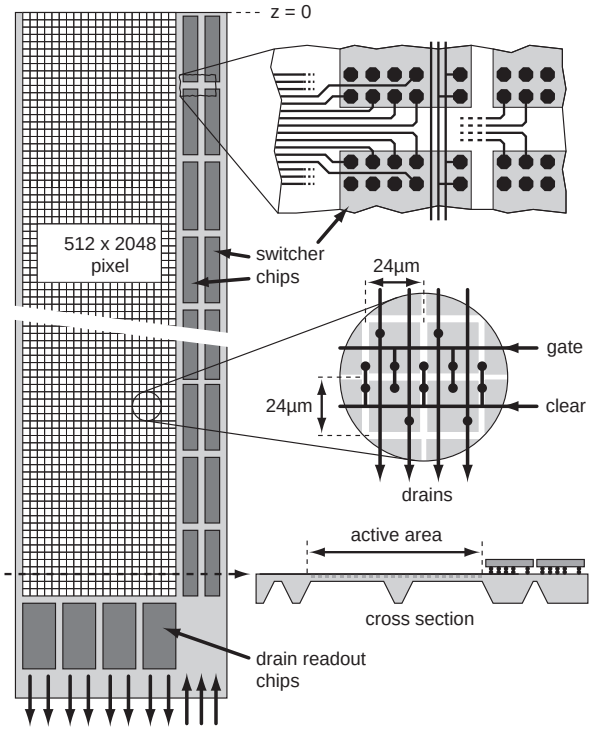

Figure 4.3: Sketch of a ladder in the innermost layer of the DEPFET based vertex detector. There are 4096 (2048×2) pixels in the z direction. The part with $z < 0$ is not shown.

4.2 The DEPFET ladder

The DEPFET based vertex detector for the ILC is developed following the layout proposed in the TESLA TDR [3]. The layout is also valid for the succeeding LDC [46] and ILD concepts [8]. In the TESLA TDR, the vertex detector has a 5-layer barrel structure composed of thin ladders. The distance from the interaction point to the surface of the innermost layer is around 15.5 mm.

Fig. 4.3 shows the sketch of a ladder in the innermost layer. The sensitive area is a DEPFET matrix with 512×4096 pixels, and its dimension is 13×100 mm^2. The dimension of a signal pixel is around 25×25 μm^2. The thinned steering chips for switch and clear are attached at the long side of the ladder. The drain readout chips, lines for power supply, slow control and data transmission are placed on both short sides of the ladder outside the fiducial volume of the vertex detector.

An all-silicon self-support concept has been developed for DEPFETs. The matrices are supported by a directly bonded silicon frame of $\approx$ 500 μm thickness. The sensitive area, however, is thinned to 50 μm. A new approach of thinning technology is employed to produce the ultra thin sensors. The process sequence is illustrated in Fig. 4.4. It starts with two oxidized silicon wafers. The DEPFET matrix is located in the top wafer. The second wafer is the handle wafer which will become the support frame. The backside implantation for

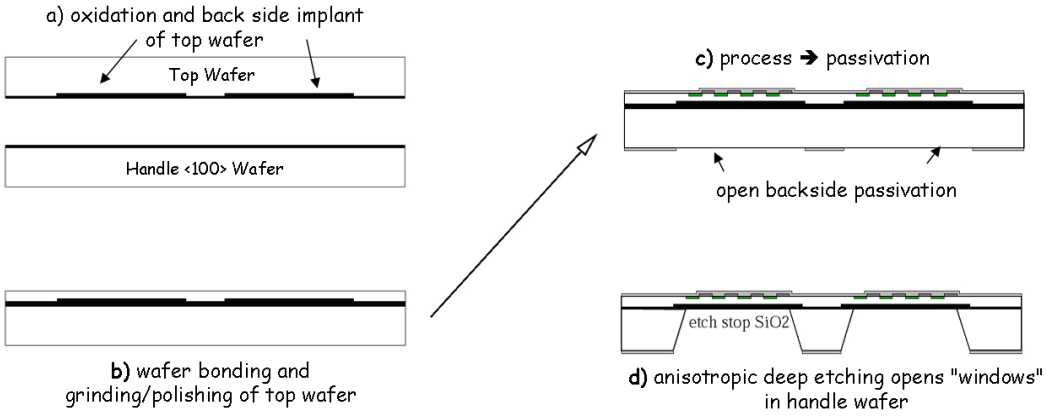

Figure 4.4: The process sequence for the production of a thin functional DEPFET sensor with support frames.

the DEPFET is done at the stage of processing. At the second stage, the two wafers are bonded together to a stack. Strong Si-O-Si bonds form between the two wafers "gluing" them together. The top wafer is then thinned to the required thickness. The stability of the stack enables top side processing for micro electronics with the usual equipment for semiconductor manufacturing. Patterned passivation layer is covered in the backside of the handle wafer. It serves as the etch mask for the deep etching of the handle wafer from the backside, so that the silicon of the handle wafer can be selectively etched away [49].

Mechanical prototypes of a DEPFET ladder of the innermost layer have been produced, as shown in Fig. 4.5. The thick support frame gives the biggest contribution to the material budget. It is believed that the frame can be made as narrow as 1 mm and a cavity pattern can be etched into the support frame so that the material in the support frame can be reduced by 33%. The self-supported structure needs no additional support material. Due to the asymmetry of the Si-SiO_2-Si bond from different thicknesses, a built-in stress in the stack was caused by the high temperature processing. The stress leads to a bow on the wafer level. The bow was measured to be 140 μm over 10 cm. The bow is expected to be constant after the processing, for the temperature differences are small. The effect of gravity has also been measured. The gravitational sag is about 20 μm over 10 cm, and is considered to be tolerable [49].

One advantage of DEPFET is that the sensor only consumes energy during the readout sequence. For an active pixel, the power consumption is 500 μW. In one ladder of the inner layer, two double rows ($2 \times 2 \times 512$ pixels) are active at the same time, resulting in 1 W per ladder. By adding up the contributions from all the active pixels, the steering and readout chips, the total power consumption of the DEPFET vertex detector is 1272 W. However, most of the active electronics can be switched off between the bunches, hence the average power consumption of the vertex detector can be reduced by a factor of 1/200 to about 6.4 W. The low energy consumption makes the cooling system less critical.

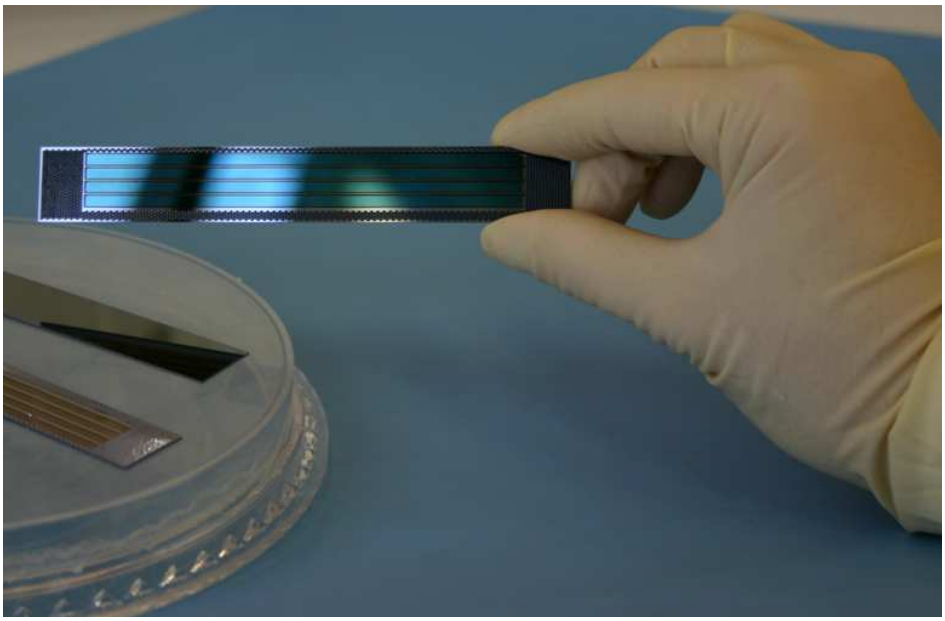

Figure 4.5: A sample DEPFET ladder in the innermost layer.

4.3 The steering and readout chips

The steering and readout chips are two ASICs to operate the DEPFET matrix. The steering chips are used to provide external gate signal and clear the charges collected in the internal gate. The readout chips are used for the readout of drain currents.

The steering chips, called "*SWITCHER*", are attached on the long side of the ladder as seen in Fig. 4.3. For the application in the ILC environment, the *SWITCHER* chips have to be sufficiently radiation tolerant. They also need to be as small and thin as possible to minimize the dead material. The rise/fall time of the signals produced by the chip has to be less than 10 ns for a load of 20 pF to enable quick readout and clear process. The number of power supplies and control signals should be minimized to simplify module construction.

Three generations of *SWITCHER* chips have been developed so far. The first generation is for simple test. The second has been used for lab and beam test in the past several years. The third generation is designed for operation at the ILC. It has all the features required by the ILC.

Two type of chips are designed to readout the DEPFETs by measuring the current change in the drain resulting from the charge collected in the internal gate. The current is generated by one DEPFET row which is activated by the *SWITCHER*. The value of current depends on properties of the DEPFET and on the potential of the external gate. A negative charge value Q in the internal gate causes a current increase by $Q \times g_{\mathrm{q}}$, where g_{q} depends on the DEPFET type and is in the order of $0.3 \sim 0.5$ nA/electron for present DEPFETs. The current change is given by subtracting the current value after the clear stage. In the DEPFET matrix, the

double pixel structure in two rows shares the same gate and clear signal. So the readout chips should be able to perform double row readout at the same time. The readout chips are outside the active region so that the material budget is not crucial. The *CURO* (CUrrent ReadOut) chip has been used in the past several years. It stores the signal difference in an array of analog memory cells for zero suppressed readout. For the present DEPFET devices, the *CURO* gives an equivalent noise charge of 250 electrons for fast readout. The developing *DCD* (Drain Current Digitizer) chip is the successor of the *CURO* chip and designed for the application at the ILC. It will digitize the current signal immediately to deal with the high occupancy resulting from the ILC background. The first test chip of *DCD* with a size of 1.5×3 mm^2 has been successfully tested.

4.4 Radiation tolerance

Since the inner layer of the vertex detector is very close to the interaction point, it should be capable of withstanding the high backgrounds induced from pair-production, beamstrahlung, synchrotron radiation and other processes. The electron-positron pairs generated in the interaction of primary beam bunches are the dominant part of the background affecting the vertex detector. It has been estimated that the sensors need to withstand a total ionizing dose of a few hundred krad in their 5-years lifetime, and the dose of neutron background induced from pair production is below a flux of 10^{10}/cm^2/year [3, 46, 36].

Background particles lead to radiation damage through ionizing energy loss as well as bulk damage through non-ionizing energy loss. Bulk damage from neutrons or charged hadrons leads to an increase of the bulk leakage current. Trap generation by non-ionizing energy loss has minor effects to the DEPFET matrices. The radiation damage has more effects on the MOS-base device. The radiation induced charges built up in the oxide and interfacial regions lead to a shift of clear threshold voltage to more negative values. The lower mobility of charge carriers after irradiation reduces the transconductance, i.e. the ratio of output current and input voltage. The noise of the transistors may increase due to the build up of states at the interface between Si and SiO_2.

Single pixel DEPFETs have been tested with X-ray, ^{60}Co gammas, protons, and neutrons. After irradiation of up to 1.2 Mrad(Si) of photons, the maximum threshold voltage shift of the DEPFETs is around -8 V. The small shift of threshold voltage is also observed after irradiation of protons with a fluence of 1.2×10^{12} p/cm^2 . The DEPFET also shows a moderate noise increase of about 6 electrons equivalent noise charge even after the total ionizing dose of 1 Mrad(Si), as shown in Fig. 4.6. The noise resulting from the increasing leakage current due to the bulk damage can be minimized by moderate cooling of the device. The measured equivalent noise charge is about 14 electrons at -10°C after the irradiation of protons with an equivalent 1-MeV-neutron fluence of 3×10^{12} n/cm^2, which is far beyond the one expected at the ILC [49]. After the neutron irradiation with an fluence of 2.4×10^{11} n/cm^2, the measured equivalent noise charge is about 3 electrons at 6°C. The results are plotted in Fig. 4.7. It is clear that the DEPFET sensor has very good radiation tolerance. But these tests have been made with single pixel structure only. More tests on the DEPFET matrices need to be done

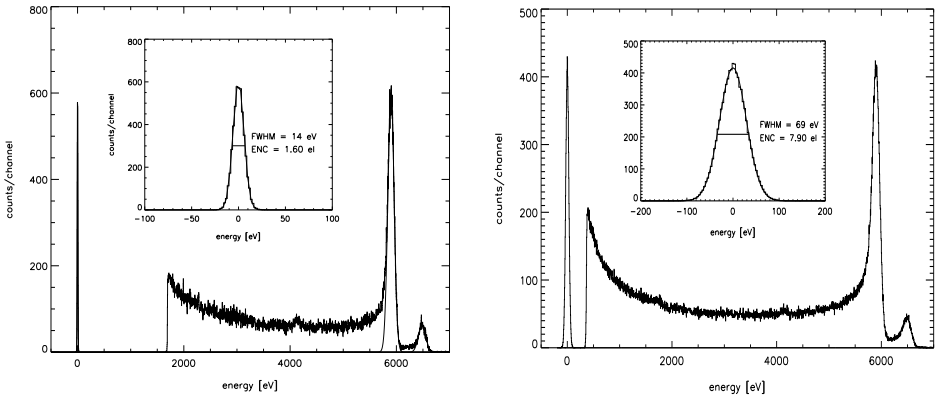

Figure 4.6: ^{55}Fe spectrum obtained using a linear DEPFET single pixel at room temperature with 10 μs shaping time before (left) and after (right) irradiation with total ionizing dose of 912 krad(Si). The noise increase is about 6 electrons equivalent noise charge after the irradiation.

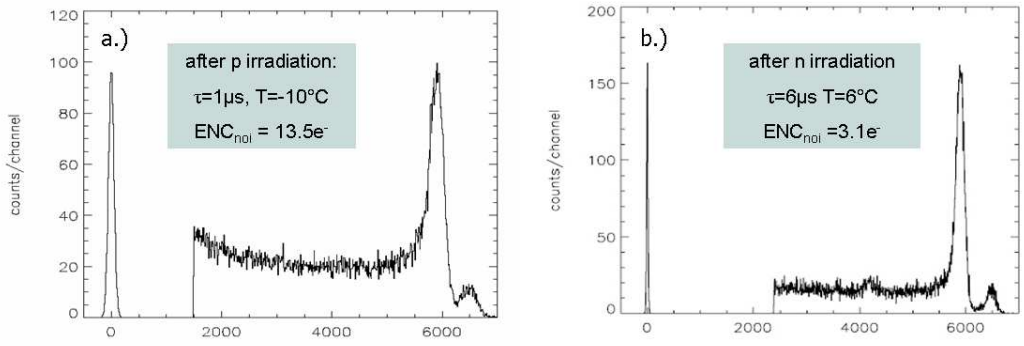

Figure 4.7: ^{55}Fe spectrum obtained using a linear DEPFET single pixel after proton (left) and neutron (right) irradiation at -10°C and 6°C, respectively.

and are currently in progress.

Chapter 5

Software tools

The optimization and development of the ILC detectors requires a large variety of software tools ranging from data model, detector simulation, digitization, reconstruction and analysis. As several different detector concepts of ILC are studied in Asia, Europe and North America, several different software frameworks are employed.

The software framework and workflow widely used in the studies of the LDC concept are illustrated in Fig. 5.1. The LCIO (**L**inear **C**ollider **I/O**) [54] is a persistency framework. It provides a data model and has been adopted as an international standard by the ILC community. The Mokka [55, 56] program is a detailed full simulation program for the ILC detectors based on Geant4 [57, 58]. It was originally developed for the TESLA project, but now it contains models for TESLA, LDC, SiD and testbeam studies. It is also selected as one of the standards for the full simulation in the R&D of ILD. The output of Mokka is always the LCIO event file. Marlin (**M**odular **A**nalysis and **R**econstruction for the **LIN**ear collider) [59] provides an application framework for the reconstruction and analysis of LCIO data. GEAR (**GE**ometry **A**PI for **R**econstruction) [60] is a geometry description toolkit for the reconstruction software of ILC. By using GEAR, the Mokka program can print out the parameters of a detector into an XML file, which can be used by the reconstruction and analysis modules of Marlin.

All these software tools are used in the development and optimization of the DEPFET based pixel vertex detector and the LDC concept. In this chapter, these software tools are described in detail and their applications are discussed.

5.1 LCIO

LCIO is designed to make data persistent in between the different stages of simulation, reconstruction and analysis. It has been adopted as the standard by the international ILC community. An abstract event data model of hits, tracks, cluster, etc. is defined by LCIO. It also provides a concrete file format to store the data. C++ and Java implementations are provided together with APIs to manipulate the data. A Fortran interface to the C++

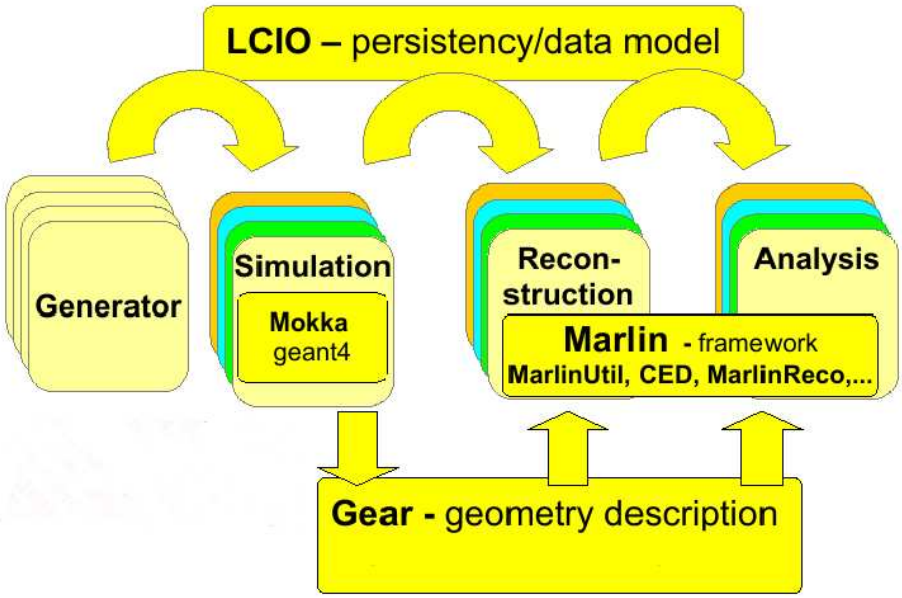

Figure 5.1: Overview of the software framework used in the R&D of LDC.

implementation is provided as well. These APIs are implemented in a way that the user code is independent of the concrete file format. So LCIO files can be exchanged between different software frameworks without rewriting any user codes if the standard is followed. LCIO is designed in a way which ensures the interoperability between different software frameworks. The interoperability is an important feature for the detector concept studies for it provides a platform for the comparison and cross-check between different concepts, codes and algorithms.

The major entities defined by the LCIO data model include *LCEvent*, *MCParticle*, *SimTrackerHit*, *TrackerHit*, *SimCalorimeterHit*, *CalorimeterHit*, *Cluster*, *Track*, *ReconstructedParticle* and *LCRunHeader*. Each entity is a special *LCObject* except for the *LCEvent*. The *LCEvent* entity serves as a container for all the data related to an event. It contains an arbitrary number of other entities through the collection of *LCObject*, which is called *LCCollection*, except for the *LCRunHeader*, which is included only once. The *MCParticle* is the list of particles created by the event generator and possibly by the simulation program. The simulation program will also add objects of *SimTrackerHit* and *SimCalorimeterHit* to their collections. Digitization programs will create objects of *TrackerHit* and *CalorimeterHit* based on the simulation information. The reconstruction programs create objects of *Track* and *Cluster* by using tracking and clustering algorithms, and use the "Particle Flow Algorithm(PFA)" to create reconstructed particles, which are stored as the objects of *ReconstructedParticle*. The internal relations between different entities are also defined by LCIO. For example, we can find the corresponding hits for arbitrary track and vice versa if possible, or find the corresponding tracks and clusters of a reconstructed particle.

5.1.1 Track parameters in LCIO

The track parameters defined in LCIO are introduced in [61]. The track of a charged particle moving in the constant magnetic field of an ILC detector is described by a helix whose axis is parallel to the beam line. The five parameters which fully determine the spatial properties of a track are Ω, ϕ_0, d_0, z_0 and $\tan\lambda$:

- Ω is the signed curvature of the track. It is positive if the particle has positive charge and negative if the particle has negative charge.
- ϕ_0 is the azimuthal angle of the momentum at the position of closest approach to the reference point.
- d_0 is the signed distance of the closest approach to the reference point.
- z_0 is the z position of the point of the closest approach to the reference point.
- $\tan\lambda$ is the tangent of the angle between the r-ϕ plane and the momentum of the particle.

The reference point is chosen to be the original point (0,0) in r-ϕ plane by most of the tracking algorithms provided by MarlinReco [62]. LCIO also provided a way to access the covariance matrix

$$\mathbf{Cov} = \mathrm{Cov}(i,j) \quad \text{with} \quad i,j \in \{d_0, \phi_0, \Omega, z_0, \tan\lambda\}, \tag{5.1}$$

where the order of the parameters in rows and columns follows that given in this formula.

5.2 GEAR

The tracking and PFA algorithms in the reconstruction programs need to know the distribution of material inside the detector. As there are many detector models with different parameters, it would be convenient for the reconstruction program to read the description of detector geometry provided by the simulation program. The GEAR toolkit serves as a bridge between the simulation and reconstruction program by providing the description of the detector geometry based on the XML file format.

The output GEAR XML is easy for humans to read. The parameters are organized in a tree structure of "gear–detectors–detector–parameters". Each sub detector is described by the parameters in one or more "detector" terms in the file. The reason for more than one "detector" term to describe a sub detector is explained below.

GEAR is written in C++. All the parameters of different sub detectors are stored through an interface. Particular implementation of interfaces for the magnetic field, the Vertex Detector (VXD), the TPC and the calorimeter have been provided by GEAR. Each implementation corresponds to one "detector" term in the output file. That means the general description of the geometry of these ingredients are the same for all the simulation programs.

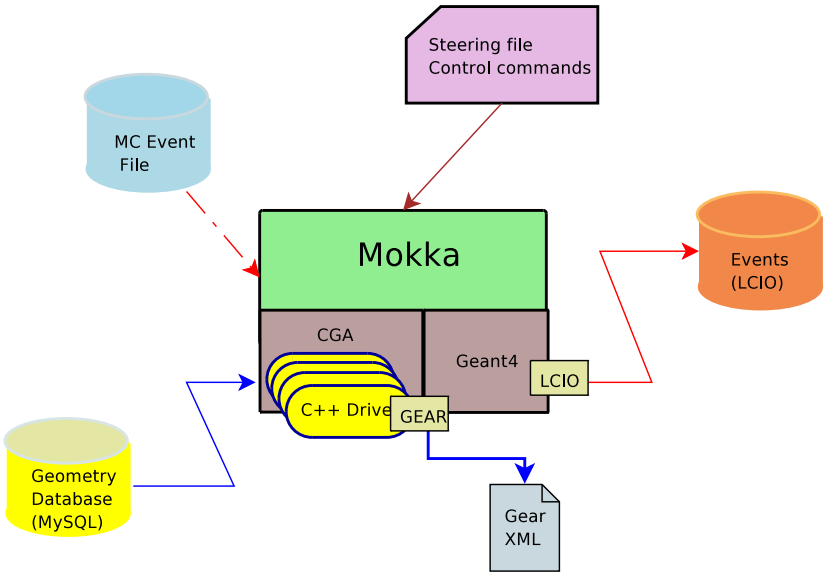

Figure 5.2: The relation between Mokka and other tools.

For example, the VXD is assumed to consist of a number of layers. Each layer is composed of rectangle ladders uniformly distributed in a circle around the Interaction Point (IP). A sensitive volume is attached to each ladder. The parameters used to describe a VXD include the number of layers, number of ladders, the radiation length, length, width and offset of ladder and sensor, etc. The distance property of the ladder (the sensor) are counted as the distance from the IP to the inner surface of the ladder (the sensor). The implementation of the interface for VXD in GEAR provides a variable to describe the gaps between ladders along the beamline direction, but it can't distinguish the different gaps in different layers. The additional information about gaps can be stored in other "detector" term related to the VXD in the output file. That is why a detector may be described by several "detector" term in the output file.

The GEAR toolkit is used by Mokka to generate the description of detector geometries. And most processors within the Marlin framework depend on the description provided by the GEAR XML file.

5.3 Mokka

The Mokka program is a powerful and flexible full simulation program for the ILC detectors. It was originally developed in 1999 for the detector studies for the TESLA TDR. Nowadays, it provides detailed simulations for various detector models in ILC, and is chosen as one of the standard simulation programs for the optimization of the ILD detector.

Mokka is a complex application written in C++. It depends on many other software tools. The relation of Mokka to other tools is illustrated in Fig. 5.2.

Mokka is based on the Geant4 toolkits [57, 58]. The Geant4 toolkit is written in C++ and used for the simulation of the passage of particles through matter. It covers a wide range of physics processes, including electromagnetic, hadronic and optic processes, and a wide range of energies from 250 eV to the TeV scale. It also provides a number of classes and functions to handle complex geometries. Geant4 is widely used in high energy experiments and provides a solid basis of Mokka. Furthermore, Geant4 provides a visualization system for the detectors and events, which is very useful in the development of Mokka drivers for sub detectors.

Mokka relies on a Common Geometry Access (CGA) interface to access the geometry database and build detector geometries. A detector model is expressed as a set of sub detectors. Their relations are stored in the database. The parameters of a sub detector and corresponding geometry driver name are also kept in the database. The geometry driver is a piece of code plugged into CGA. The task of a driver is to read parameters of the sub detector from the database, build the sub detector geometry in the simulation and output the geometry information when needed.

The geometry database is implemented with the MySQL package [63]. An official geometry database is provided by École Polytechnique. Users of Mokka can easily setup their own databases. By now, Mokka provides many detector models based on different detector concepts such as LDC and SiD.

As a simulation program, Mokka can read the Monte Carlo event files produced by event generators like Pythia [64] in HEPEvt format. [65]. Mokka can also perform simulation by using events generated from its internal particle gun, especially in the studies on the performance of one sub detector or comparison with testbeam results. The LCIO persistency framework is adopted by Mokka as the default format of output file. With the help of GEAR, Mokka is capable to generate the geometry description of a detector, which can be used by the digitization and reconstruction program.

Mokka is initialized and controlled by a steering file. It can also be controlled by interactive commands. The user can decide which detector model or sub detector need to be simulated. The ingredients of a detector model can be easily removed or replaced.

5.4 Marlin

Marlin is a generic C++ framework for the reconstruction and analysis of LCIO data. It provides a platform to develop and execute a number of computation codes.

The framework allows to implement every computation task as a separate module called "processor". The tasks may be very simple, such as filling histograms. They may be as complicated as pattern recognition and track finding. The LCIO data model is not only used for input and output, but also for the transfer of data from one processor to another processor. An example of full reconstruction within the Marlin framework is illustrated in Fig. 5.3. The main program reads the data event by event from LCIO files, creating an LCEvent which hands data to the processors performing different tasks. The processors are permitted to read and add collections to the LCEvent. The program is steered via an XML file which contains

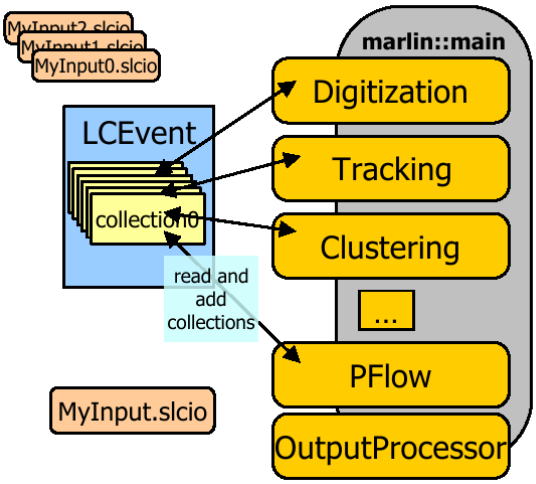

Figure 5.3: A schematic view of the Marlin framework.

the processor parameters and the order of processors to be used. The steering file provides a mechanism to select processor for specified computation task and makes it unnecessary to recompile the code.

Marlin implements a framework within which many codes for different purposes are developed. These codes may be processors to perform computation tasks, such as the MarlinReco package, which is a set of processors for the event reconstruction. The codes may be used as utilities for Marlin and other processors, such as the MarlinUtil package, which separates from Marlin and provides utility classes to facilitate reconstruction. The MarlinReco, PandoraPFA [44, 66, 45, 67] and PFOID [68] packages are used in our studies. A brief introduction about these packages is given below.

5.4.1 MarlinReco

MarlinReco is a complete set of processors for event reconstruction at the ILC based on the particle flow concept.

The processors used in our studies can be classified into the following categories:

- **Tracker Hit Digitization:** Two different digitizers are available for the vertex system. In the VTXDigiProcessor, simulated hit positions are smeared according to Gaussian distributions and a prior specified resolution in r-ϕ and z. It also performs the digitization in the Silicon Inner Tracker (SIT) with the same algorithm. A more sophisticated VTXDigitizer, specifically developed for DEPFET pixels with the fully depleted silicon bulk, takes the charges deposited in the silicon and the drifting of charges with the Lorentz effect of the magnetic field into account [69]. For the Forward Tracking Detector (FTD), the FTDDigiProcessor using the same algorithm as the VTXDigiProcessor

obtains hit positions. In the TPC, the TPCDigiProcessor performs Gaussian smearing of the simulated hit positions in r-ϕ and z according to the intrinsic chamber resolution.

- **Calorimeter Hit Digitization:** Two processors are developed for the conversion of simulated hits inside the Electromagnetic Calorimeter (ECAL) and the Hadron Calorimeter (HCAL) into calorimeter hits. The SimpleCaloDigi processor converts the simulated energy deposited in the active layers into physical energy by taking into account energy threshold and sampling fractions of ECAL and HCAL. The MokkaCaloDigi processor does nearly the same thing. In addition, it has the capability of merging the neighboring cells in calorimeters into a larger one, so that it can perform digitization for arbitrary detector geometries. Both processors are able to treat calorimeters in analogue and digital mode.

- **Tracking:** A complete set of tracking processors for tracking in the silicon detectors, the TPC and the whole tracking system are provided. The SiliconTracking processor performs stand-alone pattern recognition in the VXD, FTD and SIT. It performs tracking in the VTX+SIT and FTD separately and associates segments from the same track in the two parts together if possible. The LEPTrackingProcessor produces track collections from hits in the TPC by using the LEP tracking algorithm based on Kalman filters. Energy loss and multiple scattering are taken into account. The FullLDCTracking processor performs tracking in the whole LDC detector by linking track segments in the silicon detector and the TPC reconstructed by the previous two processors.

- **Clustering:** The PFA requires to assign the correct calorimeter hits to reconstructed particles. The TrackwiseClustering processor performs such a task of "clustering". It focuses on the spatial information of the hits and the dependence of the clustering procedure on the detector geometry is minimized.

- **Particle Flow:** The Wolf processor matches tracks and clusters, reconstructs particles and performs simplified identification of photons and electrons. The 4-momentum of charged particles are evaluated based on the tracking information. For the neutral particles, the 4-momenta are evaluated from the calorimeter information. Identification of γ and e is based on the ratio of energy deposited in ECAL to the total energy of cluster.

5.4.2 PandoraPFA

The PandoraPFA package provides a more sophisticated implementation of PFA than the Wolf processor in MarlinReco. It performs both calorimeter clustering and particle flow in a single processor.

The algorithm has eight main stages [45, 66]:

1. **Preparation:** The stage includes the identification of the Minimum Ionizing Particles (MIPs) and finding of non-isolated hits.

2. **Loose clustering in ECAL and HCAL:** The clustering starts from the inner layer. Tracks reconstructed with FullLDCTracking processor provided by MarlinReco are used as seeds. Hits are associated with nearby existing clusters and a cone based algorithm is used.

3. **Topological linking of clearly associated clusters:** In this stage, clusters with clear topological relations are associated. Photon identification plays a very important role in this stage–particles identified as photons are immune against association procedure.

4. **Grouping of clusters:** Tracks and clusters are temporarily associated. The energy-momentum relation between track and cluster is used to determine whether an association is valid.

5. **Iterative reclustering:** If the energy of the clusters and the momentum of corresponding track are inconsistent, reclustering is necessary. The suspicious cluster is split by changing the parameters of clustering until a sensible energy-momentum match is obtained.

6. **Photon recovery:** The photons identified before are merged to nearby clusters by using the energy-momentum relation. This is done by projecting the hits to the plane perpendicular to the radial vector and searching for peaks near the point where track intersects with ECAL.

7. **Fragment Removal:** This stage is applied to all non-photon neutral clusters. Cuts are performed to determine if the neutral hadron candidates are true neutral particles or fragmentation of other clusters.

8. **Formation of final Particle Flow Objects:** The Particle Flow Objects (PFOs) are created from previous results of clustering. These PFOs are treated as reconstructed particles and added to the LCIO data structure. Like in the case of Wolf algorithm, tracking information is used to determine the four-momentum of the particle.

The performance of the PandoraPFA algorithm has been studied with samples of $Z \rightarrow u\bar{u}, d\bar{d}, s\bar{s}$ decays. Together with the FullLDCTracking processor, $\delta_E/E < 3.6\%$ is achieved for jet energies ranging from 45-250 GeV [67].

5.4.3 PFOID

The PFOID package provides a Marlin processor for particle identification. It is important to discriminate electrons, muons and pions. Different particle types generate distinctly different distributions of cluster shape variables, such as average hit density, weighted mean distance of hits to the track extrapolation into calorimeter volume, ratio of energy deposited in ECAL to the total energy in cluster. The probability density functions (pdfs) of these distributions are used by the PFOID package to construct likelihoods for the following particle hypotheses: electron, muon, and charged hadron. The highest likelihood defines the particle ID.

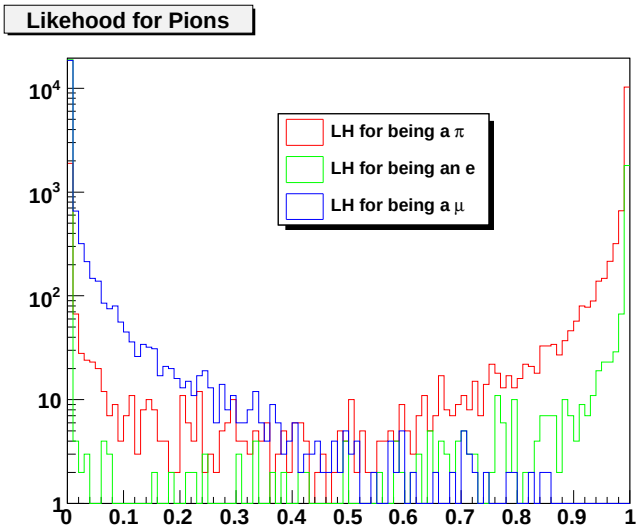

Figure 5.4: The likelihood calculated with the PFOID package for PFOs reconstructed by the PandoraPFA processor. These PFOs should be pions.

The performance of the PFOID package is tested together with the Wolf processor in MarlinReco package [68]. About 99.5% of the electrons are identified correctly, while the rest 0.5% are identified as pions. About 94% of the muons are identified correctly, with the rest identified as pions.

We have also tested the package with the PandoraPFA package for the identification of pions which energies ranging from 0.5 GeV to 150 GeV. The likelihood distributions are plotted in Fig. 5.4. About 89% of the pions are identified correctly. Only 0.7% are misidentified as muons. About 10% are recognized as electrons while the rest are identified as other particles.

Chapter 6

Simulation of the DEPFET vertex detector

A detailed simulation is necessary to study the performance of the DEPFET vertex detector (VXD) at the ILC.

Simulation codes for the DEPFET VXD in the LDC and SiD detector concepts have been developed within the framework of Mokka. The detailed description of the laddered structure of the DEPFET vertex detector, as proposed in the DEPFET report is implemented. The codes are tested and used to study the impact parameter resolution of the DEPFET VXD.

6.1 Developing new drivers for the Mokka program

As introduced before, the Mokka program uses the so called "drivers" to access the geometry database and build the detector geometry. In general, each sub detector is constructed by one driver. Our simulation codes for the DEPFET VXD are also developed as drivers of Mokka. For the main program of Mokka will access the database "**models03**" to find out the relationships between the detector models and sub detectors, the drivers must be registered in that database.

Fig. 6.1 shows the structure of the most important tables in the "**models03**" database and their relationships. With the table **ingredients**, different models and sub detectors are connected together. The table **model** contains the name, description and corresponding detector concept of different models. The information of a driver for one sub detector is recorded in the table **sub_detector**. The "*db*" column of this table gives the name of the database which contains the detailed parameters of the detector.

In general, the Mokka program is used to simulate one detector model. The sub detectors are found from the **ingredients** table and corresponding drivers are loaded. The Mokka program can also be used to simulate one single sub detector. In this situation, the driver for this sub detector is found directly from the **sub_detector** table. Therefore, at least the

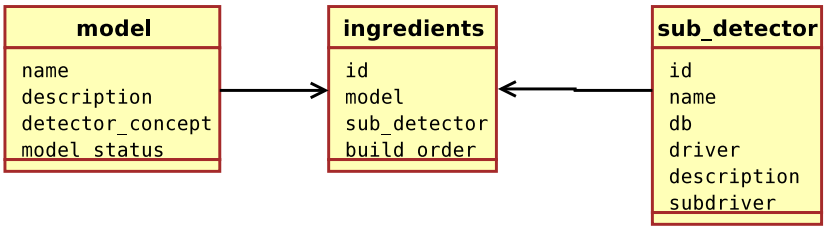

Figure 6.1: The important tables in the **models03** database of Mokka.

information of a driver should be inserted into the **sub_detector** table to make it usable. If the driver needs to access parameters of the corresponding sub detector, a database has to be created for it.

Thus the tasks of developing new drivers for Mokka include:

- Write C++ code of the driver, add it to the source tree of Mokka and recompile the whole program;
- Create a parameter database for the driver;
- Register the driver in the **models03** database, update related tables.

6.2 Simulation of the DEPFET VXD in LDC

The initial R&D of the DEPFET vertex detector was oriented towards TESLA. The proposed concept of a five layer barrel type vertex detector remains valid in the LDC concept of ILC. The DEPFET vertex detector in LDC follows this configuration.

6.2.1 The layout of the DEPFET VXD

The general layout of the vertex detector, foreseen for the LDC concept is plotted in Fig. 6.2. The radius of the innermost layer is about 15.5 mm, which is chosen to be as close as possible to the interaction point while keeping beam backgrounds controlled. The distance between adjacent layers is 11 mm. Each layer is composed of ladders. The number of ladders changes with the radii of the layers. Two specification of ladders with different sizes are used in the first layer and layer 2-5, respectively. The ladders used in the first layer have smaller length and width. The innermost layer covers the polar angle in a range of $|\cos\theta| < 0.96$, and the 5th layer extends to $|\cos\theta| = 0.9$. The detailed geometrical parameters are listed in Tab. 6.1. These parameters are also used in the design of the DEPFET VXD in LDC. The sensors are thinned to 50 μm to minimize the effects of multiple scattering.

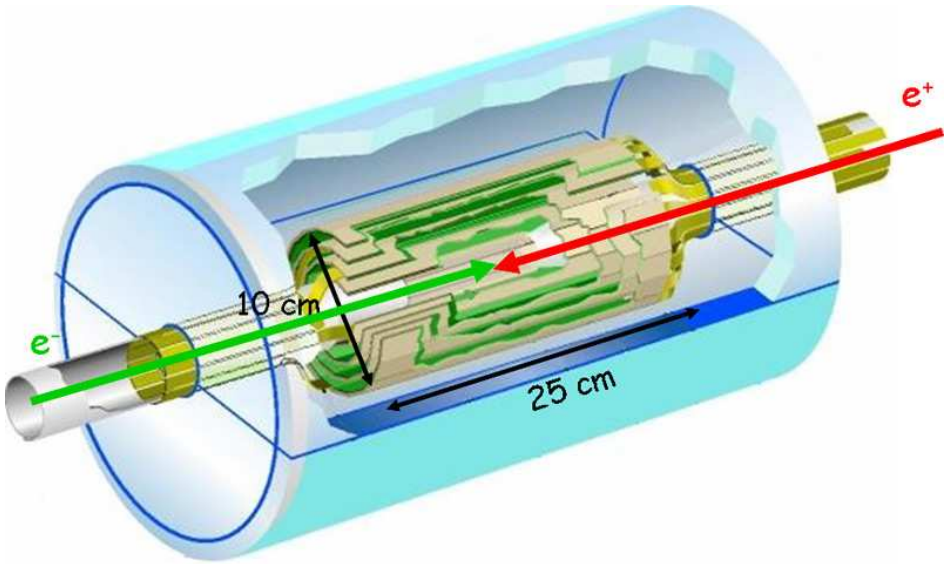

Figure 6.2: The proposed layout of the vertex detector in TESLA and LDC.

Layer	# Ladders	Radius (mm)	Ladder Length (mm)	width (mm)
1	8	15.5	100	13
2	8	26.0	2×125	22
3	12	37.0	2×125	22
4	16	48.0	2×125	22
5	20	60.0	2×125	22

Table 6.1: Default geometrical parameters of the DEPFET based vertex detector in LDC.

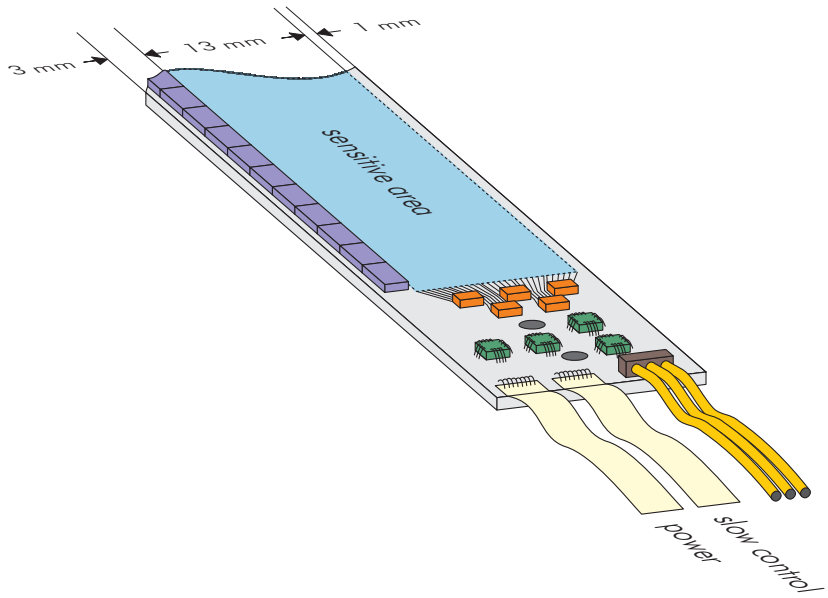

Figure 6.3: Sketch of one DEPFET module for the first layer.

6.2.2 Construction of a single ladder

The task of the C++ driver is to implement the geometry of DEPFET VXD. It starts from the construction of ladders. Ladders are the basic functional DEPFET modules with sensitive pixels, readout and steering electronics and supporting structures. Fig. 6.3 shows the sketch of a DEPFET module for the first layer. The dimensions of the thinned active area for the first layer are 100×13 mm^2. The sensors are supported by the silicon support frames. The readout electronics, power supply, slow control and data transmission are placed on both short ends of the frame volume. The steering chips are attached on the long side of the ladder with bump bonds.

The ladder constructed in the driver contains the sensitive area, the steering chips and the supporting frames only. The bump bonds and electronics in the short ends of the ladders are omitted for the time being for their relatively smaller volume located outside the fiducial volume.

The cross-section of a ladder is plotted in Fig. 6.4. One ladder is treated as the combination of four components – the sensor, the steering chips, the upper supporting frame and the lower supporting frame. The sensor and chips are implemented as silicon boxes according to their different geometrical sizes. The upper supporting frame is a silicon box with an etching hole in which the sensor is placed. It has the same thickness as that of the sensor. The lower supporting frame is also implemented as a box, but with two etching holes. It has the same length and width as those of the upper frame. The thickness of the lower supporting frame is 250 μm. All these components are created separately, and then assembled together according to their relative positions. The shape of these components is illustrated in Fig. 6.5. A detailed description of the parameters used in the simulation is given in Appendix A.

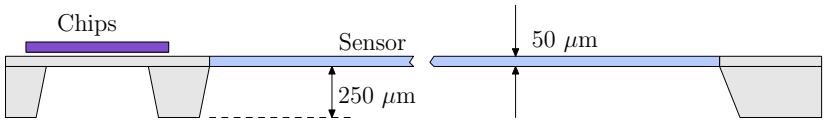

Figure 6.4: Cross section view of the layout of one ladder.

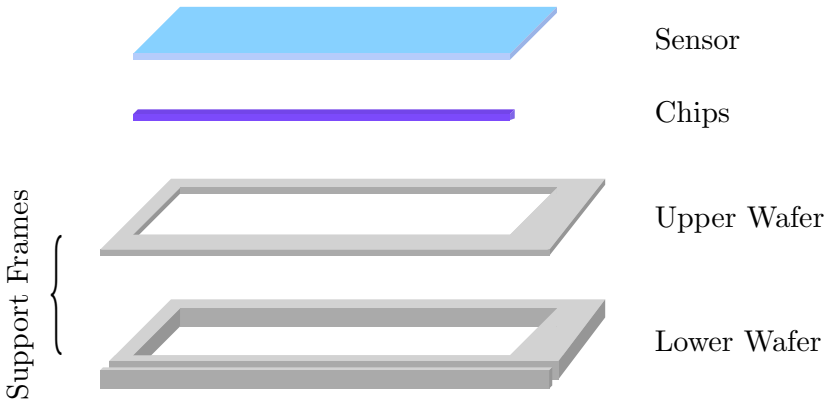

Figure 6.5: The four components of a ladder in the simulation.

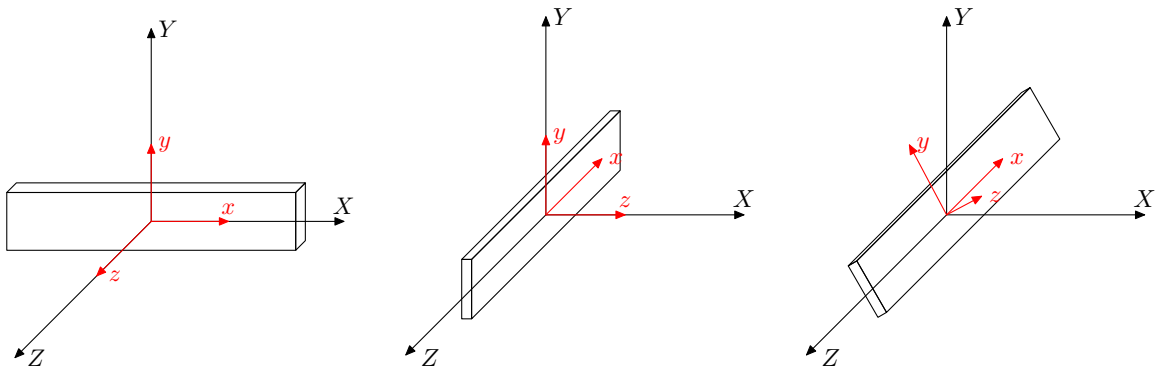

(a) The initial position of the ladder object.

(b) The position of the ladder after rotation around the y axis for $-\frac{\pi}{2}$.

(c) The position of the ladder after rotation around the x axis for $\frac{2i\pi}{n}$.

Figure 6.6: The rotation of the ladder object.

6.2.3 Placement of ladders

The ladders should be placed around the beamline to form barrel layers. When a ladder is created, the center of the sensor is placed in the original point, and the plane of sensor is perpendicular to the beamline. Fig. 6.6(a) shows the initial position and orientation of one ladder together with the global coordinate, which is indicated by XYZ. The internal coordinate of the ladder is also given, and it is indicated by xyz. The internal coordinate has the same orientations as those of the global coordinate system in the beginning.

To place the ladder in its proper position, we need to rotate it first. According to the rules of the Geant4 toolkit, rotation of one object is relative to its internal coordinate system, and the relative position of the internal coordinate system to the object does not change. In the first step, the ladder is rotated around the y-axis by $-\frac{\pi}{2}$ to place the long side of the ladder parallel to the Z-axis, see Fig. 6.6(b). Then, the ladder is rotated around the x-axis, which is now anti-parallel to the Z-axis, to form a barrel layer. The angle of rotation depends on the number n of ladders in this layer and the order i of the ladder, and is given by $\frac{2i\pi}{n}$. The result of rotating one ladder in this step is given in Fig. 6.6(c). After the two steps, the ladder has the "right" orientation in the space.

But the center of sensor is still at the original point. The ladder should be shifted according to the radius of the layer. The translation distances x_{tr} and y_{tr} are given by

$$x_{tr} = R\cos\frac{2i\pi}{n}, \tag{6.1}$$

$$y_{tr} = R\sin\frac{2i\pi}{n}, \tag{6.2}$$

where R is the radius of the layer, n is the number of ladders in this layer in XY plane and i is the order of the ladder.

The translation in Z direction depends on the layer. The innermost layer has only one ladder in Z direction, so ladders in this layer do not need to be shifted along the Z-axis. In

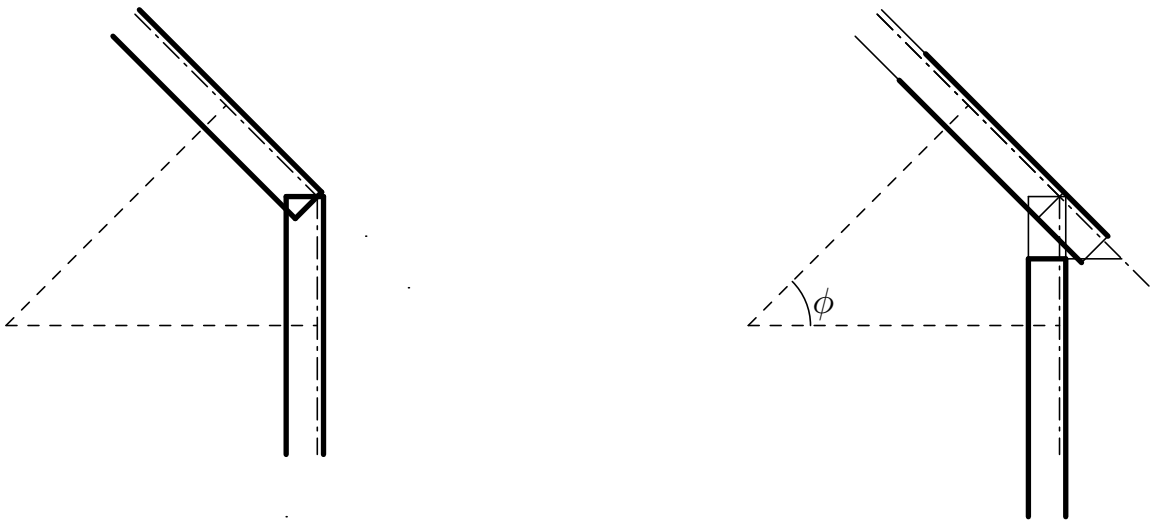

(a) Overlap between ladders without offset.

(b) Move ladders along the direction of their short side.

Figure 6.7: The offset of one ladder along the direction of the corresponding side of the polygon.

contrast, the remaining layers have two ladders in the Z direction. The shift distances z_{tr} of ladders are given by

$$z_{tr} = \pm(D + \frac{1}{2}d), \tag{6.3}$$

where D is the distance from the center of the sensor to the long end without electronics, and d is the distance between the two ladders' ends.

The configuration of the vertex detector is designed to cover the full azimuthal angle. Ideally, sensors would only connect with adjacent ones in their edges to form a regular polygon. But the sensors have finite thickness and are supported by supporting structure. Hence, the ladders will overlap with adjacent ladders as shown in Fig. 6.7(a) if we just rotate and translate them as before. This is avoided by moving each ladder along the direction of the corresponding side of the polygon, which is shown in Fig. 6.7(b). The offset can either be set by hand or be calculated when the smallest distance between two adjacent ladders is given. The detailed offset calculation is given in Appendix A. The offset leads to a modification of the translation distance given in Eqs. (6.1) and (6.2). The modified translation distance are

$$x'_{tr} = R\cos\frac{2i\pi}{n} + d_o\sin\frac{2i\pi}{n}, \tag{6.4}$$

$$y'_{tr} = R\sin\frac{2i\pi}{n} - d_o\cos\frac{2i\pi}{n}, \tag{6.5}$$

where d_o is the offset.

Applying the above procedures, ladders are placed in their proper positions and the barrel-structure detector is formed, as shown in Fig. 6.8.

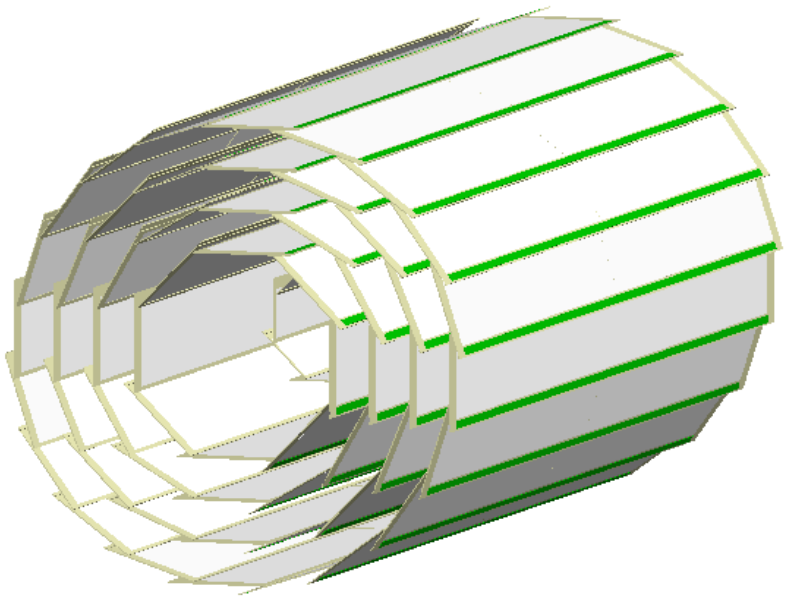

Figure 6.8: Implementation of the DEPFET vertex detector (ladders only) in the LDC concept. The configuration is also used in the ILD concept.

6.2.4 Support structure

As no mechanically detailed concept for the global support system of the VXD exist yet, the simulated support structure for the DEPFET VXD are limited to the outer support shell and endplates. The outer support shell is implemented as a beryllium cylinder with inner radius of 65 mm and length of 270 mm. The endplates are implemented as beryllium discs which are perpendicular to the beamline. Two specifications of end plates are used for the first layer and the remaining layers. The parameters of the endplates are listed in Tab. 6.2.

6.2.5 Gear parameters

The driver also prints out the geometrical parameters via the GEAR toolkit. These parameters are necessary for the digitization and reconstruction program.

The general description of a vertex detector in GEAR output is organized as a tree structure of "VXD–Layers–Layer–Ladder & Sensitive", which is shown in Fig. 6.9. In this description,

	z (mm)	thickness (mm)	inner radius (mm)	outer radius (mm)
type 1	±54.024696	0.049392	14.5	18
type 2	±135.024696	0.049392	23.2	65.224696

Table 6.2: The parameters of the end support plates.

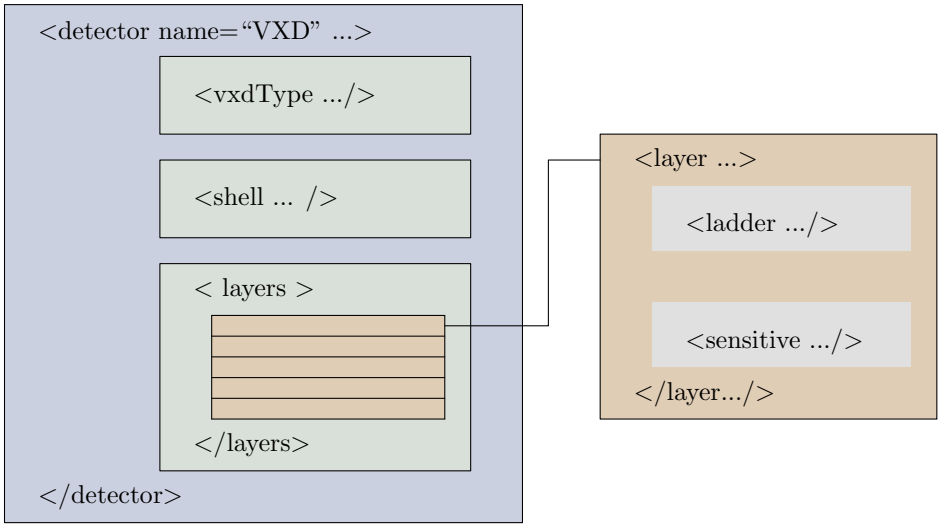

Figure 6.9: The description of VXD in GEAR toolkit.

ladder is used to support the sensitive area. For the self-supported DEPFET VXD, the support wafers are etched in the back side underneath the sensitive area, so the thickness of the ladder can be set to be 0. The width value of the sensor is given as the full width, 13 mm for the first layer and 22 mm for layers 2-5. By default, GEAR assumes each layer is composed of two ladders along the beamline. So the length of the "sensitive" in the first layer is set to be the half length of a sensor in the layer, or 50 mm. For "sensitive" in other layers, the property is set to be the full length of a sensor in those layers, or 125 mm. The gaps between the two "sensitives" are printed to a record of a detector "VXDInfra", and are set to be 0 and 0.04 mm for the first and remaining layers respectively. The record of detector "VXDInfra" also contains the parameters of the supporting structure, cryostat and electronics ends. Though some of these components do not exist in the simulation of DEPFET VXD yet, the parameters are kept and set to be 0, for they are needed by the reconstruction program.

6.3 Simulation of the DEPFET VXD in SiD

The DEPFET technology is also proposed to be used in the SiD concept. The layout of the vertex detector in the SiD is quite different from that in the LDC. In the SiD, the design of the vertex detector is based on barrel layers and endcap disks. The proposed layout is

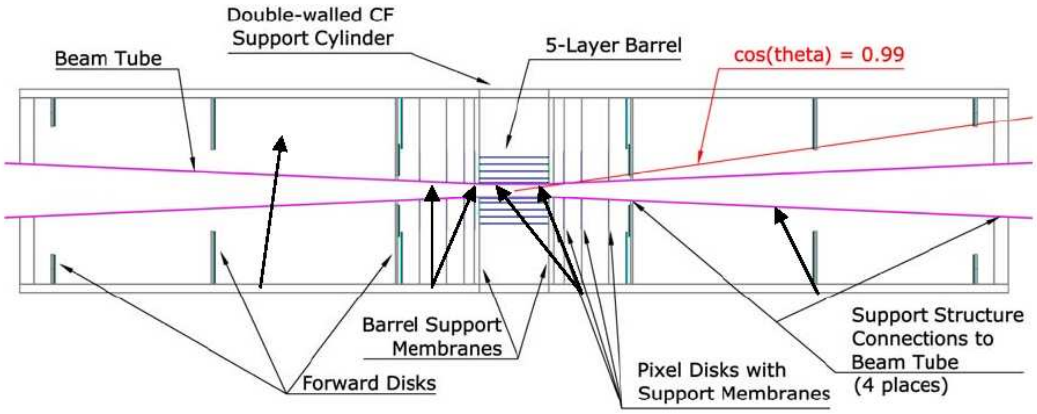

Figure 6.10: *R-Z* view of the vertex detector with support structure in SiD.

Layer	# Ladders	Radius (mm)	Ladder Length (mm)	width (mm)
1	8	14	120	13
2	8	22	120	22
3	12	35	120	22
4	16	47.6	120	22
5	20	60.0	120	22

Table 6.3: The geometrical parameters of the barrel part of the DEPFET based VXD in SiD.

shown in Fig. 6.10 and Fig. 6.11. Five barrel layers of equal length are positioned around the beampipe at radii ranging from 14 to 60 mm (A), or 15.2 to 60.7 mm (B). Four disk layers with sensors are attached to each end of the vertex detector by carbon fiber support disks ranging from 72 to 172 mm.

The proposed DEPFET vertex detector in SiD keeps the basic configuration of barrel layers and endcap disks. The geometrical size of the ladders in barrel layers will not change too much compared to that used in LDC. As all the barrel layers have the same length, each layer is composed of one ladder in z direction. The ladders in each layer have the same width as the ladders in corresponding layer in LDC. The lengths of DEPFET sensors in the SiD design are all 120 mm, which are longer for the first layer, but shorter for layers 2-5 in the LDC. The number of ladders in R-ϕ direction in each layer are 8, 8, 12, 16, 20. The parameters of DEPFET vertex detector in SiD are listed in Tab. 6.3. The implementation of the barrel layers in SiD is very similar to that in LDC. Sensors, chips, upper and lower support frames are implemented separately and ladders are assembled. The ladders are placed at the proper positions after rotations and translations.

The DEPFET based endcap disks are single sided sensors. For the time being, no support

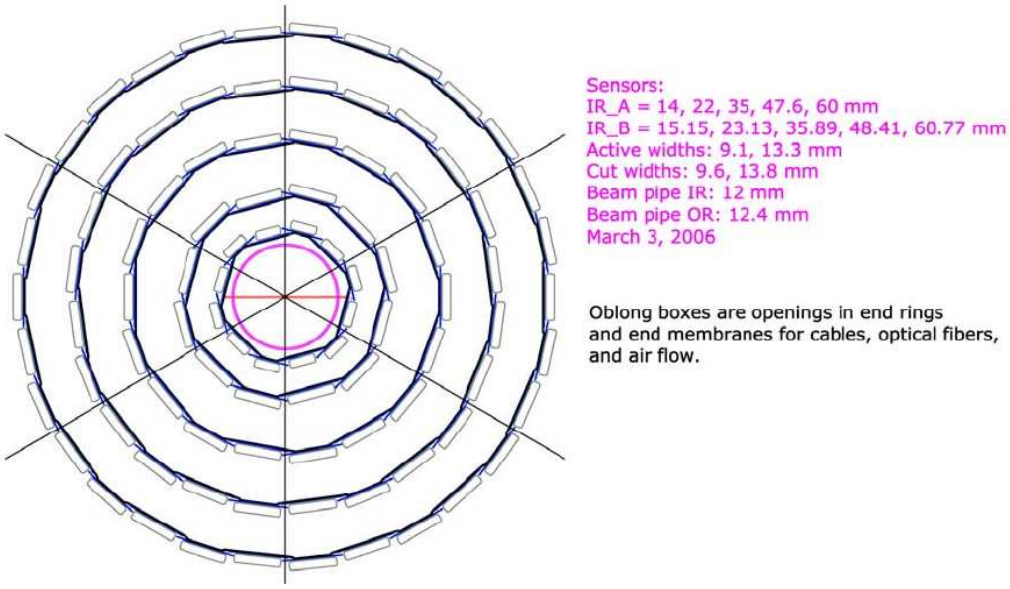

Figure 6.11: R-ϕ view of the vertex detector barrel in SiD.

Disk	Inner Radius (mm)	Outer Radius (mm)	Z (mm)	Thickness (μm)
1	14	71	72.278	50
2	16	71	92.043	50
3	18	71	123.432	50
4	20	71	171.693	50

Table 6.4: The geometrical parameters of the endcap disks in the DEPFET based VXD in SiD.

structures for the disks exist in code and only the sensors in the endcap disks are implemented. These disks have the same outer radius. The parameters of the DEPFET endcap disk sensors are given in Tab. 6.4.

The driver for the DEPFET vertex detector in SiD is used for the development of digitization program and study of the performance of the SiD vertex detector. The latter need the realistic description of the beampipe. As the present Mokka program provides no such a driver for the beampipe in SiD, an implementation of the beam pipe is also included in the driver. The parameters of the beam pipe are taken from the SiD outline document. Within the barrel part, the beam pipe is implemented as straight beryllium cylinder with inner radius of 12 mm and thickness of 0.4 mm. Beyond $Z = \pm 62.5$ mm, the beam pipe has conical shape with thickness of 0.875 mm. The half angle of the cone is around 2.773°.

The implemented DEPFET base vertex detector in SiD, with its barrel and end disk structure is shown in Fig. 6.12.

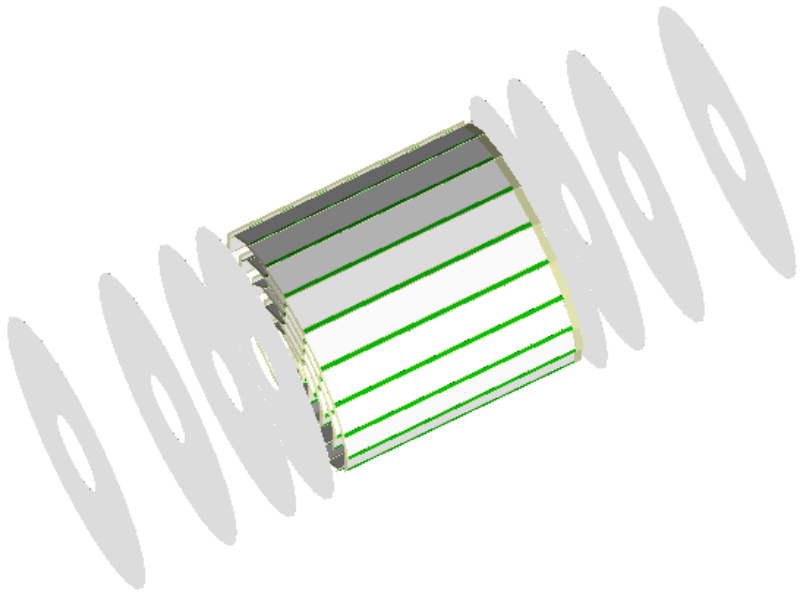

Figure 6.12: The DEPFET based vertex detector in SiD implemented within Mokka.

6.4 Study of the impact parameter resolution

One of the requirements for the vertex detector in ILC is to provide accurate impact parameter resolution. The impact parameter is the distance of closest approach between the interaction point (IP) and the trajectory of the charged particle. It is a key parameter to identify the heavy flavor quarks. The physics requirement on impact parameter resolution is

$$\sigma(IP_{r\phi}) = 5\mu\text{m} \oplus \frac{10\mu\text{m GeV/c}}{p \cdot \sin^{3/2}\theta}, \tag{6.6}$$

within $|\cos\theta| < 0.96$, where p is the momentum of the particle and θ is the polar angle.

The impact parameter resolutions of the LDC concept with DEPFET VXD is studied as a function of particle momentum for different polar angles. The driver for the DEPFET VXD is used.

The study starts from the simulation of muons with predefined energies and polar angle passing through the detector. The detector model LDC01_05Sc[1], which is an implementation

[1]More information of this model is given in Section 8.3 of Chapter 8.

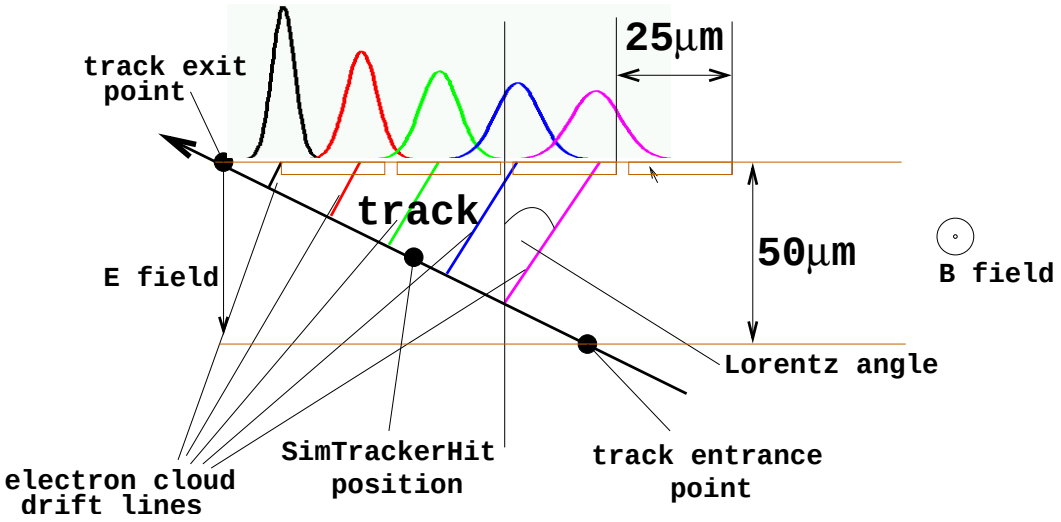

Figure 6.13: Simulation of the response of the DEPFET sensor.

of the realistic LDC detector, is used in the simulation. The detector is immersed in the solenoidal magnetic field of 4 T.

For our studies, we generated single muons with energies of 0.2, 0.5, 1, 2, 5, 10, 50 and 100 GeV and polar angles of 30°, 40°, 50°, 60°, 70°, 80°. The azimuthal angles of muons are distributed uniformly within $[0, 2\pi)$.

The detector simulation run produces hits left by muons passing through the VXD, the Forward Tracking Detector (FTD), the Silicon Inner Tracker (SIT) and the Time Projection Chamber (TPC). The response of the DEPFET VXD is simulated by the VTXDigitizer processor in the MarlinReco package. The processor approximates the track segment inside a given detector layer by line, with position and direction given by the simulated data. The line is divided into a number of subsegments. For each subsegment, charges are generated according to the Landau distribution as expected in Silicon. The charge drifts from the center of the subsegment to the collection plane of the detector with diffusion and undergoes a Lorentz shift in the magnetic field. The spread of the electron cloud on the collection plane is proportional to $\sqrt{L_{drift}}$, where L_{drift} is the drift distance. The charges on each fired pixel are the sum of the contribution from all the Gaussian distributed electron clouds. The simulation is illustrated in Fig. 6.13. Vertex hit positions are calculated from the fired pixels by using the center-of-gravity method. The single point resolution in r-ϕ and z as a function of track polar angle for different active sensor thicknesses and pixel sizes, has been studied, as shown in Fig. 6.14 [49]. Slight improvement of r-ϕ resolution towards small polar angle is explained by a larger deposited charge and consequently smaller inter-pixel signal fluctuations. The best z-resolution is obtained at $\cos\theta \sim 0.35$. For larger polar angle, the amount of fired columns along z decreases, increasing the z-position uncertainty. For smaller polar angle, the inter-pixel signal fluctuations are enhanced due to the larger fired cluster. In our studies, a sensor thickness of 50 μm with 25×25 μm^2 pixel size is used, following the proposal in the DEPFET report.

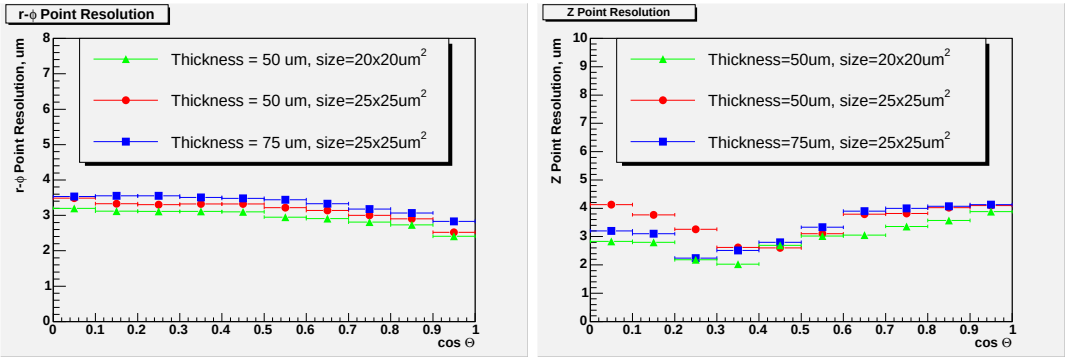

Figure 6.14: The spatial point resolution in r-ϕ (right) and z (left) as a function of track polar angle θ.

Track segments are reconstructed inside the silicon detectors and the TPC respectively, and combined together if possible. Tracking processors in the MarlinReco package are used to perform this task. The r-ϕ impact parameter d_0 is obtained by fitting the reconstructed tracks. The fitting procedure employs Kalman filtering, and takes into consideration the effect of multiple scattering and energy loss.

The impact parameter resolution as a function of momentum for different polar angles is plotted in Fig. 6.15. The dark (blue) lines in the plots are given by Eq. (6.6). Fitting the obtained resolution with the relation

$$\sigma(IP_{r\phi}) = a \oplus \frac{b}{p \cdot \sin^{3/2}\theta}, \tag{6.7}$$

yields $a < 5.0\mu$m and $b < 8.0\mu$m·GeV for all the polar angles we scanned. The light (green) lines in each plots indicate the fitting results. The DEPFET based VXD meets the ILC requirements well, for a sensor thickness of 50 μm and pixel dimension 25×25 μm^2.

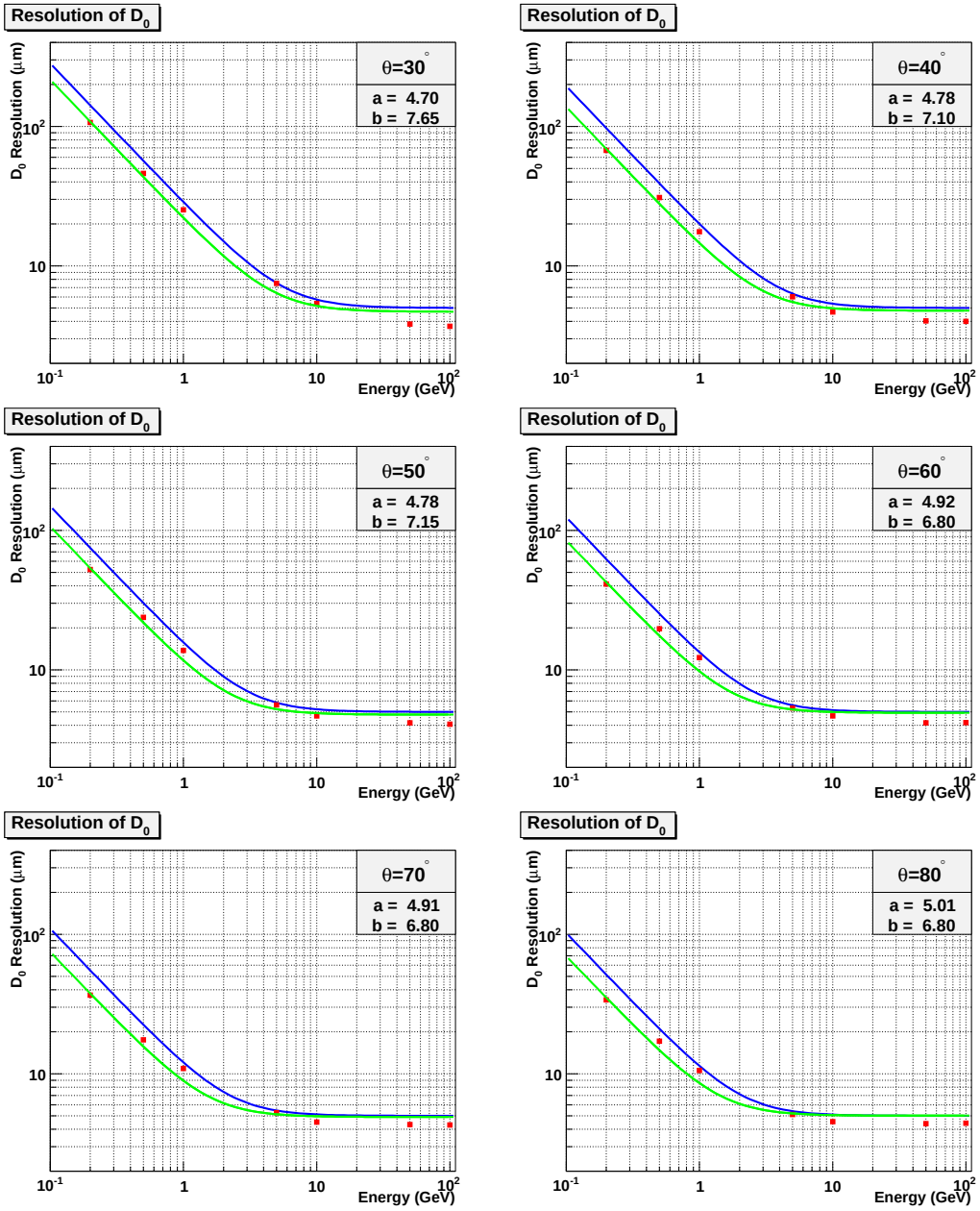

Figure 6.15: The impact parameter resolution as a function of momentum for different polar angles. Dark (blue) line: ILC requirement. Light (green) line: Fit result.

Chapter 7

Test Beam Analysis on Two-Track Resolution

The first prototype of the DEPFET matrices (called PXD4) with sensor thickness of 450 μm was produced in 2004 [70]. A number of tests and measurements have been performed on the 64×128 matrices using laser and source induced signals, as well as test beams. The first beam test took place at DESY with 6 GeV electrons in 2005. The results include that the Signal-to-Noise (S/N) ratio is larger than 110, the detection efficiency achieves 99.96% and the purity is around 97%. The resolution is 4.2 μm in the x-direction and 1.5 μm in the y-direction for the 36×22 μm^2 pixels [71,72]. Angular scans were performed, and the results have been used to tune and validate the GEANT4 simulation.

A DEPFET telescope consisting of 5 DEPFET layers was set up for the first time in the beam test at CERN in 2006. It was tested with a beam of 180 GeV pions. Extrapolation of the analysis results shows that the telescope would be capable of achieving submicron precision for beams with energy greater than 180 GeV [73]. In this chapter, we will discuss the analysis of the same data for the two-track-resolution.

7.1 Experimental Setup

A system has been developed for the testing of the PXD4 matrix by the DEPFET collaboration [70]. One CURO II chip is used for the readout of the matrix. Two SWITCHER II chips are used for the control tasks, one for FET gate control and another for clear. Fig. 7.1 shows a photo of one DEPFET test module. The matrix and the ASICs are placed on a PCB board where the output current of the CURO is converted to a differential voltage signal by an external amplifier. The voltage signal from the board is digitized by a 14-bit ADC in another board and stored in SRAM cells for readout. The slow control and readout of chips, the timing and the data transfer to PC via USB are executed by a SPARTAN 3 FPGA.

The Bonn ATLAS Telescope (BAT) [74] was used for tracking in the DESY test beam.

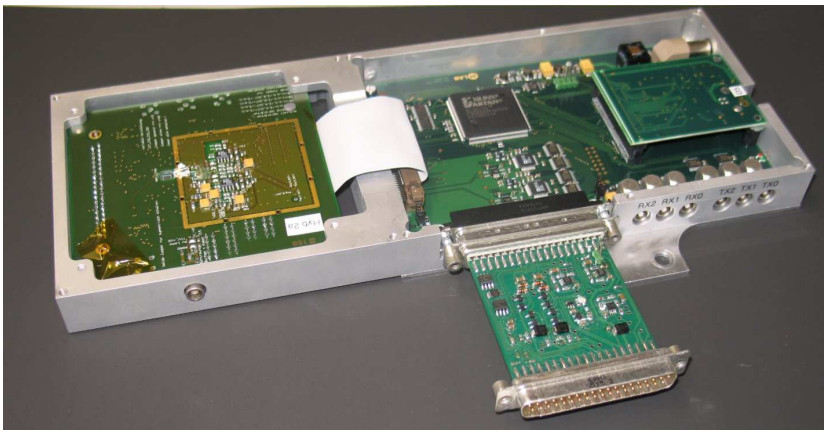

Figure 7.1: A DEPFET test module. The hybrid with the PXD4 matrix is on the left.

It consists of four identical planes of double-sided silicon micro strip sensors with a pitch of 50 μm each and provides a resolution of $\sim 4\ \mu m$. The resolution is worse than the intrinsic resolution of the DEPFET, which yields an uncertainty in the prediction of the hit positions.

To decrease this uncertainty, a telescope consisting of 5 DEPFETs numbered 2, 4, 5, 7 and 9, and spaced 25 mm apart was developed and tested with a beam of 180 GeV pions at the CERN SPS. Each DEPFET module has a matrix of 64×128 pixels. In four of these DEPFET modules, the pixel size is 36×22 μm^2 while one module (No. 9) has a pixel size of 33×23.75 μm^2. A photograph of the DEPFET telescope is shown in Fig. 7.2 .

One general task of reconstruction consists in the correct assignment of hits to the tracks. The two-track resolution, which is defined as the smallest possible distance where two tracks can be resolved, is an important parameter reflecting performance of the detector as well as the reconstruction software. The two-track resolution is determined from the test beam data. The strategy is as follows: Two events with one track each are merged together to create a new artificial event containing two tracks. All the information on the tracks is kept so that the distance between the two tracks can be decreased by moving the hits closer. Each time the distance between the two tracks is decreased, tracks are reconstructed to find out if the two tracks can still be separated. The procedures are repeated until the two tracks are no longer resolved. It is obvious that tracking plays an important role in the analysis.

The analysis starts from the readout of raw data and extraction of signals in each pixel. Hit clusters are searched around pixels with a signal higher than a given threshold in each DEPFET plane. The hit positions are then calculated based on the clusters. Finally, tracks are built from the hit information.

7.2 Format of raw data

The raw data is stored in binary format. Each data file has a unique run number. It is organized event by event. Each event has an 8-Bytes event header, in which the type and

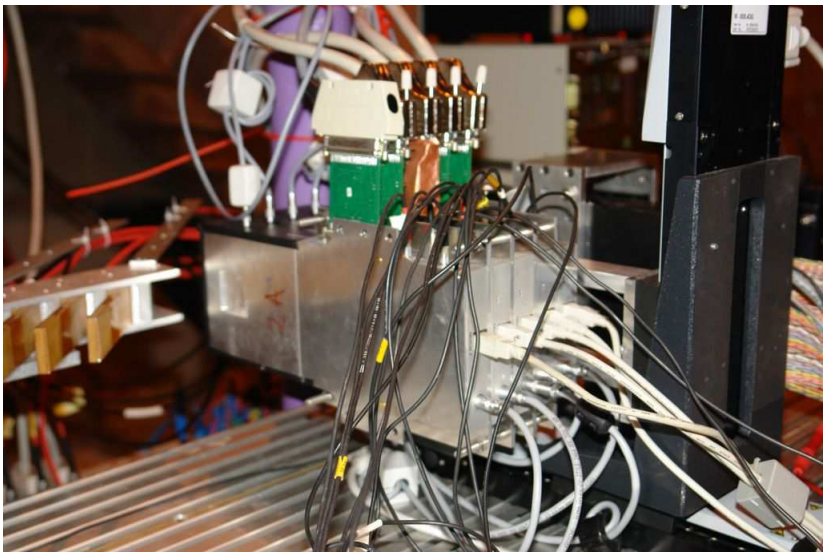

Figure 7.2: Photo of the telescope formed by 5 DEPFET planes.

size of this event is recorded. There are three types of event: The begin of run event (BORE) indicates the start of a new run and does not record signal data from the pixels. It contains the information about the order of the DEPFET modules. The standard event contains signal data of pixels on each DEPFET plane. For the standard event, data are recorded according to modules after the event header. A 12-Bytes module header is used to store the information related to the module, such as the type, number of the module and whether zero-suppression is enabled. The signal of each pixel is recorded in a 4-Bytes structure, where the lower 16 bits gives the ADC value and the higher 16 bits gives the position of this pixel. As the telescope consists of 5 DEPFETs of 64×128 pixels, $8 + ((64 \times 128) * 4 + 12) * 5 = 163908$ Bytes of storage space is needed by one standard event. For a run with about 30,000 standard events, the file exceeds 4.5 Gigabytes. The last type of event is the end of run event (EORE). In general, it is not used in the analysis.

7.3 Decomposition of raw signal

As mentioned before, the current signal of one pixel is converted to a differential voltage signal and digitized by an ADC. The digitized ADC value is stored in the raw data file. The raw signal of a pixel on one DEPFET module can be expressed as

$$S_{ij,N}^{raw}(k) = S_{ij,N}^{pedestal} + S_{j,N}^{common\ mode}(k) + S_{ij,N}^{random\ noise}(k) + S_{ij,N}^{signal}(k), \tag{7.1}$$

where i and j indicate the position of the pixel, N is the number of the module, k is the event number. The pedestals and common mode noise should be subtracted from the raw signal.

The pedestal is independent of the event number. Given that the average of the random noise is zero and the average of the common mode noise is a constant that can be absorbed

into the pedestal, the pedestal can be calculated by averaging the raw signals for each pixel in the absence of hits, or

$$S_{ij,N}^{pedestal} = \frac{1}{n_e} \sum_{k=1}^{n_e} S_{ij,N}^{raw}(k), \tag{7.2}$$

where n_e is the effective number of events for pixel (ij, N) after hit removal for a specific number of events. In general, the first 1000 events of a run are used to calculate the pedestal. The effective number can be obtained by the following steps: At first, the mean value $\bar{S}_{ij,N}^{raw}$ and standard deviation $\sigma(S_{ij,N}^{raw})$ of the raw signal are calculated. If the difference between the raw signal for a pixel (ij, N) in one event and the mean value is larger than $3\sigma(S_{ij,N}^{raw})$, the raw signal of this pixel is treated as a hit signal and will not be used in the calculation of pedestal in Eq. (7.2). The pedestal obtained for each DEPFET module in run 3421 are shown in Fig. 7.3.

The common mode noise is obtained by averaging the signal of a row after the subtraction of pedestals and removal of hits for each event. Since the lower and higher 32 columns of a DEPFET module are readout respectively by one ADC, the common mode noise has to be calculated for the two parts separately. Fig. 7.4 shows the distribution of common mode noise in DEPFET module 2. The common mode noise follows a Gaussian distribution. The distribution of common mode in other DEPFET modules looks very similar to that in DEPFET module 2. A correlation between the common mode noise of the two ADCs is observed. The correlation in DEPFET module 2 is plotted in Fig. 7.5.

The random noise is then calculated as the standard deviation of the signal after the subtraction of pedestal and common mode correction. Hits are removed by the $\pm 3\sigma$ cut. The noise of each pixel is depicted in Fig. 7.6 and the distribution are plotted in Fig. 7.7. Peaks are observed around 15 ADC counts in DEPFET module 2, 4, 5 and 7, while around 22 in DEPFET module 9. The long tail at higher values is due to pixels with higher noise. Fig. 7.6 shows that most of the high noise pixels are concentrated in columns. That means the high noise is mainly caused in the CURO. The noise information of each pixel will be used in the analysis of two track resolution.

7.4 Hits and clusters

Clusters need to be searched before the finding of hits, for the positions of hits are calculated based on the signals in the cluster pixels. Clusters are found by a clustering algorithm that first searches for the cluster seed, which is the pixel with maximal amplitude above 5σ threshold, where σ is the noise calculated before. Once a cluster seed is found, the neighboring 3×3 pixels around the seed are blocked and the searching procedures are repeated until no further seeds are found.

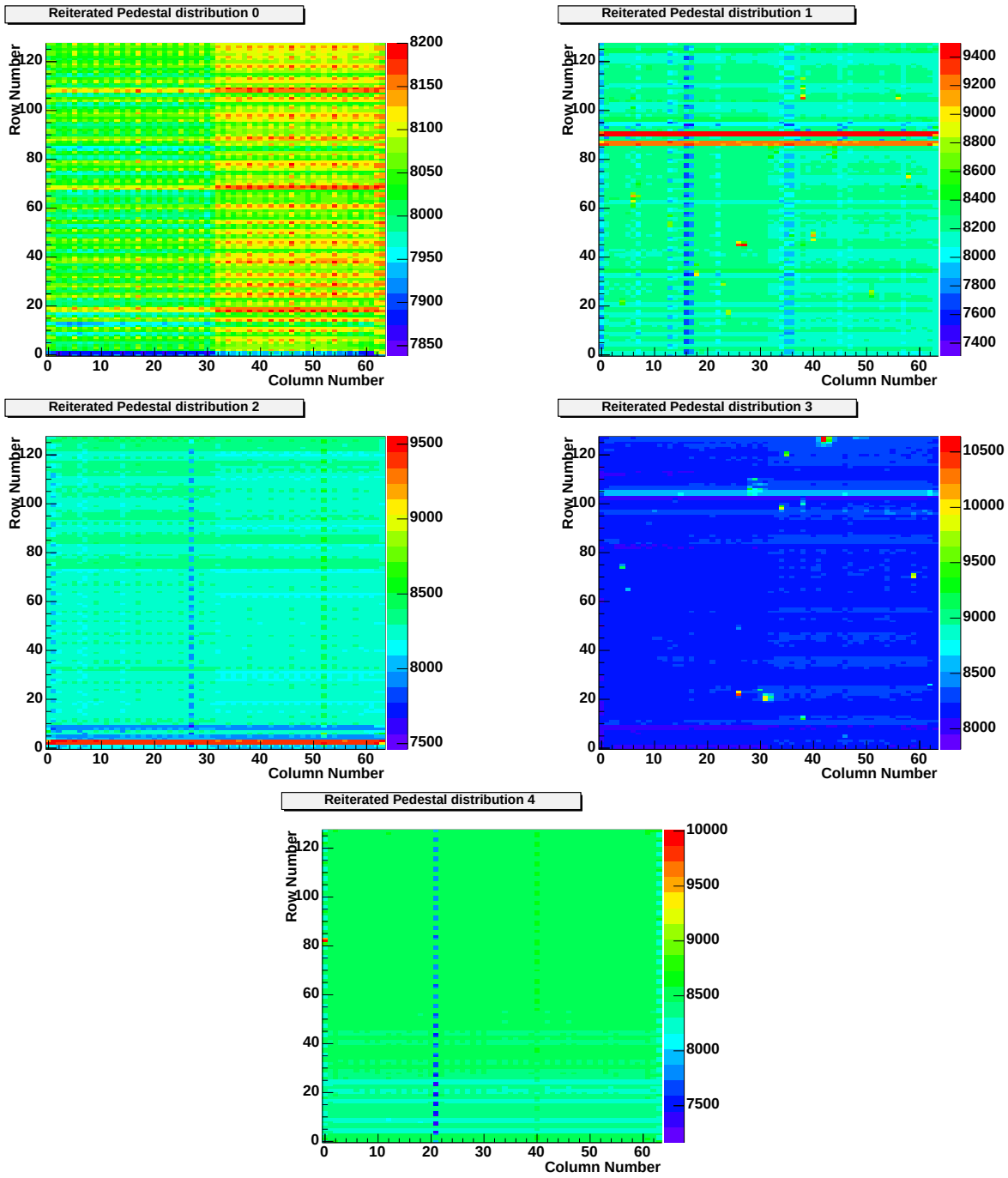

Figure 7.3: The pedestals obtained in each DEPFET module in run 3421.

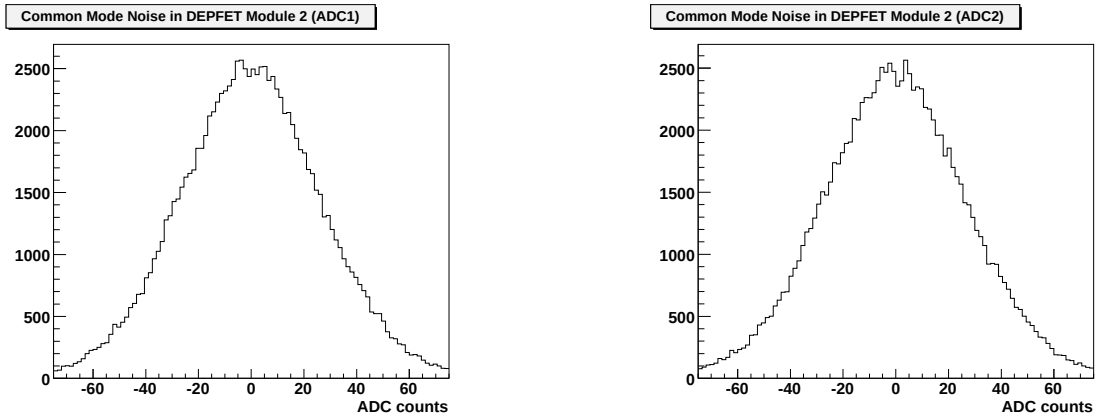

Figure 7.4: The distribution of common mode noise in DEPFET module 2.

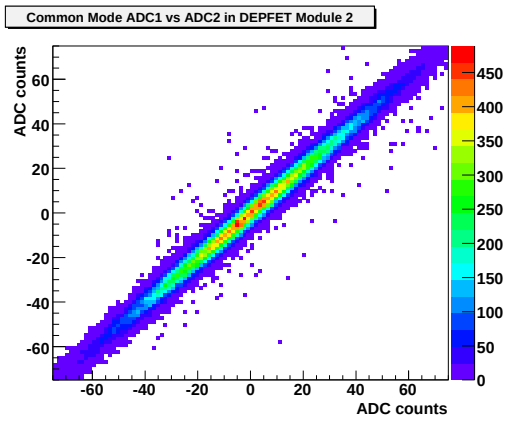

Figure 7.5: The correlation of common mode noise of two ADCs in DEPFET module 2.

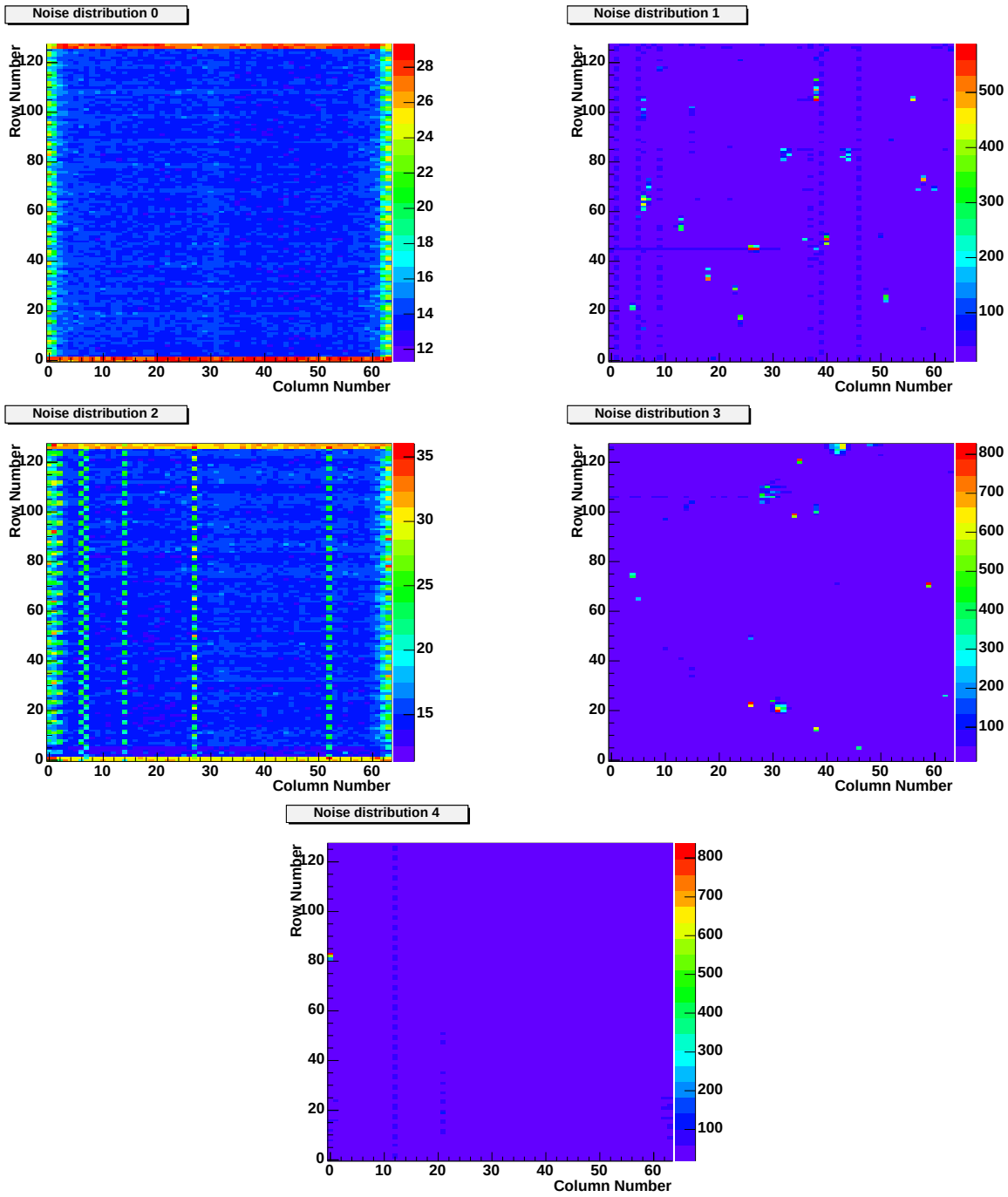

Figure 7.6: The random noise of each pixel in different DEPFET modules.

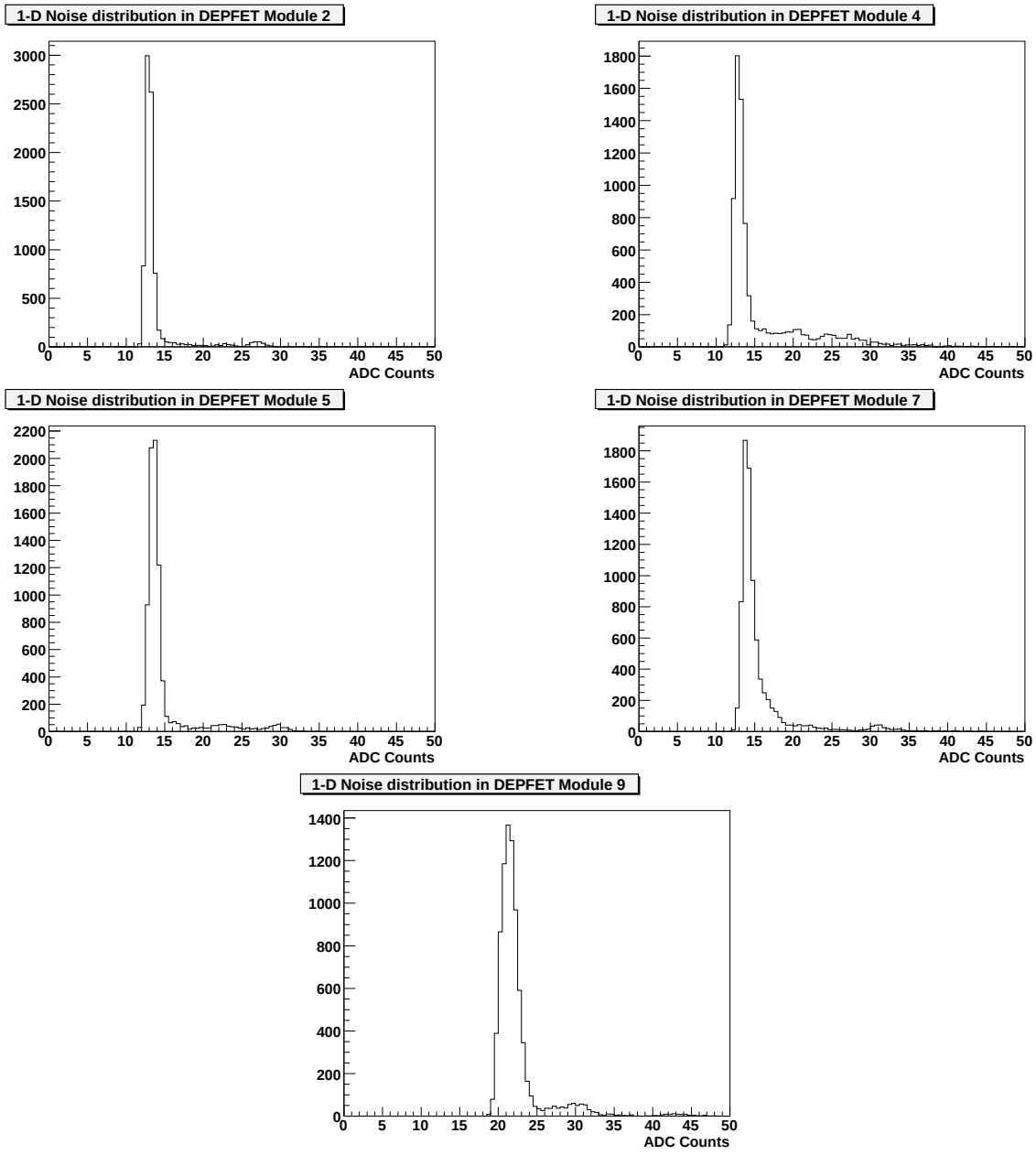

Figure 7.7: The distribution of random noise in different DEPFET modules.

7.4.1 Blocking of hot pixels

Some pixels occur much more often as seeds than other pixels. These pixels are "hot" pixels and should be blocked together with their neighboring 3×3 pixels.

The hot pixels are determined as follows: At first, the distributions of the number of times a pixel is found as seed are plotted. They should follow an the exponential distribution, which is used to fit the distribution. A cut is set to the point where the function takes the value of 1. The pixels which have higher frequency than the cut frequency are marked as hot pixels and blocked out. After these hot pixels are blocked out, seed finding procedures are performed again, and the process of hot pixel searching should be repeated, until no more hot pixels are found. In general, two iterations are enough for finding all hot pixels. Fig. 7.8 gives an example of seed frequency distribution after the first round of seed finding for run 3421. There are much more hot pixels in the DEPFET module 2 than other modules.

Fig. 7.9 shows the pixels recognized as seeds after two times of hot seeds removal for run 3421. From the first plot, we can find that most pixels on the right of DEPFET module 2 have been blocked out. This is very likely to be a problem of the ADC which readout the columns in the right handed side. For DEPFET module 4, 5, 7, most blocked pixels are concentrated in some columns, which can be seen clearly in Fig. 7.9. These phenomena are very likely due to the problem of CURO. The hypothesis could be tested by rebinding the DEPFET channels to different CURO channels.

7.4.2 Cluster signals

A cluster is the collection of pixels around a cluster seed. Only the pixels with a signal above a 2σ cut are used for the calculation of hit positions. Fig. 7.10 shows the signal distribution of clusters of 3×3 pixels after the blocking of hot pixels. It is suggested that the low signal clusters result from a CURO problem, except for the DEPFET module 9 and the right side of DEPFET module 2 [75]. Hence, the seed locations for the low signal clusters should be blocked out. The cluster signal distribution in DEPFET 9 is different from those in other modules. The reason is still unknown and being studied.

7.4.3 Hit position

The position of hits can be calculated in two ways. One is the Center-of-Gravity (CoG) method. In that method, the position is given by

$$\begin{aligned} x &= \frac{\sum S_i n_i^{col} x^{pixel}}{\sum S_i}, \\ y &= \frac{\sum S_i n_i^{row} y^{pixel}}{\sum S_i}, \end{aligned} \tag{7.3}$$

where the sum runs over all the pixel passing the 2σ cut in the cluster, S is the signal of the pixel, n^{col}, n^{row} are the column and row number of the pixel respectively, and x^{pixel}, y^{pixel} are the geometrical size of the pixel.

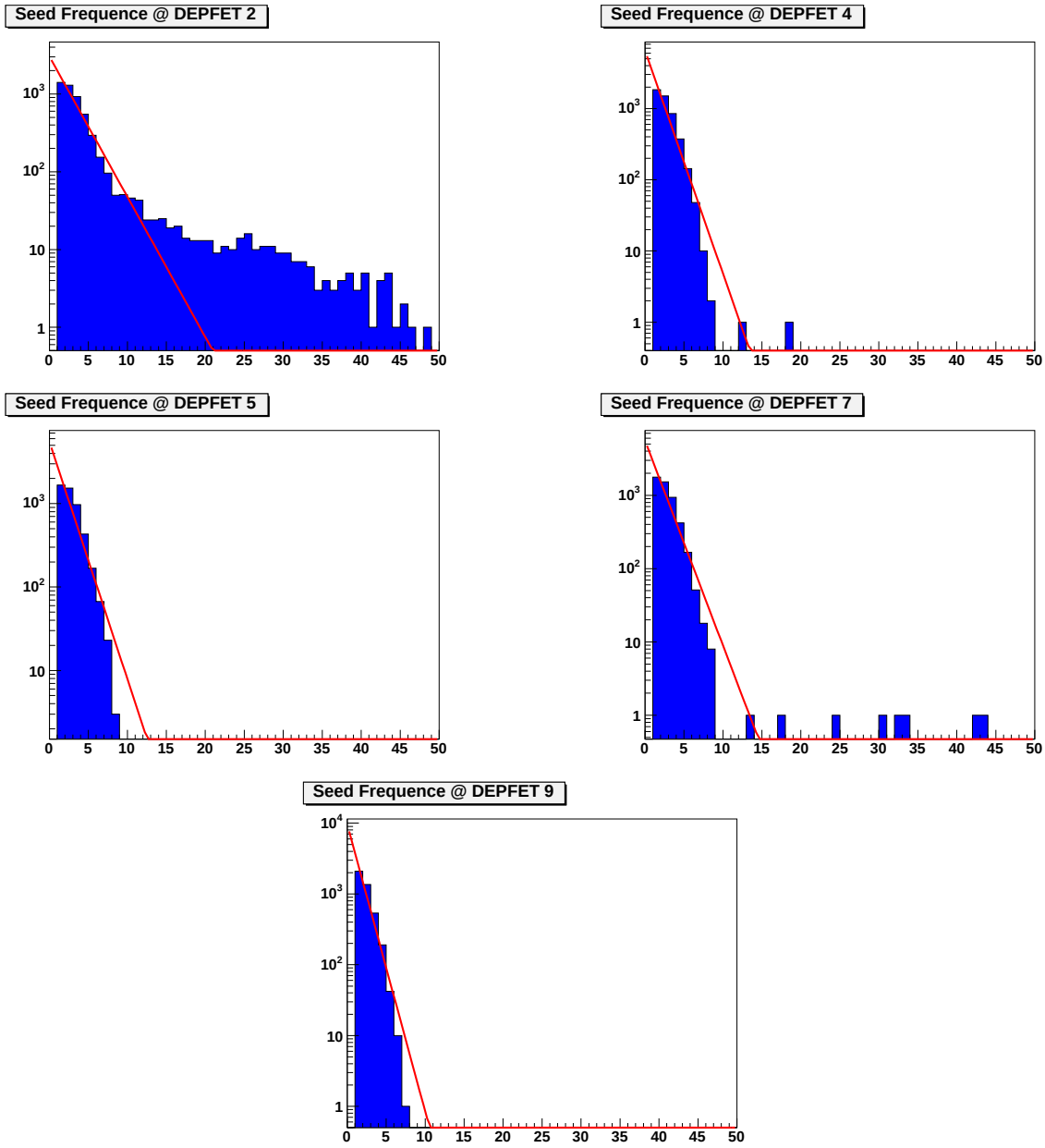

Figure 7.8: The frequency of a pixel recognized as seed in each DEPFET module after the first time of seed finding for run 3421. Cuts are given by set the value of fitting exponential function to be 1.

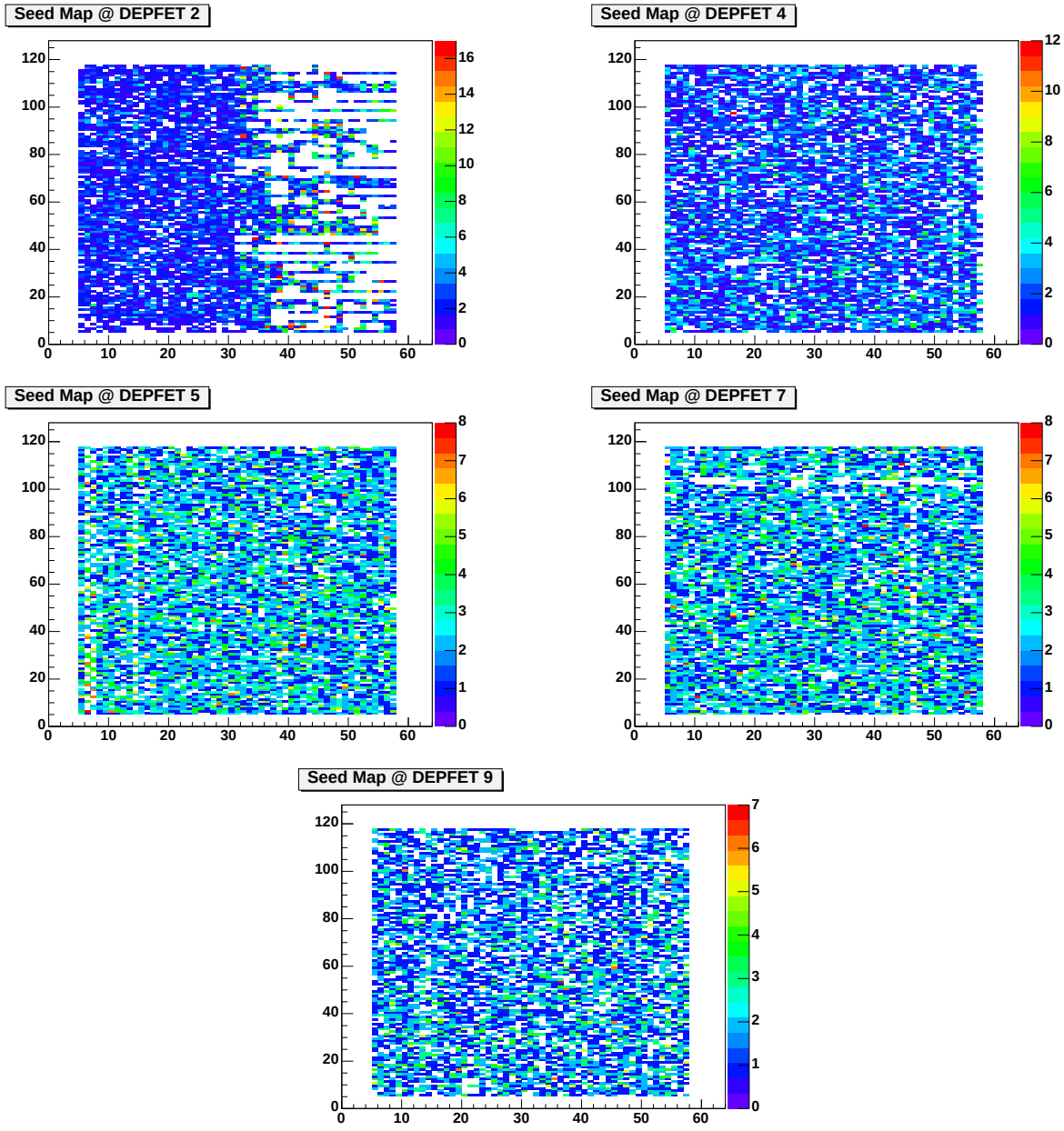

Figure 7.9: The pixels recognized as seeds in each DEPFET modules after 2 iterations of hot pixel search for run 3421. The color indicates the frequency of the pixel found as seed.

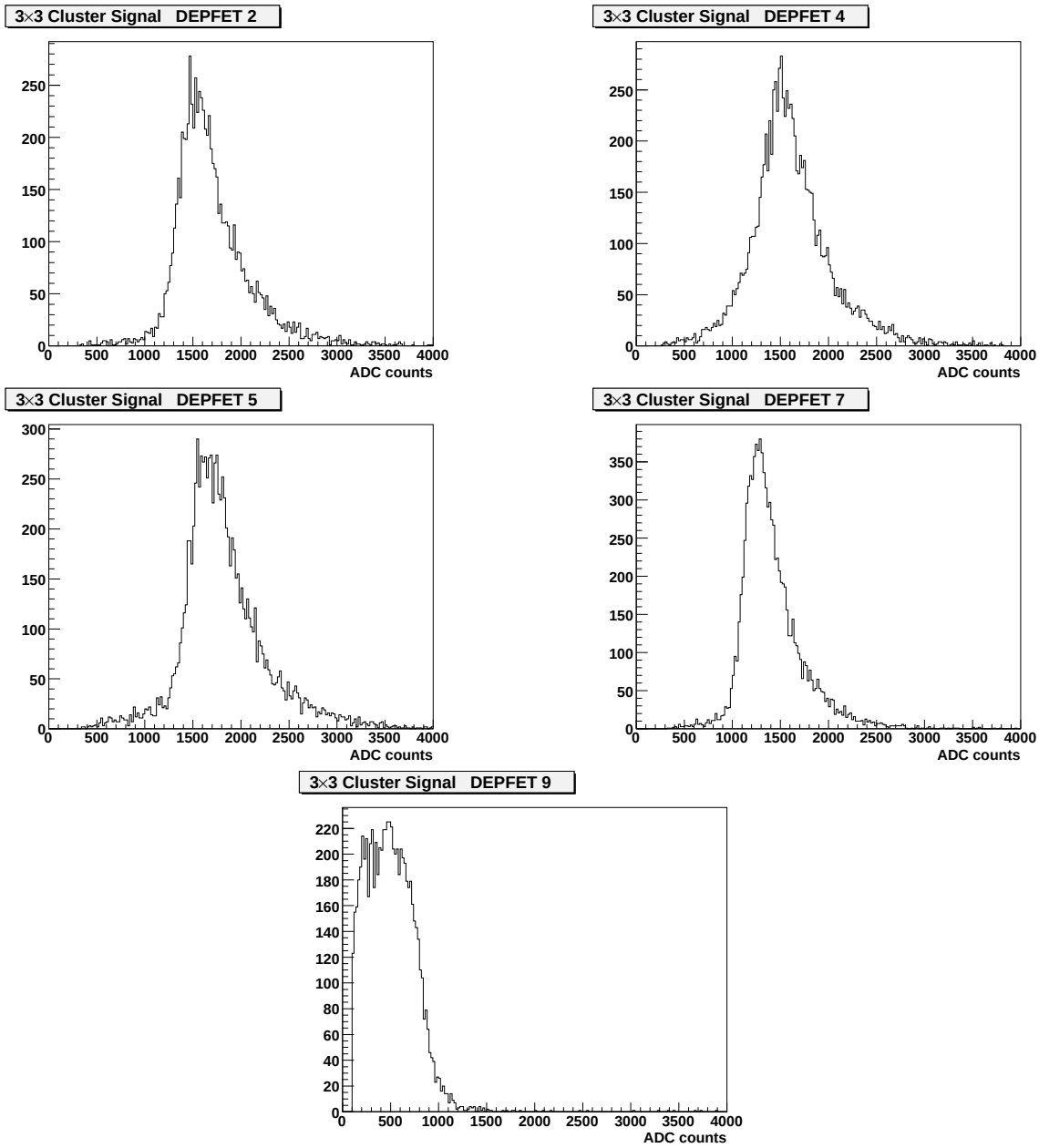

Figure 7.10: The signal distribution of cluster in ADC counts with 3×3 pixels for the DEPFET modules.

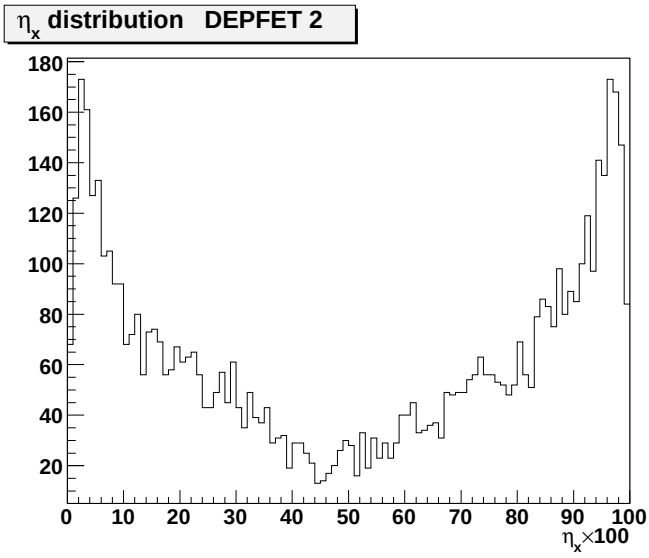

Figure 7.11: The distribution of η_x for DEPFET module 2.

Another way to calculate hit position is the η-algorithm. The distribution of charges collected by nearby pixels is used in this method. We take the x position of a hit as an example. In a cluster, only the column containing the seed and the column with higher signal is used to calculate η_x, which is defined as the fraction of the column signal in the right over the total signal of two columns, or

$$\eta_x = \frac{S_{right}}{S_{left} + S_{right}}. \tag{7.4}$$

It is clear that the value of η_x reflects the information of the x position of the hit: the hit should be close to the left column if η_x is close to 0, while it is close to the right column if η_x is close to 1. Due to the nonlinearity of the charge collection between pixels, the distribution of η_x is not flat. Then the x position of the hit is given by

$$x = x_{left} + x^{pixel} \int_0^{\eta'_x} f(\eta_x) d\eta_x, \tag{7.5}$$

where x_{left} is the x position of left column, x^{pixel} is the size of the pixel, $f(\eta_x)$ is the distribution function of η_x normalized between $[0, 1]$, and the η'_x is calculated in this cluster. The same method can be used to calculate y positions of hits.

Knowledge of the distribution function $f(\eta)$ is necessary in the η-algorithm. This can be obtained by studying all the clusters in a run analyzed. Fig 7.11 gives the distribution of η_x for DEPFET module 2. We can find that more charge is collected by the nearby pixel, which leads to the two peaks near 0 and 1.

Better resolutions are obtained by using the η-algorithm than the CoG method [72]. But for the study of two-track resolution, the simpler CoG method is used because precise hit positions are not necessary.

7.5 Track finding

7.5.1 Pre-alignment

Though the five DEPFET modules are placed 25 mm apart, they are not well aligned. Actually, the overlap region of the five DEPFET modules is very small. The hit positions calculated before can not be used directly in the tracking.

The pre-alignment is done by finding the correlation between the hit positions on different DEPFET modules. DEPFET module 5 is chosen to be the reference plane. The positions of hits for other modules are plotted against those for DEPFET module 5 for x and y respectively if they belong to the same event. The plots are shown in Fig. 7.12 and Fig. 7.13. Clear lines are observed in all these plots. They are given by the hits belong to the same track. Points away from the lines may come from the wrong combination of hits in one event or erroneous hits. These plots can be fitted with straight lines by setting a threshold cut of amount of hits for all the cells, which eliminates most of the points away from the lines. With the fitting function, we can project the hits on other DEPFET modules onto module 5. Then we can reconstruct tracks.

7.5.2 Tracking

As all the DEPFET modules are nearly parallel to each other, and the beams are approximately perpendicular to them, we assume that the hits in the same track would have nearly the same x and y coordinate. This hypothesis is used in the tracking procedure.

For each event, we start from the hit on DEPFET module 5. When a hit from other modules is added, it is mapped to DEPFET module 5 by using the fitting functions obtained in the pre-alignment procedure. The center of gravity of all the selected hits is calculated by setting equal weighting for all hits. If the largest distance from a hit to the center of gravity exceeds the geometrical size of a pixel, the hit is rejected and the center of gravity is updated. The procedure is repeated until all the hits in one events have been considered. The resulting track should contain at least 3 hits from different DEPFET modules.

The reconstructed track can be described with the coordinate (x_o, y_o) of the center of gravity of all the hits in this track on DEPFET module 5. Fig. 7.14 and Fig. 7.15 give the distribution of residuals in x and y direction of the hits relative to the center of gravity. The parameter σ given in each plot is not the track resolution, for the tracking model does not consider the mis-alignment of the DEPFET modules. The track resolutions should be better than those given in the plots. The deviation of the residual distributions from Gaussian distribution in several of the plots also results from the crude tracking model. But we can at least conclude that the hits really belong to the same track in each event.

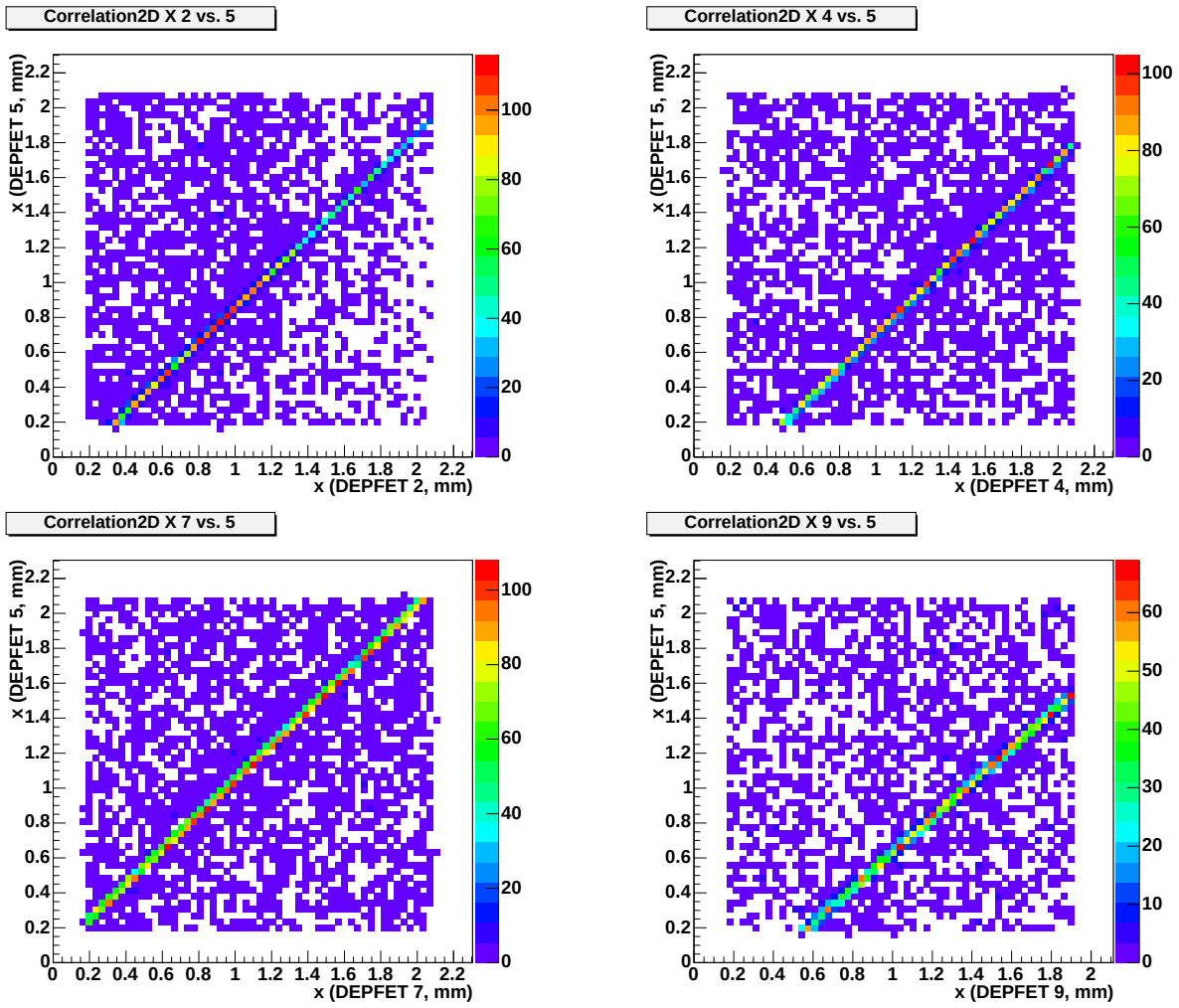

Figure 7.12: The correlation of x coordinates of hits for different DEPFET modules against DEPFET module 5.

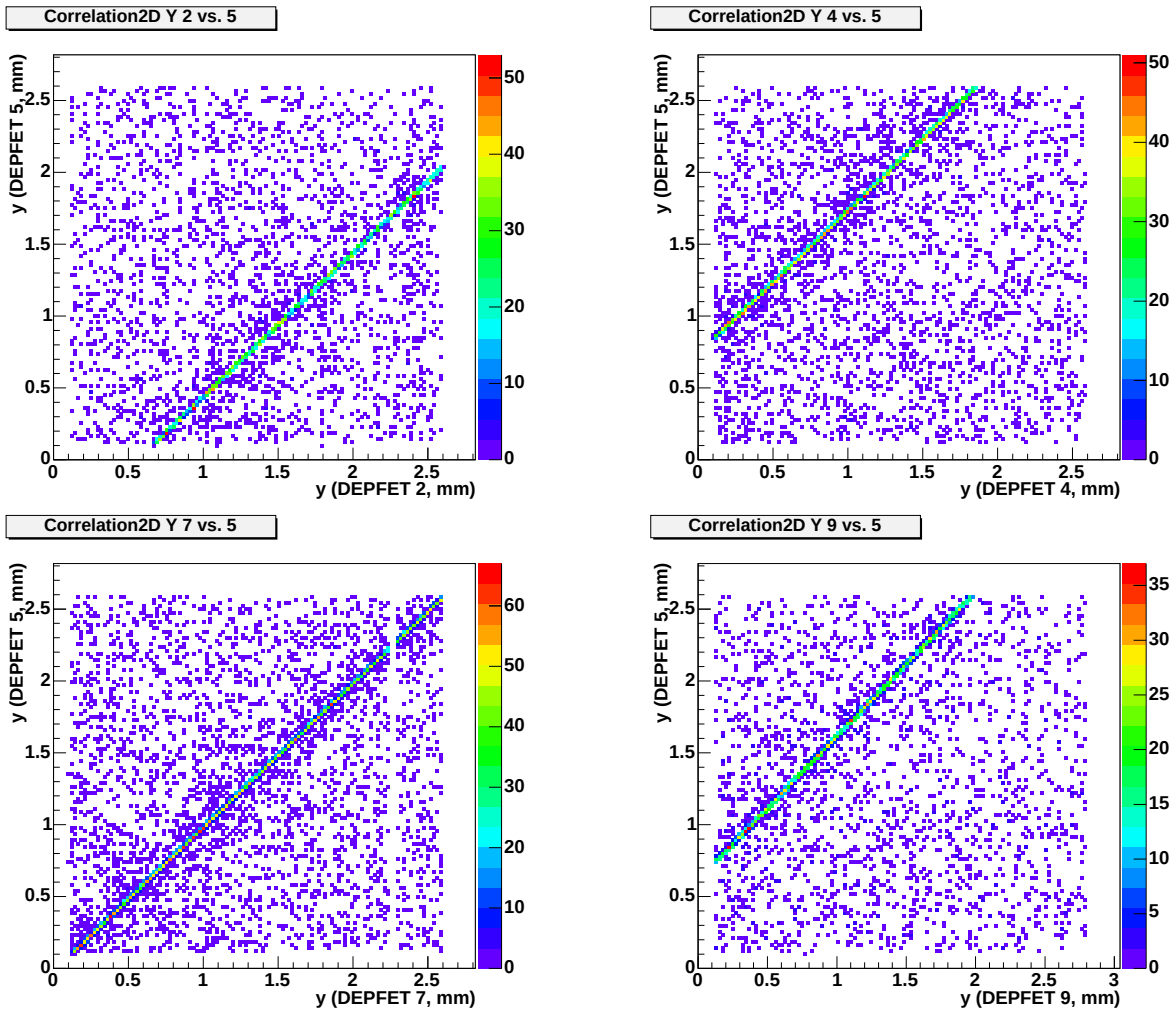

Figure 7.13: The correlation of y coordinates of hits for different DEPFET modules against DEPFET module 5.

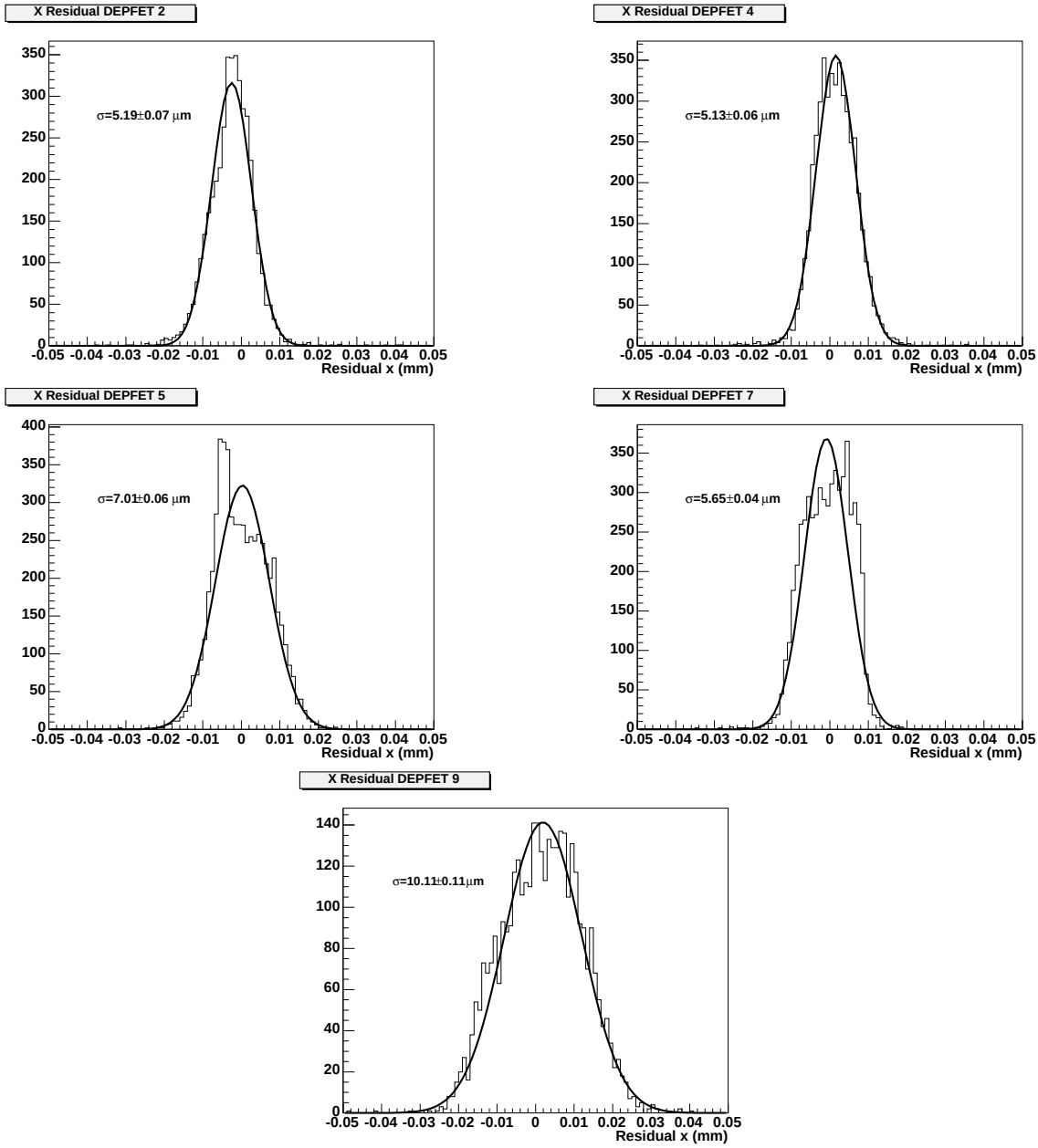

Figure 7.14: Residuals in the x direction of hits relative to x_o of the reconstructed track.

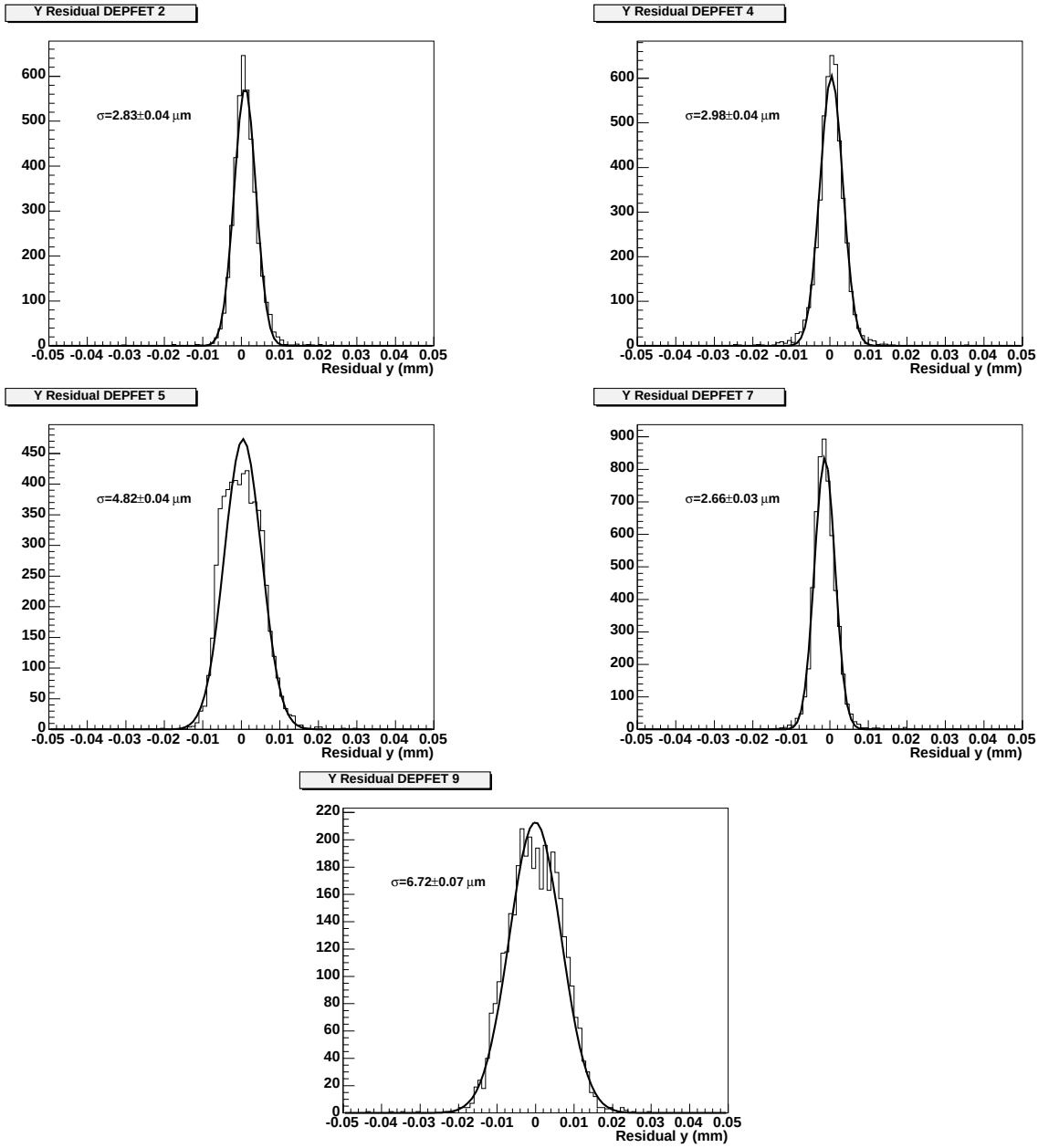

Figure 7.15: Residuals in the y direction of hits relative to y_o of the reconstructed track.

7.5.3 Alignment

Accurate determination of hit positions in one uniform coordinate system is necessary for the analysis of two-track resolution. Improved precision of hit coordinates is achieved with the alignment package written by Mathes [76]. One module in the package reads ACSII files containing the hit positions for each DEPFET module. Another program performs alignment and tracking by using the least χ^2 method. The program operates with 6 parameters about the translation and rotation for each DEPFET module given by the alignment procedure. Three of them are translations along the three axes and can be represented by a vector $\Delta\mathbf{X}(\delta x, \delta y, \delta z)$. Another three parameters are rotation angles (α, β, γ) around the x, y, z axes respectively. With these parameters, the position of a hit in the new coordinate system can be written as

$$\mathbf{X}_a = R_z(\gamma)R_y(\beta)R_x(\alpha)\mathbf{X}_o + \Delta\mathbf{X}, \tag{7.6}$$

where $\mathbf{X}_a$ is the aligned position vector, $\mathbf{X}_o$ is the position vector calculated from the cluster information only, and $R_{x,y,z}$ are rotation matrices.

7.6 Analysis on Two-track resolution

The two-track resolution can be studied when the tracks, noises of each pixel for all the DEPFET module and alignment parameters are available.

7.6.1 General procedure

As we have mentioned before, the analysis on the two-track resolution proceeds via merging of two tracks from different events into one, moving them closer and performing hit searching and track finding. The detailed procedure can be described as follows. At first, two tracks are selected. For each hit within these tracks, the row and column number of the cluster seed, the signals of pixels in the 3×3 cluster are readout. A DEPFET module is chosen as the reference plane. One track is kept unchanged. We use t_1 to indicate the track for simplification. Another track (t_2) is moved to the same row (column) in the reference plane as t_1 but with its x (y) coordinates unchanged by changing the row (column) number of cluster seeds by the same amount. An artificial event can be constructed from the cluster signals, seed positions of the two tracks and the noise of all pixels. Then we perform hit finding and tracking in this event to see whether two tracks can be reconstructed. The alignment parameters are used in tracking. After that, t_2 is moved towards t_1 pixel by pixel until the clusters of two tracks in the reference plane coincide with each other. In each step, the same hit finding and tracking procedures are performed. At last, we can get the relation between the fraction of events in which two tracks have been separated and the distribution between the two tracks. The two-track resolution can be obtained from this relation.

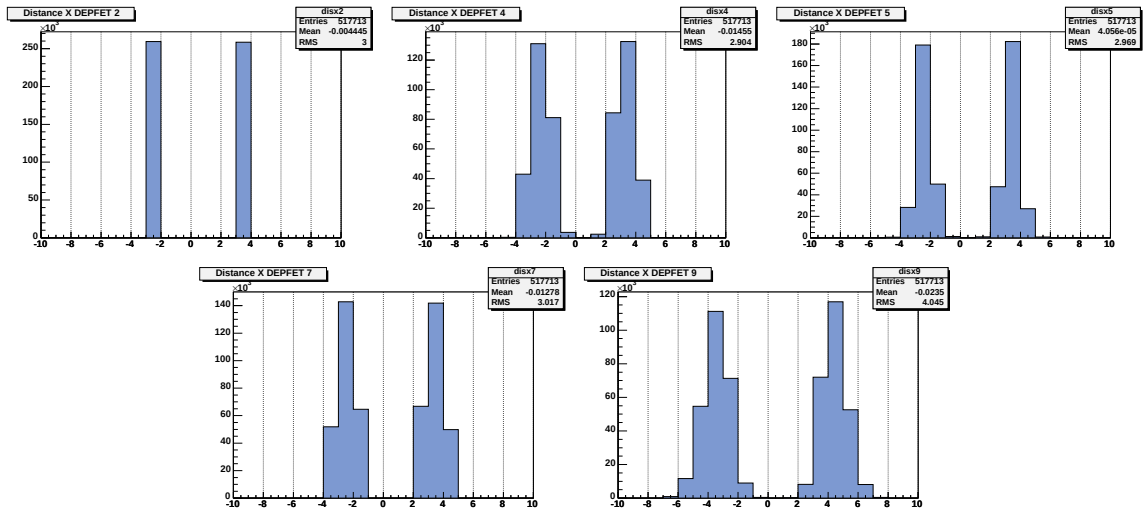

Figure 7.16: Distance between clusters in each DEPFET module when the distance of two tracks is set to 3 pixels in the reference plane in the x direction. The DEPFET module 2 is chosen to be the reference plane.

7.6.2 Influence of pixel geometry

In the analysis of two-track resolution, the distance of the two tracks is given by the distance between cluster seeds of the two tracks in the reference plane. The distance of cluster seeds in other DEPFET modules may not be the same as that in the reference plane, but the difference should be small.

The relative positions between the clusters of the moving track are required to be kept fixed while the track is moved pixel by pixel so that its shape would not change. The requirement is naturally fulfilled if all the pixels on different DEPFET modules have the same geometrical size. In the DEPFET telescope, the pixels in module 9 have different size to those in other modules. When all the clusters of a track move for the same amount of pixels, the actual distance of the cluster in DEPFET module 9 is different from others. Fig. 7.16 and Fig. 7.17 give the distance of the clusters of two different tracks in each DEPFET module expressed in the amount of pixels when the distance of the two tracks are set to be 3 pixels in x and y direction, which means the two clusters in the reference plane are next to each other. Clear differences have been found between the plots of DEPFET module 9 and other modules. Consequently, the hits in DEPFET module 9 have not been used in the analysis of two-track resolution.

7.6.3 Optimization of signal generation

The signal of other pixels outside the clusters can be given by an Gaussian-distributed random number generator whose standard deviation equals the noise of that pixel. As only pixels with a signal above the 2σ threshold are used in the calculation of hit positions, it is

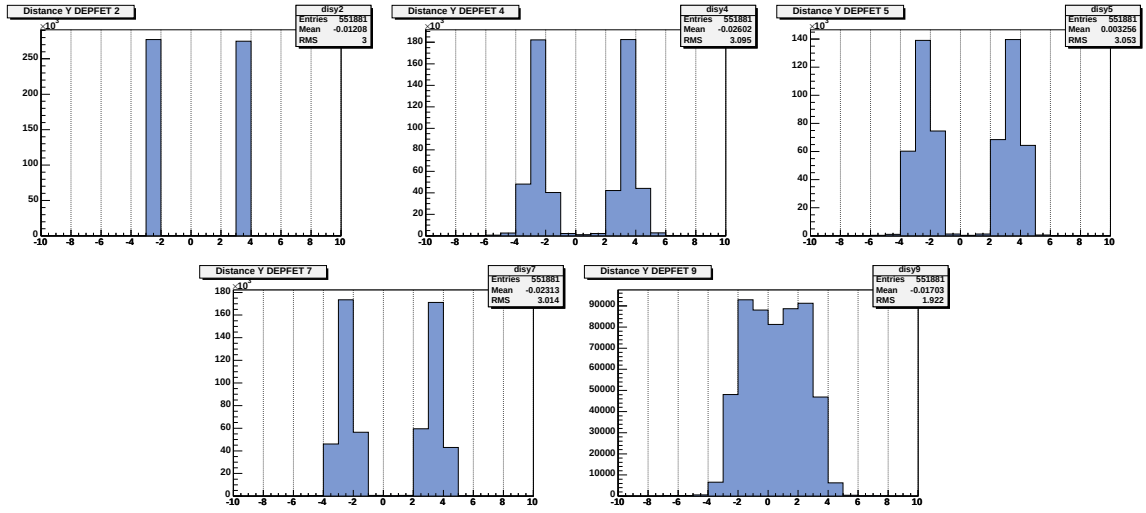

Figure 7.17: Distance between clusters in each DEPFET module when the distance of two tracks is set to 3 pixels in the reference plane in the y direction. The DEPFET module 2 is chosen to be the reference plane.

not necessary to generate signals for every pixel outside the clusters. Instead, the Gaussian-tail distribution is used for the generation of signals in $8192 \times 2.25\% \approx 185$ pixels in each DEPFET module. These pixels are selected randomly. Signals of other pixels are simply set to be 0.

7.6.4 Optimization of hit finding

One key problem of the analysis is whether two tracks can be separated when some of their clusters partly overlap with each other. By studying the properties of clusters, we found that the cluster positions can be calculated with the pixels in the 2×2 region in the cluster in half of cases. The number of each type of cluster and their fraction are plotted in Fig. 7.18. The type 1 cluster (small cluster) are those which positions can be calculated with pixels within the 2×2 area, and the type 2 cluster (large cluster) are those which positions should rather be calculated with pixels within the 3×3 area.

Fig. 7.19 shows the difference between positions calculated with the two different cluster size, 2×2 and 3×3. The differences between positions calculated in the two cases are below ~ 2 μm. Then a natural thought is to calculate the cluster positions with only the pixels with high signals in the 2×2 area around the seeds when two seeds are found to be close to each other so that the general 3×3 clusters partly overlap with each other. Using of smaller cluster enables the separation of close-by hits.

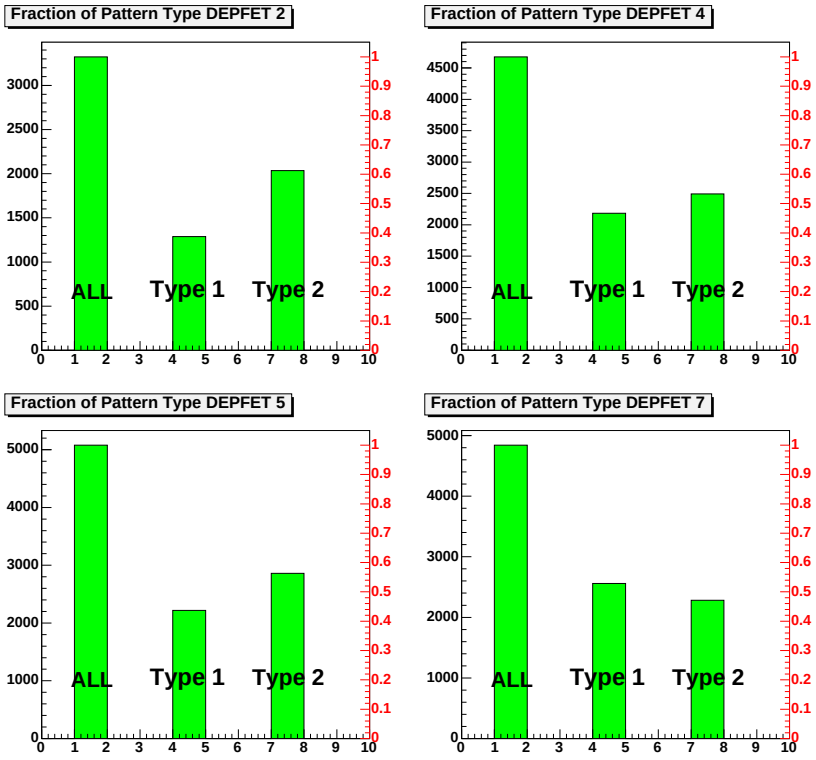

Figure 7.18: The fraction of the two different type of clusters.

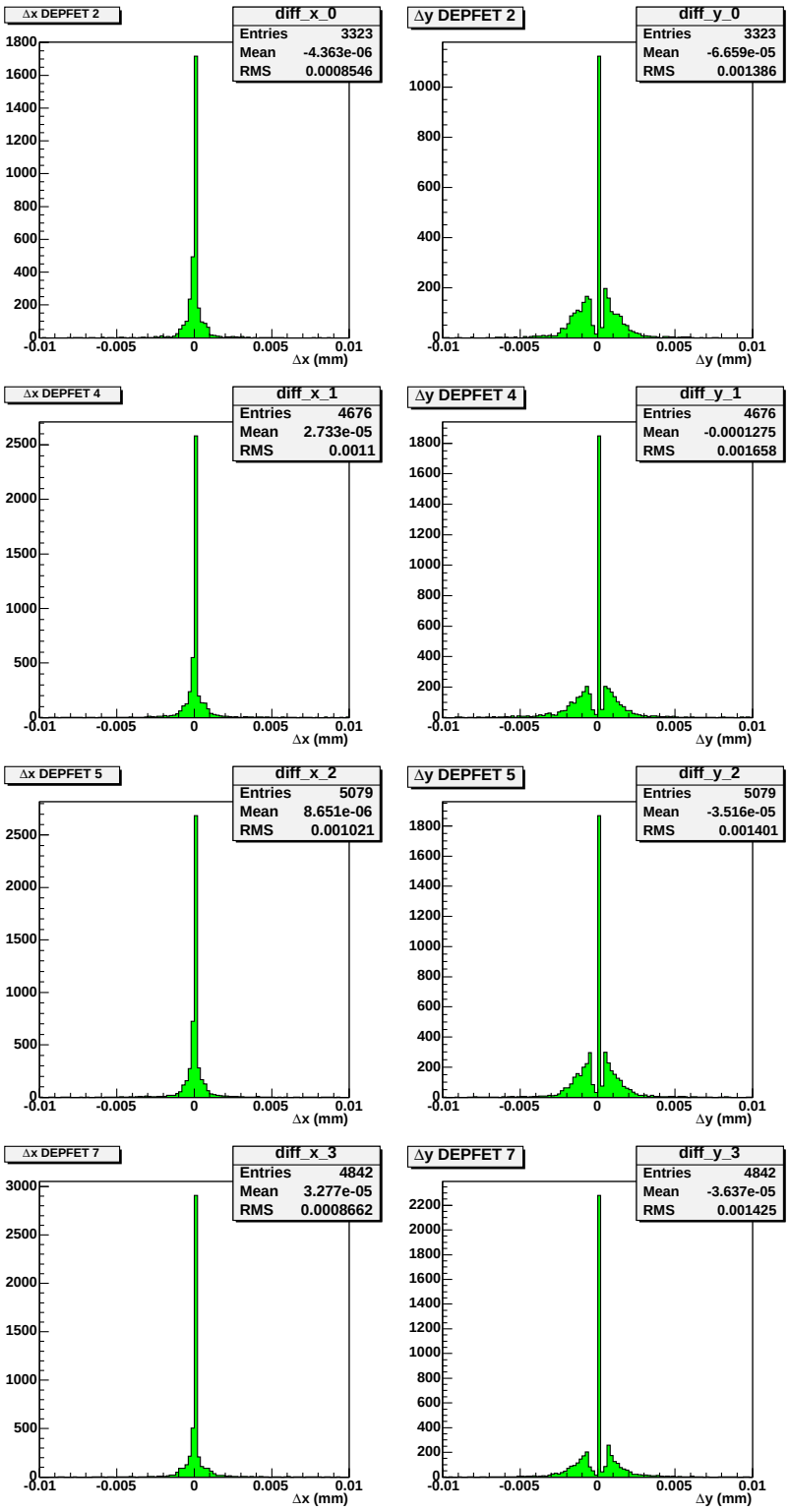

Figure 7.19: The difference between hit positions calculated with different cluster size.

7.6.5 Optimization of tracking

The tracking algorithm employed in the analysis of two-track resolution is a little different from the one used before. Only clusters in the four DEPFET modules are used, which means a track should contain at most 4 hits. Aligned hit positions, which are calculated from the reconstructed clusters and the alignment parameters, are used in tracking. The straight-line hypothesis of track is still used. The purpose of the tracking is to find out whether two tracks can be separated, irrespective of track parameters.

An important problem is the assignment of hit to tracks when two tracks are close to each other and the hit can be generated by either track. This is done by finding the distance of the hit to the two tracks. The hit is assigned to the track with smaller distance.

7.6.6 Results and discussions

The results of the analysis are plotted in Fig. 7.20 for the column (x-direction) and row (y-direction) of the DEPFET matrix, respectively. The number of events in which two tracks can be resolved, n_r, and the number of total events, n_t, are plotted as functions of the distance d_i between the tracks in blue and red lines respectively, where i is the number of pixels between the seeds of two tracks in the reference plane. When $i = 0$, the distance takes its minimum, i.e. 36 μm in column direction or 22 μm in row direction. The ratio

$$R(d_i) = \frac{n_r(d_i)}{n_t(d_i)}, \tag{7.7}$$

is given in asteroids. From the plots, we can find that $R(d_0) \approx 0$, $R(d_1) \approx 45\%$ and $R(d_i) \approx 100\%$ for $i \geq 2$. This implies that two tracks can be resolved effectively when their distance is larger than 3 times the pixel side length. The blue squares show the weighted cumulative fraction, which is defined as

$$R_{wc}(d_i) = \frac{\sum_k w_k n_r(d_k)}{i \cdot n_t(d_0)}, \ k < i, \tag{7.8}$$

where the weight w_k is given by $w_k = n_t(d_0)/n_t(d_k)$. It is the fraction of events in which two tracks can be solved in all the events when the distance of the two tracks is smaller than d_i.

While the pixel side lengths in the column and row directions are different, the two weighted cumulative fractions exhibit similar feature. Better two-track resolution is achieved in the row direction due to the smaller pixel side length. As a consequence, the two-track resolution of the DEPFET pixel telescope can be improved by decreasing the pixel size.

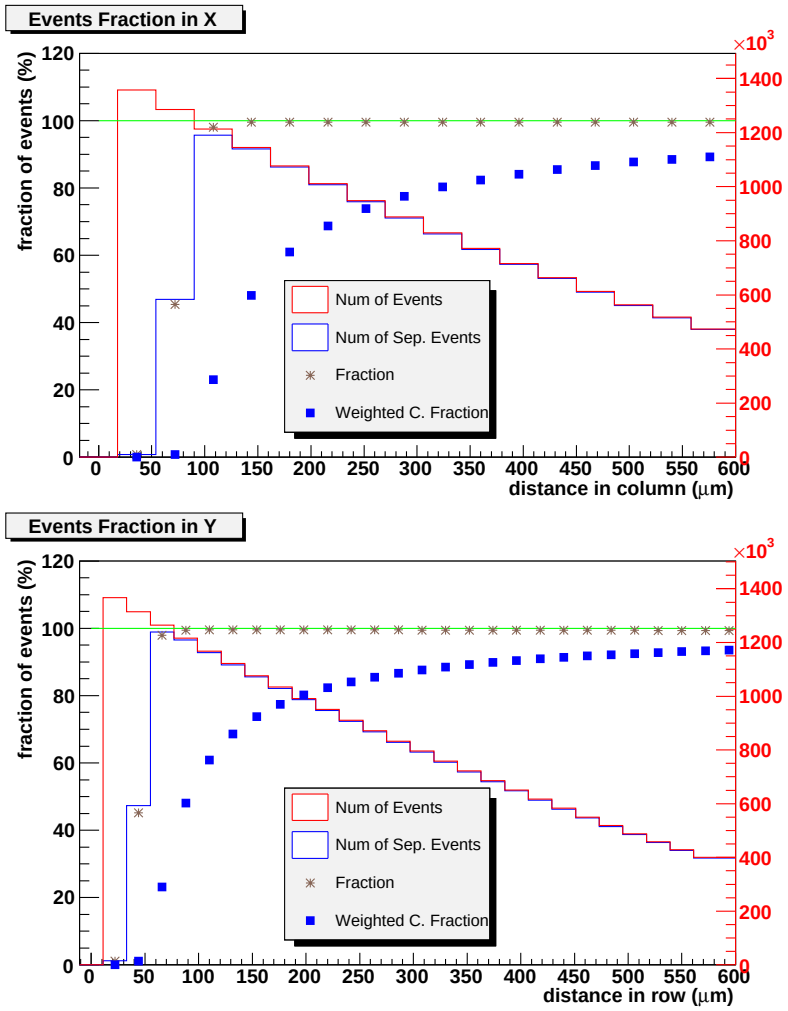

Figure 7.20: The results of two-track resolution analysis. The blue lines are the number of events where two tracks can be resolved, while the red lines are the number of all events. The ratio of the two numbers is plotted as asteroids. The blue squares are the weighted cumulative fractions, which is explained in the text.

Chapter 8

Production of right-handed smuon pairs

SUSY predicts the existence of a supersymmetric partner for each known particle that differs in spin by 1/2. For instance, smuons $\tilde{\mu}^{\pm}_{L,R}$ are the supersymmetric partners of muons. They can be produced in pairs at the ILC. In the mSUGRA SPS1a scenario, the dominant decay mode of smuons is $\tilde{\mu} \rightarrow \mu\tilde{\chi}^0_1$, where $\tilde{\chi}^0_1$, the lightest supersymmetric particle (LSP), is invisible in the ILC detector. Hence, muons with missing energy will be observed in this process. The masses of $\tilde{\mu}$ and $\tilde{\chi}^0_1$ can be obtained from the endpoint energies of muons. The ILC tracking system is essential for the precision measurement of muon momenta. The vertex detector, that improves the overall tracking performance, will play an important role.

Theoretical studies on the production of smuons and other sleptons at e^+e^- linear colliders have been performed in great detail [77], and some works based on fast simulation have given very good results [78, 79]. In this chapter, we will study the production of right-handed smuon pairs at the ILC in the mSUGRA SPS1a scenario, based on the full simulation and reconstruction chain with the tools currently available. By using a more realistic detector description, we will explore its potential.

8.1 Detection of right-handed smuons

The right-handed smuon $\tilde{\mu}^{\pm}_R$ can be produced at the ILC via s-channel γ/Z exchange,

$$e^+e^- \rightarrow \tilde{\mu}^+_R\tilde{\mu}^-_R. \tag{8.1}$$

The process is shown in Fig. 8.1. In the mSUGRA SPS1a scenario, the decay mode of the smuon directly into a muon and a lightest supersymmetric particle (LSP), $\tilde{\mu}_R \rightarrow \mu\tilde{\chi}^0_1$ is the dominant one. We expect to detect the two muons with missing energy resulting from the undetected $\tilde{\chi}^0_1$ in the process at the ILC.

Smuon decay is a simple two-body decay process. In the rest frame of the smuon, according

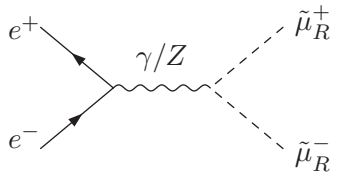

Figure 8.1: The production of $\tilde{\mu}_R^{\pm}$ pairs.

to the conservation of energy and momentum, we have

$$\mathbf{p}'_{\mu} + \mathbf{p}'_{\tilde{\chi}_1^0} = 0, \tag{8.2}$$

and

$$E'_{\tilde{\chi}_1^0} + E'_{\mu} = m_{\tilde{\mu}_R}, \tag{8.3}$$

where m is the mass of the particle, $\mathbf{p}$ is the momentum, and E is the energy. Substituting Eq. (8.2) into Eq. (8.3) and neglecting the muon rest mass, we obtain

$$m^2_{\tilde{\mu}_R} - 2m_{\tilde{\mu}_R}|\mathbf{p}'_{\mu}| = m^2_{\tilde{\chi}_1^0}, \tag{8.4}$$

or

$$E'_{\mu} = \frac{m_{\tilde{\mu}_R}}{2}(1 - \frac{m^2_{\tilde{\chi}_1^0}}{m^2_{\tilde{\mu}_R}}). \tag{8.5}$$

The energy of the muon in the laboratory frame can be solved by boosting back from the rest frame of the smuon,

$$E_{\mu} = \gamma E'_{\mu}(1 + v_{\tilde{\mu}_R}\cos\theta') = \frac{\sqrt{s}}{4}(1 - \frac{m^2_{\tilde{\chi}_1^0}}{m^2_{\tilde{\mu}_R}})(1 + \beta\cos\theta'), \tag{8.6}$$

where θ' is the angle between the smuon and the muon in the rest frame of smuon, $\beta = v_{\tilde{\mu}_R}$, and $\sqrt{s} = 2E_{\tilde{\mu}_R}$ is the center-of-mass energy by neglecting the effects of initial-state radiation (ISR) and beamstrahlung. The only variable in Eq. (8.6) is θ'. The angular distribution of muons should be isotropic in the rest frame of smuon. So the angle θ' has a probability density function of $p(\theta') = \frac{1}{2}\sin\theta'$, for $\theta' \in [0, \pi]$. We have

$$p(E_{\mu}) = p(\theta')\left|\frac{d\theta'}{dE}\right| = \text{constant}, \tag{8.7}$$

which means that the energy spectrum of muons is flat. The end points of the spectrum are given when the muon is parallel (anti-parallel) to the smuon, or $\cos\theta' = 1(-1)$. That leads to the relation between the end point energies and the masses of $\tilde{\mu}_R$ and $\tilde{\chi}_1^0$,

$$E_{\pm} = \frac{\sqrt{s}}{4}(1 - \frac{m^2_{\tilde{\chi}_1^0}}{m^2_{\tilde{\mu}_R}})(1 \pm \beta). \tag{8.8}$$

where the symbol "+" and "−" are used to indicate the upper and lower edge respectively. The masses of $\tilde{\mu}_R$ and $\tilde{\chi}_1^0$ can be calculated from the following equations:

$$m_{\tilde{\mu}_R} = \frac{\sqrt{s}}{E_- + E_+}\sqrt{E_- E_+}, \tag{8.9}$$

$$m_{\tilde{\chi}_1^0} = m_{\tilde{\mu}_R}\sqrt{1 - \frac{E_- + E_+}{\sqrt{s}/2}}. \tag{8.10}$$

Therefore, if we can measure the energy spectrum of muons from this process accurately, we can calculate the masses of $\tilde{\mu}_R$ and $\tilde{\chi}_1^0$ precisely. For a center-of-mass energy of 500 GeV, and polarization of e^-, e^+ beams of $P_{e^-} = 0.8, P_{e^+} = -0.6$ separately as proposed by the RDR of ILC [80], the cross section of $\tilde{\mu}_R$ pair production is around 135 fb in the SPS1a scenario, which yields enough events for analysis considering an integrated luminosity of 500 fb^{-1} which will be achieved in 4 years.

Backgrounds come from events in which two muons are detected together with missing energy. The most important backgrounds within the Standard Model are the production of W^+W^- pairs or Z^0Z^0 pairs with leptonic decay, $W^+ \to l^+\nu_l, W^- \to l^-\bar{\nu}_l, Z^0 \to \nu\bar{\nu}$ and $Z^0 \to l^+l^-$. At the same conditions mentioned before, the cross section of W^+W^- production with leptonic decay is around 80 fb and Z^0Z^0 production with leptonic decay is around 60 fb. SUSY events of the production of neutralino and chargino pairs, such as $e^+e^- \to \tilde{\chi}_1^0\tilde{\chi}_2^0$(20 fb) and $e^+e^- \to \tilde{\chi}_1^+\tilde{\chi}_1^-$(12 fb), also contribute to the background [1].

We are also interested in the angular distribution of the smuons. Because $\tilde{\mu}_R$ is a spin-0 particle, its angular distribution follows the relation [81]

$$\frac{d\sigma}{d\cos\theta} \propto \sin^2\theta. \tag{8.11}$$

When the masses of $\tilde{\mu}_R$ and $\tilde{\chi}_1^0$ are calculated, we can determine the direction of $\tilde{\mu}_R$ with twofold ambiguity. This will be discussed in detail in section 8.5.4.

8.2 Event generation

The study starts from the generation of Monte Carlo (MC) events. The PYTHIA [64] program is widely used in the event generation in many HEP experiments and is proven to be reliable. It can be used for the generation of both SM and SUSY events. But the SPS suggested using program ISAJET [82] as the standard event generator in the analysis of SUSY. ISAJET is a Monte Carlo program used for the simulation of $pp, \bar{p}p$, and e^+e^- interactions at high energies. The patch ISASUSY [83] of ISAJET can calculate decay modes of supersymmetric particles in the MSSM. A study shows that the output of PYTHIA and

[1] One possible source of backgrounds are events with two pions in which both pions are incorrectly identified as muons. As mentioned in chapter 5, studies shows that only 0.7% pions are identified as muons by the PFOID processor, which is used in our analysis for particle identification. Thus backgrounds from pions can be neglected.

ISAJET are in remarkable agreement with each other to within a few percent for the SPS1a scenario [84].

It is also possible to use PYTHIA and ISAJET together for the production of SUSY events, as PYTHIA provides an interface to call the routines of ISAJET. Such an event generator based on both PYTHIA 6.4 and ISAJET 7.75 is developed and used in our studies. Details are described in Appendix B.

We generated signal and background events for an integrated luminosity of $\mathcal{L} = 100$ fb^{-1} in the analysis, corresponding to the collection of data in one year. The center of mass energy is chosen to be 500 GeV. The beams are polarized to suppress the cross section of backgrounds (mostly W^+W^- pairs) with $\mathcal{P}_{e^-} = +0.8, \mathcal{P}_{e^+} = -0.6$. ISR is included by the default setting of PYTHIA . The synchrotron radiation resulting from the high density of electrons (positrons), or the so called beamstrahlung is included by using the CIRCE [85] program. By setting the parameters given in the SPS 1a scenario, the program gives $m_{\tilde{\mu}_R} = 142.52$ GeV and $m_{\tilde{\chi}_1^0} = 97.36$ GeV. Further more, a high statistics sample of signal MC events (900 fb^{-1}) is generated in order to study the shape of the spectrum.

The calibration procedure which relates the generated edges of the lepton spectrum to the reconstructed ones, requires simulation of signals with different masses of $\tilde{\mu}_R$. The events with different masses are generated by reading the SUSY mass spectrum from a SUSY Les Houches Accord (SLHA) file, not from the calculation of input parameters. It is discussed in detail in Appendix B. The output file of the event generator follows the HEPEVT standard [65], and can be used directly by the simulation program.

8.3 Simulation

Simulation is done with the Mokka program. Since each ILC detector is composed of a set of different sub detectors, the Mokka program defines detector models for the simulation of different detector concepts. In this study, the LDC00Sc and LDC01_05Sc models are used.

The LDC00Sc model follows the detector definition in the TESLA TDR. Many of its drivers simulate the realistic detectors in a simplified way without many details, so the model is just an rough approximation of the detector proposed by TESLA.

The LDC01_05Sc model follows the LDC baseline version 5. Compared with the LDC00Sc model, the main change is that the tracking system (especially the Time Projection Chamber (TPC)) has smaller radius, and extends in the direction of beamline. The whole detector is simulated of a more realistic level, and many new sub detectors, such as the Resistive Plate Chambers (RPCs) for muon detection, are added.

The detailed descriptions of the subdetectors of the two models are listed in Tab. 8.1 and Tab. 8.2. The simulation codes for the DEPFET vertex detector is not employed. But a general silicon vertex detector, which has the nearly the same structure and performance as the DEPFET one, is used. Similar results are expected by substituting the DEPFET vertex detector for the general one.

Name	C++ driver	Description
tube01	tube01	The conical beam tube made of Be and Fe with electronics.
vxd00	vxd00	Cylindrical implementation of the vertex detector with 5 Si layers, Be support structure, electronics end and cryostat. Inner radius is 15.5 mm, outer radius is 60 mm.
sit00	sit00	The SIT with 2 cylindrical Si layers at $r = 160, 300$ mm.
ftd00	ftd00	The FTD with 7 Si disks at z =200, 320, 440, 550, 800, 1050 mm in each side.
LumicalS00	Lumical	The strip LumiCal, initial version.
mask04	mask04	The tungsten cylindrical shielding mask.
STpc01	STpc01	The TPC, which inner radius is 320 mm, and outer radius is 1690 mm.
SEcal01	SEcal01	The electromagnetic calorimeter with tungsten as the absorber and thin silicon sensors. The inner radius of the barrel part is 1700 mm, and the outer radius is 1910 mm. The granularity is $1 \times 1\text{cm}^2$.
SHcal01	SHcal01	The hadron calorimeter with iron as the absorber and scintillator sensors. The inner radius of the barrel part is 1936 mm, and the outer radius is 2900 mm.
SCoil01	Scoil01	The coil is represented by an aluminum tube.
SYoke01	SYoke01	The iron-made returning yoke with polyhedra shape.
SFiled01	SField01	The magnetic field, 4 T along the beamline.

Table 8.1: The description of the subdetectors and drivers in the LDC00Sc detector model.

Name	C++ driver	Description
tubeX01	tubeX01	The beryllium beam pipe with cross angle proposed by LDC.
vxd01	vxd01	The vertex detector with realistic geometry proposed in the TESLA TDR.
sit01	sit01	The SIT with 2 cylindrical Si layer at $r = 160, 270$ mm.
SFtd02	Sftd01	The FTD with 7 Si disks at z =220, 350, 500, 850, 1200, 1550, 1900 mm in each side.
tpc08	tpc06	The TPC, which inner radius is 305 mm, and outer radius is 1580 mm.
SEcal02	SEcal02	The electromagnetic calorimeter made of Si/W. The inner radius of the barrel part is 1600 mm, and the outer radius is 1910 mm. The granularity is $3 \times 3\text{cm}^2$.
etd00	etd00	The endcap tracker detector, just as the FCH in the old TPC driver.
maskX01	maskX01	The more realistic shielding masks made of tungsten and graphite.
SHCal03	SHCal03	The hadron calorimeter made of iron and Scintillator. The inner radius of the barrel part is 1925 mm, and the outer radius is 2900 mm.
SCoil01	SCoil01	The coil is represented by an aluminum tube.
yoke03	yoke03	The iron-made returning yoke with RPC muon detector.
SLCal01	SLCal01	The more realistic implementation of the luminosity calorimeter.
SField01	SField01	The magnetic filed, 4 T along the beamline.

Table 8.2: The description of the subdetectors and drivers in the LDC01_05 model.

The parameters of the detectors are printed out into the GEAR xml file and can be used in reconstruction. The output file has the standard slcio format. Informations of MCParticle and hits generated in the detectors are recorded.

8.4 Reconstruction

Reconstruction is done within the software framework Marlin [59]. The Marlin framework allows to implement every computing task as a separate module, or the so called "processor" that analyzes and adds new data stream information to the persistency layer. The MarlinReco [62] package is a collection of processors developed for the digitization and reconstruction inside the ILC detector. It is used for the creation of tracker hits, reconstruction of tracks, clustering and Particle Flow Algorithm (PFA). The separate package, PandoraPFA [44], is the best PFA program currently available. It is used in the reconstruction of LDC01_05Sc model. The PFOID processor is employed for the identification of reconstructed particles via likelihood method. The DumpRecoParticle processor outputs the information of reconstructed particles, such as type, mass, momentum and energy, to a ROOT file for analysis.

We use two sets of processors for the reconstruction of simulation data in the two detector models. The processors used for the reconstruction of data in the LDC00Sc model are listed in Tab. 8.3, and for the data in the LDC01_05Sc model are listed in Tab. 8.4.

The MaterialDB processor is used to build the material database by reading detector geometries and properties from the GEAR xml file, which is produced by the Mokka program. The material database is important for the tracking procedures. The CurlKillerProcessor is used to enable effcient pattern recognition in TPC by removing high curling tracks, which deposit signal within a few neighboring TPC pads. The processors with suffix "Digi" are used to perform digitization of simulated hits in various subdetectors. Track segments are reconstructed in the silicon detectors by the SiliconTracking processor and in the TPC by the LEPTrackingProcessor separately. Then they are combined together into tracks by the FullLDCTracking processor. The TrackwiseClustering processor performs clustering of hits inside the calorimeter. The Wolf processor performs PFA to match clusters to tracks and reconstruct particles.

The main difference between the selection of processors for the two Models comes from the different choice of processor for PFA. The Wolf processor is used in the LDC00Sc model, while the PandoraPFAProcessor is used in the LDC01_05Sc model for both clustering and PFA. As the muon detectors are used in the LDC01_05Sc model, the SimpleMuonDigi processor is also used. In this analysis, the difference caused by the choice of PFA processors should be small because the relatively clean signal and the information of muons is mainly given by the tracking system. We plot the distribution of number of reconstructed muons in each event for data in the LDC01_05Sc model in Fig. 8.2. Both the Wolf processor and the PandoraPFA processor are used. The plot shows clearly that the difference caused by the different choice of PFA processors will be small.

Function	Processor
Miscs	MaterialDB
	CurlKillerProcessor
TrackDigi	TPCDigiProcessor
	VTXDigiProcessor
	FTDDigiProcessor
Tracking	SiliconTracking
	LEPTrackingProcessor
	FullLDCTracking
CaloDigi	MokkaCaloDigi
Clustering	TrackwiseClustering
PFA	Wolf
Identification	PFOID
Output	DumpRecoParticle

Table 8.3: The processors used for the reconstruction and particle identification in the LDC00Sc model.

Function	Processor
Miscs	MaterialDB
	CurlKillerProcessor
TrackDigi	TPCDigiProcessor
	VTXDigiProcessor
	FTDDigiProcessor
	SimpleMuonDigi
Tracking	SiliconTracking
	LEPTrackingProcessor
	FullLDCTracking
CaloDigi	MokkaCaloDigi
	SimpleLCalDigi
Clustering & PFA	PandoraPFAProcessor
Identification	PFOID
Output	DumpRecoParticle

Table 8.4: The processors used for the reconstruction and particle identification in the LDC01Sc model.

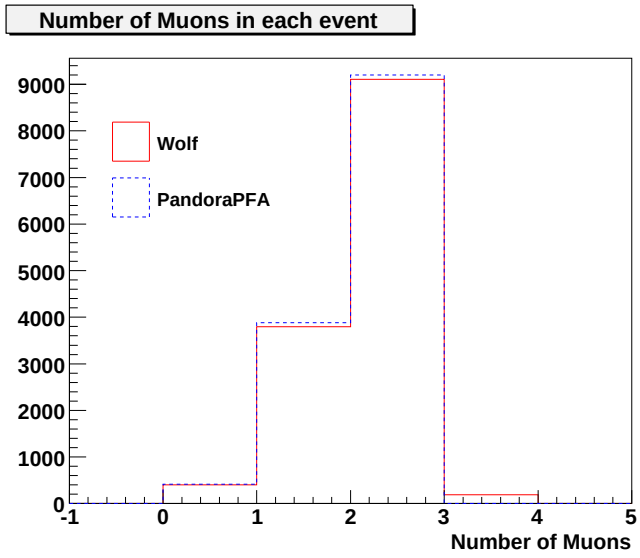

Figure 8.2: The distribution of the number of reconstructed muons in each signal event for data in the LDC01_05Sc model. Events are reconstructed with two PFA processors.

8.5 Analysis

After the reconstruction, we can plot the energy spectrum of the reconstructed muons. Fig. 8.3 shows the spectrum in the LDC00Sc model. The spectrum is nearly flat as predicted by theory. But the ISR, beamstrahlung and the detector resolution smear the edge of the spectrum. Muons from the background contribute about 20% to the whole spectrum, and complicate the determination of the endpoint energy. In order to clean the signal, cuts should be chosen carefully and applied to the data [77, 79].

8.5.1 Study of cuts

The study of cuts is based on data in the LDC00Sc model.

First of all, we require each event to contain only 2 muons, and a number of charged particles in each event not larger than 3, for there is the possibility that δ electrons may be produced inside the tracking system and be detected as separate tracks. Actually, only $\sim 1.5\%$ smuon events are found to have 3 charged particles. Soft muons with energies smaller than 2 GeV are rejected.

Because the two muons come from two different smuons in one event, we require the two muons to be acoplanar by the condition $\cos\alpha_{\mu\mu} < 0.998$, where $\alpha_{\mu\mu}$ is the angle between the two muons. The distributions of $\cos\alpha_{\mu\mu}$ are plotted in Fig. 8.4. The plots shows that the cut removes a small amount of the W^+W^- and Z^0Z^0 pair events.

Another cut concerns the direction of missing momentum. Missing momentum may resulted

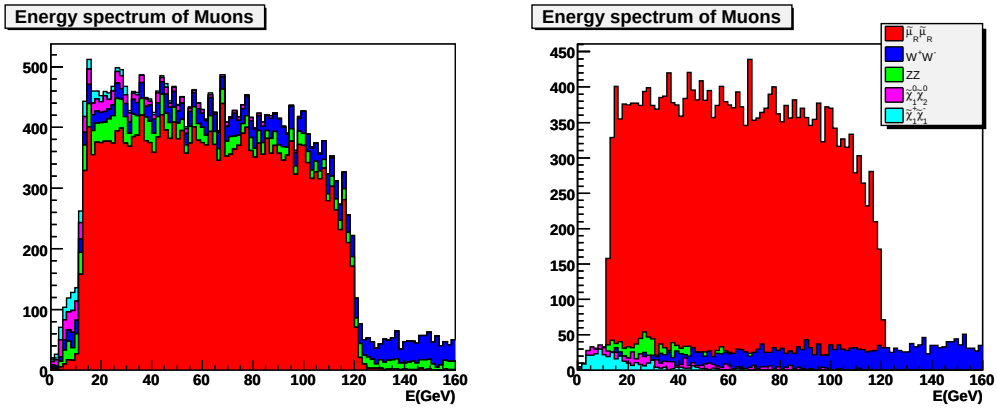

Figure 8.3: The energy spectrum of reconstructed muons before cuts of data in the LDC00Sc model, 100 fb^{-1}. The figure in the left is a stacked view, and the right one is a non-stacked view.

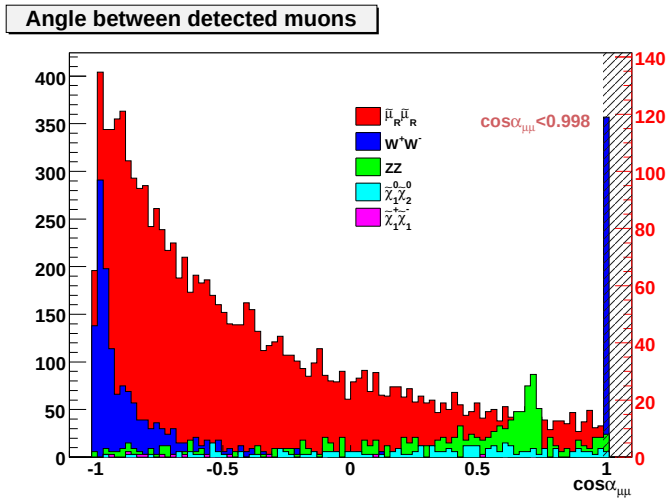

Figure 8.4: The distributions of angle between the two detected muons. The cut is $\cos\alpha_{\mu\mu} < 0.998$. The number of the background events is scaled and should be read from the axis on the right side.

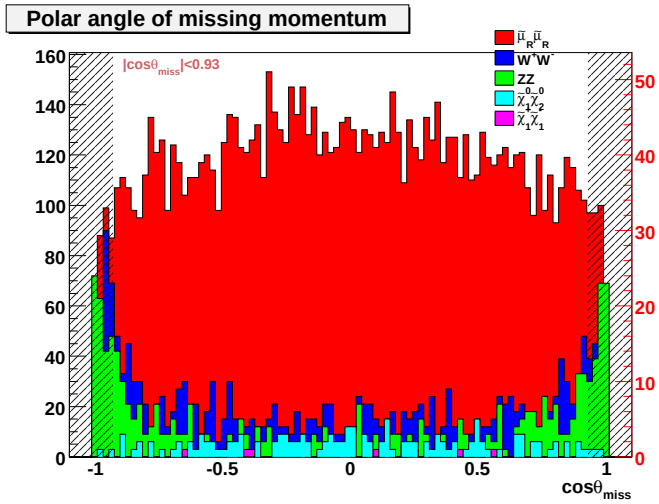

Figure 8.5: The distributions of the polar angle of the missing momentum. The cut is $|\cos\theta_{miss}| < 0.93$. The number of the background events is scaled and should be read from the axis on the right side.

from undetected particles inside the forward/backward region of the beampipe, so we should reject these events with $|\cos\theta_{miss}| < 0.93$, where θ_{miss} is the polar angle of the missing momentum. The distribution of θ_{miss} is plotted in Fig. 8.5. Backgrounds from SM are suppressed more than that from SUSY and the signal for their different distributions.

In the W^+W^- pair background events, missing energy is taken by neutrinos. The mass of the neutrinos is nearly zero, while the neutralino, which takes the missing energy in the smuon pair events, is very heavy. Hence, the missing energies of the W^+W^- pair background events can take very small value as opposed to signal events. The distributions of missing energy are plotted in Fig. 8.6. We can choose a cut of $E_{miss} > 220$ GeV. About half of the W^+W^- background events are dropped without affecting the signals. We also noticed that a peak appears around 250 GeV in the distribution of Z^0Z^0 events. It is just the energy of one single Z^0. But we do not set the cut here, for the peak is close to the distribution of signals. One thing should be emphasized that the distribution of the missing energy depends on the masses of $\tilde{\mu}_R$ and $\tilde{\chi}_1^0$ greatly. If we do not know the masses, we can not perform such a cut. Actually, we could estimate their masses from the energy spectrum of muons we obtained before. Then the missing energy of signals can be calculated in a rough level. That also explains why we set the cut far from the edge of the missing energy distribution of the signals.

The Z^0Z^0 pair events can be suppress by another way. Because the two muons come from one single Z^0, it is natural to cut on the recoil mass. The distributions of recoil mass are plotted in Fig. 8.7. The Z^0Z^0 pair events are suppressed greatly by requiring $m_{recoil} > 220$ GeV with very small impact on the signals. Similar to the cut on missing energy, this cut also requires a approximate knowledge of the masses of $\tilde{\mu}_R$ and $\tilde{\chi}_1^0$ from the energy spectrum of muons before cuts.

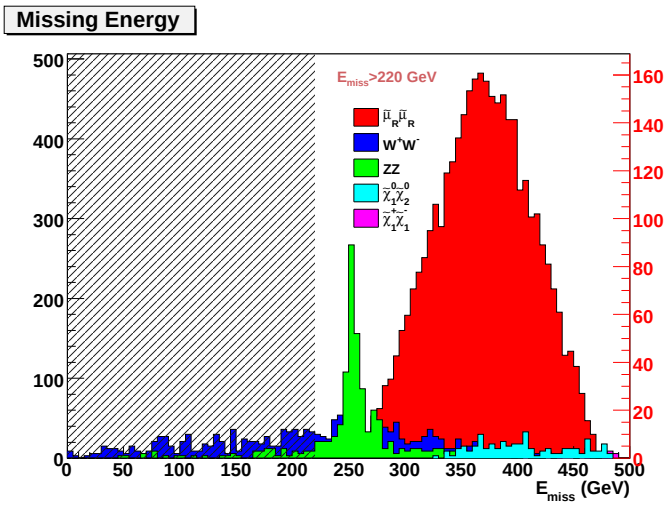

Figure 8.6: The distributions of the missing energy. The cut is $E_{miss} > 220$ GeV. The number of background events is scaled and should be read from the red axis.

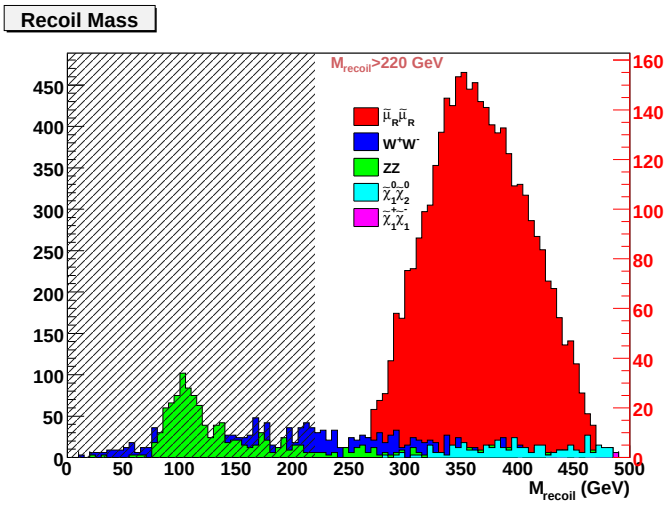

Figure 8.7: The distributions of the recoil mass. The cut is $m_{recoil} > 220$ GeV. The number of background events is scaled and should be read from the axis on the right side.

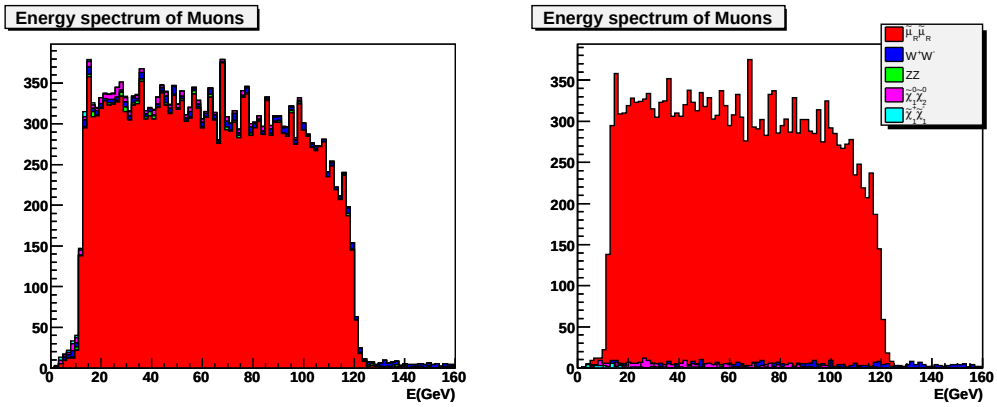

Figure 8.8: The energy spectrum of muons after cuts for data in the LDC00Sc model, 100 fb^{-1}. The figure in the left is a stacked view, and the right one is a non-stacked view.

LDC00Sc	$\tilde{\mu}_R\tilde{\mu}_R$	W^+W^-	Z^0Z^0	$\tilde{\chi}_1^0\tilde{\chi}_2^0$	$\tilde{\chi}_1^+\tilde{\chi}_1^-$
before cuts	24411	2712	2161	696	343
after cuts	20364	418	140	253	42

Table 8.5: The number of muons before and after cuts for data in the LDC00Sc model.

The energy spectrum of muons after applying all the cuts above is plotted in Fig. 8.8, and the numbers of muons before and after cuts are listed in Tab. 8.5. The selection cuts considerably suppress backgrounds while keeping high efficiency for signal. Only about 15% muons from signal are rejected, while about 85% muons from backgrounds are rejected. The selection increases the signal-to-noise (S/N) ratio from 4 to 24.

The same cuts are applied for the LDC01_05Sc model. The energy spectrum of muons before cuts is plotted in Fig. 8.9 and the spectrum after the cuts is plotted in Fig. 8.10. The numbers of muons before and after the cuts are listed in Tab. 8.6. Nearly 75% of signal events are retained, while about 85% of background events are rejected. The S/N ratio increases from around 4.5 to 25.

We notice a larger fraction of signal events is rejected in the LDC01_05Sc model than in the LDC00Sc model. The difference comes from the cut on the number of muons in each event, as shown in Fig. 8.11. In the LDC01_05Sc model, the amount of events in which only one

LDC01_05Sc	$\tilde{\mu}_R\tilde{\mu}_R$	W^+W^-	Z^0Z^0	$\tilde{\chi}_1^0\tilde{\chi}_2^0$	$\tilde{\chi}_1^+\tilde{\chi}_1^-$
before cuts	22292	2235	1837	559	282
after cuts	17283	353	135	175	28

Table 8.6: The number of muons before and after the cuts for data in the LDC01_05Sc model.

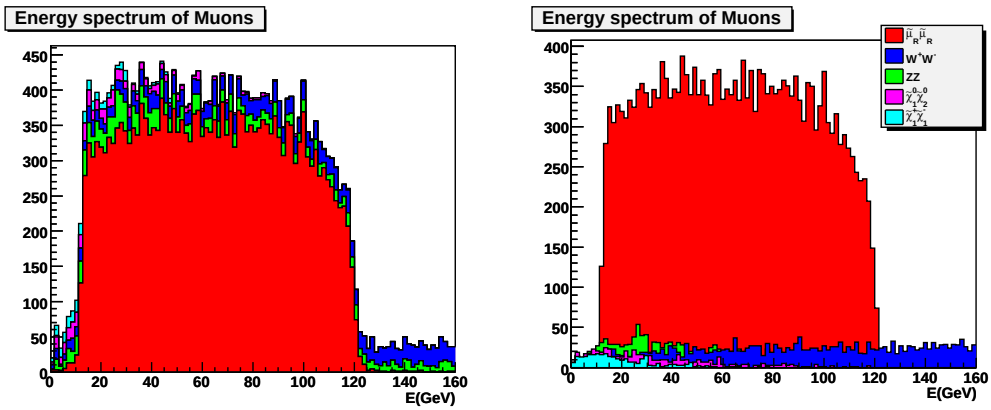

Figure 8.9: The energy spectrum of reconstructed muons before cuts of data in the LDC01_05Sc model, 100 fb^{-1}. The figure in the left is a stacked view, and the right one is a non-stacked view. The backgrounds make determination of edge of the spectrum difficult.

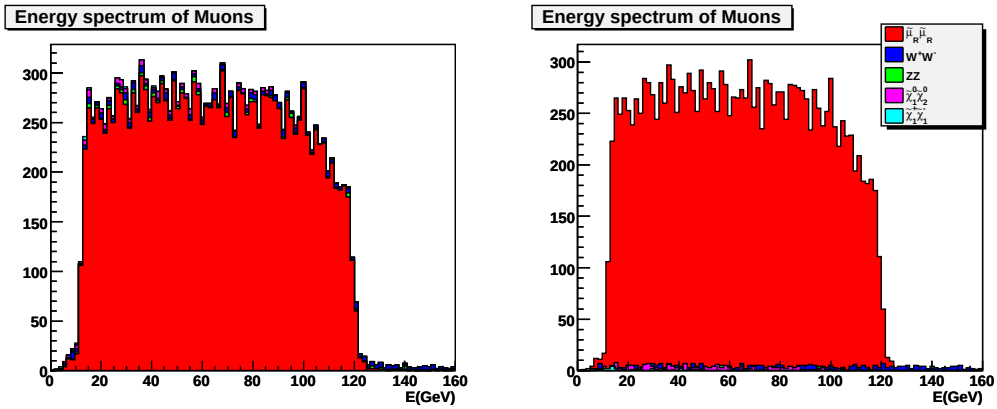

Figure 8.10: The energy spectrum of muons after cuts for data in the LDC01_05Sc model, 100 fb^{-1}. The figure in the left is a stacked view, and the right one is a non-stacked view. The backgrounds have been greatly suppressed.

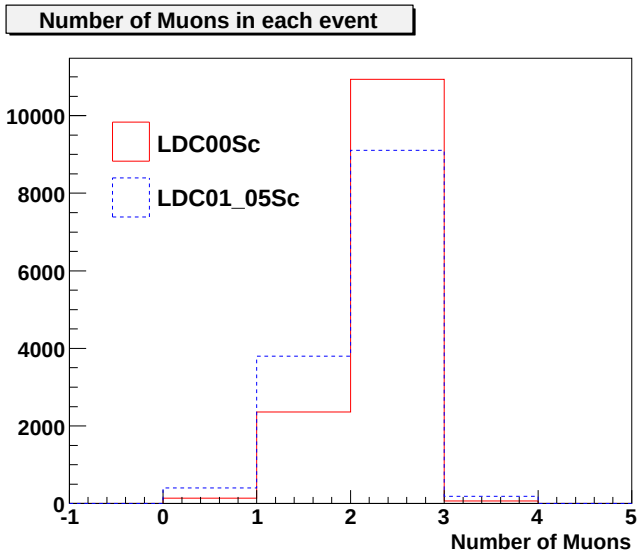

Figure 8.11: The distribution of number of reconstructed muons in each event in the two different detector model.

muon is reconstructed is larger than that in the LDC00Sc model, so more events are rejected.

8.5.2 Determination of masses

To access the information about $m_{\tilde{\mu}_R}$ and $m_{\tilde{\chi}_1^0}$, first the endpoint energy of the spectrum must be determined. The spectrum is not perfectly flat as the prediction of theory due to the existence of ISR, beamstrahlung and the resolution of the detectors. The ISR reduces the electron-positron collision energy, which moves both edges inwards. But the highest possible energy will not change. The beamstrahlung also changes the center-of-mass energy, either larger or smaller. The resolution of the detectors smears the edge and makes the edge oblique. Hence, we can not read the energies directly from the spectrum.

One way to determine the end point energies is choosing a function to fit the edge of the spectrum, and getting the end point energy from the intersection of the function and the x axis. We limit the range of the lower edge to be from 8 GeV to 28 GeV, and the upper edge to be from 80 GeV to 130 GeV. Each edge can be fitted with a function composed with 3 segments: a Fermi-Dirac distribution, a quadratic polynomial and a horizontal line. The detailed structure is given by Eq. (8.12) and Eq. (8.13). For the lower edge, we have

$$f(E) = \begin{cases} \dfrac{a_2}{1+\exp(\dfrac{a_0-E}{a_1})} + a_3, & E < E_1 \\ b(E-a_4)^2 + a_5, & E_1 \le E \le E_2 \\ a_5, & E_2 < E \end{cases} \tag{8.12}$$

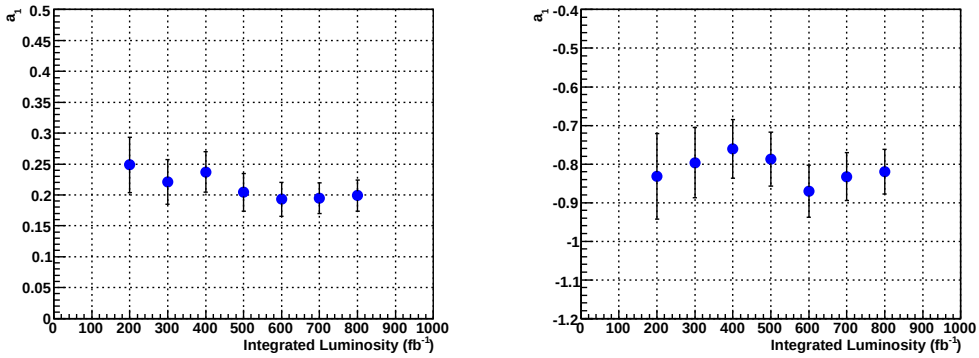

Figure 8.12: The effect of different integrated luminosities to the a_1 parameter in the LDC00Sc model. The left figure shows a_1 in the lower edge, and the right one shows a_1 in the upper edge.

and for the upper edge

$$f(E) = \begin{cases} a_5, & E_2 > E \\ b(E-a_4)^2 + a_5, & E_1 \geq E \geq E_2 \\ \dfrac{a_2}{1+\exp(\dfrac{a_0 - E}{a_1})} + a_3, & E > E_1. \end{cases} \tag{8.13}$$

where a_0, a_1, a_2, a_3, a_4 and a_5 are parameters to be determined in the fitting process, and E_1, E_2 and b can be calculated by the requirements of smoothness of these functions, for the function and its first order derivative should be continuous at these two points.

The end point energies are determined by the Fermi-Dirac distribution. The parameter a_0 gives the position of the distribution, and is related to $m_{\tilde{\mu}_R}$ and $m_{\tilde{\chi}_1^0}$. The parameter a_1 defines the width of distribution, and should be only related to the ISR, beamstrahlung and detector resolution. The changes of a_1 with respect to the integrated luminosity and the mass of $\tilde{\mu}_R$ in the LDC00Sc model are plotted in Fig. 8.12 and Fig. 8.13. The a_1 parameter does not change a lot for different integrated luminosity and different masses of smuons. So we can use a constant value of the a_1 parameter when performing the analysis. It is obtained by fitting the spectrum of MC data for an integrated luminosity of 900 fb^{-1} because a more accurate fitting result can be achieved with higher statistics.

The fitting functions in Eq. (8.12) and Eq. (8.13) are only valid for $\tilde{\mu}_R\tilde{\mu}_R$ signals. Though the backgrounds are greatly suppressed by the cuts, they can not be neglected in the analysis. Background subtraction is necessary in the analysis. This is done in the following way: Additional background events for an integrated luminosity of 200 fb^{-1} with the same conditions are generated. These events pass the same simulation and reconstruction steps. The cuts introduced before are applied to these events. Then we can obtain the lower and upper parts of the muon energy spectrum from the backgrounds. They are plotted in Fig. 8.14 and Fig. 8.15 for the two detector models separately. The spectra show large variances between

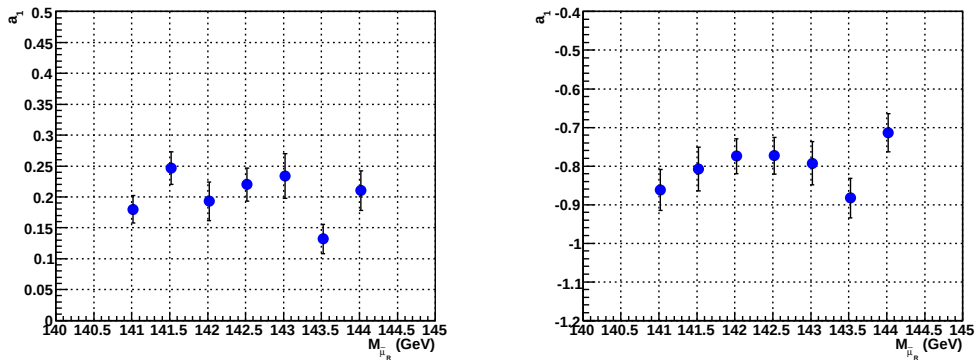

Figure 8.13: The effect of different $m_{\tilde{\mu}_R}$ to the a_1 parameter in the LDC00Sc model. The integrated luminosity is 900 fb^{-1}. The left figure show a_1 in the lower edge, and the right one shows a_1 in the upper edge.

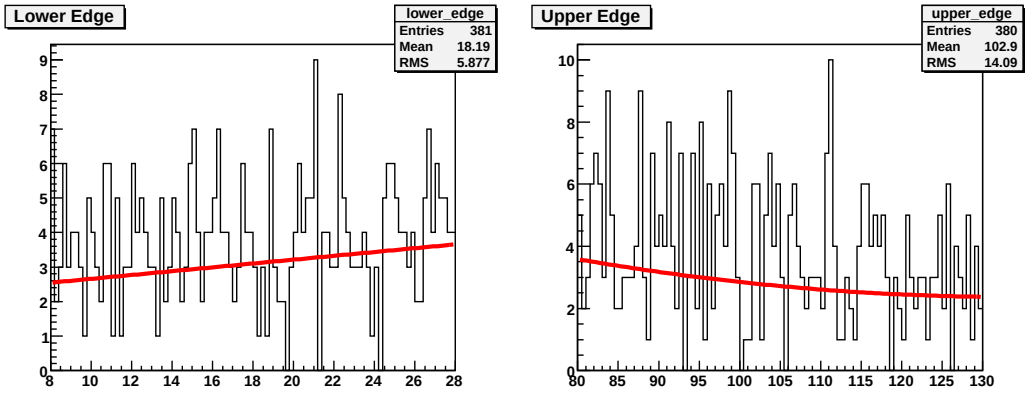

Figure 8.14: The energy spectrum of muons from background in LDC00Sc. The left figure shows the lower part of the spectrum, and the right one shows the upper part.

bins due to the low statistics after cuts. Decreasing the number of bins makes the spectrum smoother. The spectra can be fitted with quadratic polynomial functions. These functions will be scaled according to the integrated luminosity and be subtracted as backgrounds from the data to be analyzed.

The results of the background subtraction are plotted in Fig. 8.16 and Fig. 8.17 for the two detector models with different integrated luminosity. As a comparison, the energy spectrums from $\tilde{\mu}_R\tilde{\mu}_R$ signals are also plotted in these figures. It is clear that the subtraction method we employed is very effective.

Now we come back to the determination of the parameter a_1. As we have mentioned before, a_1 is obtained from the fitting from the high statistics data for an integrated luminosity of 900 fb^{-1} after the subtraction of backgrounds. The values are given in Tab. 8.7.

The values of a_1 parameter are fixed in the analysis of data for an integrated luminosity

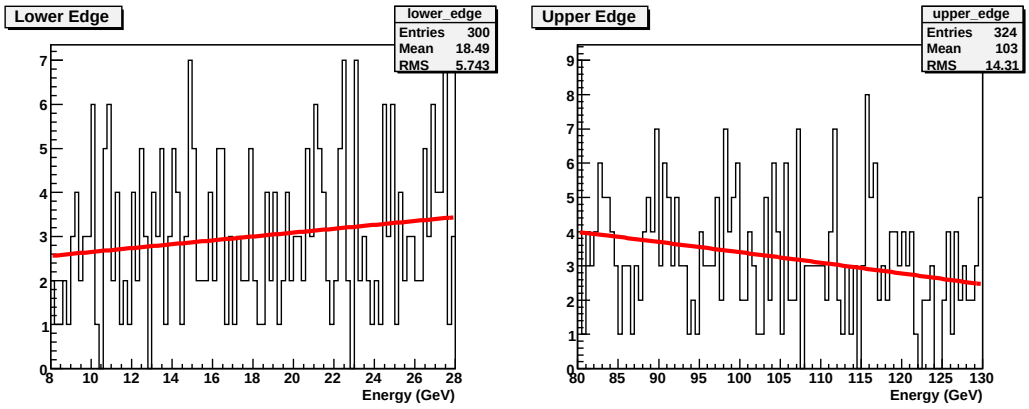

Figure 8.15: The energy spectrum of muons from background in LDC01_05Sc. The left figure shows the lower part of the spectrum, and the right one shows the upper part.

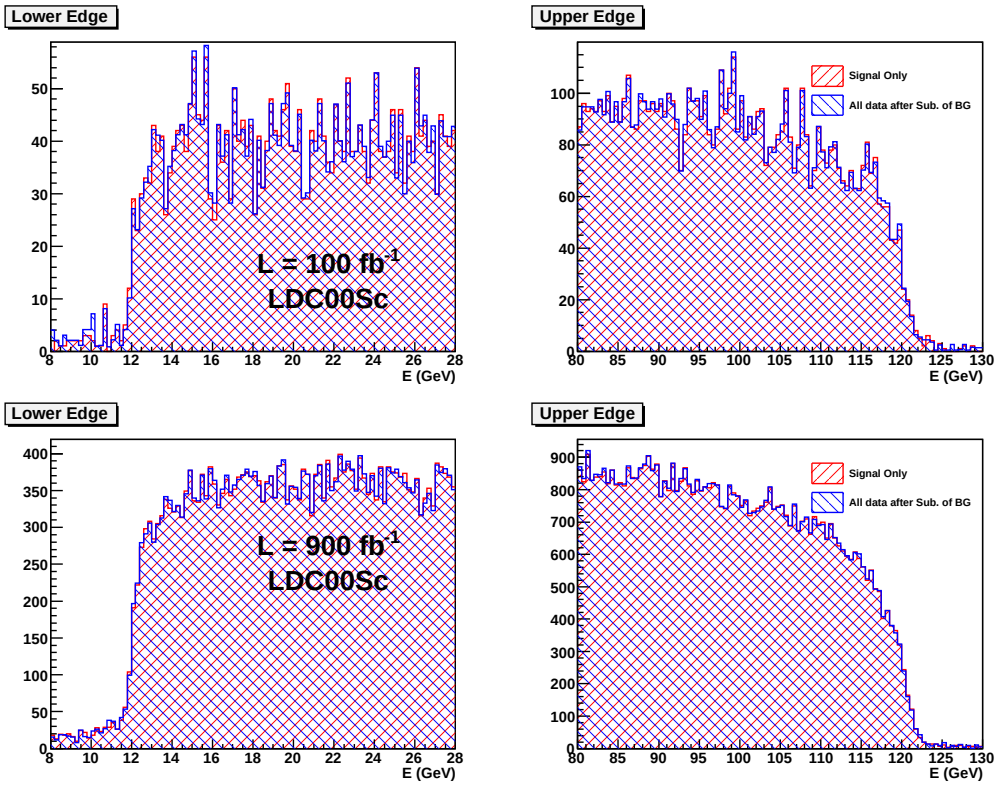

Figure 8.16: The muon energy spectrum after the subtraction of backgrounds in the LDC00Sc model for different integrated luminosity.

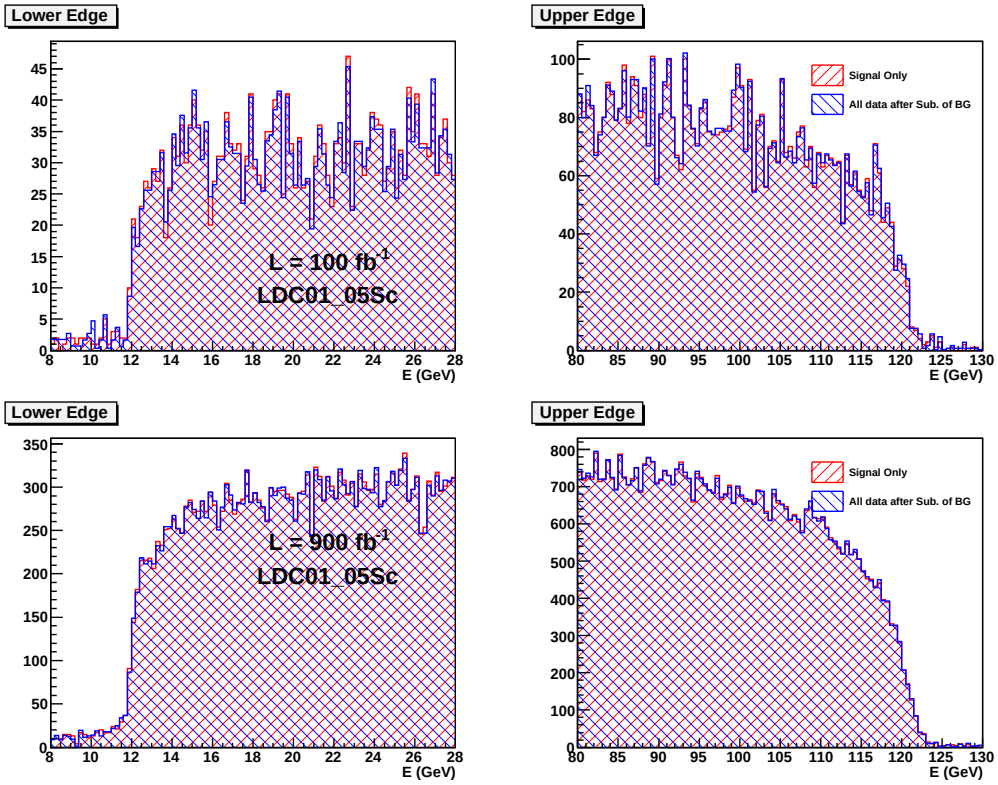

Figure 8.17: The muon energy spectrum after the subtraction of backgrounds in the LDC01Sc model for different integrated luminosity.

	LDC00Sc		LDC01_05Sc	
a_1	lower edge	upper edge	lower edge	upper edge
	0.222±0.024	-0.947±0.049	0.250±0.032	-0.877±0.043

Table 8.7: The values of the a_1 parameter from the fitting of data for an integrated luminosity of 900 fb^{-1} after backgrounds subtraction.

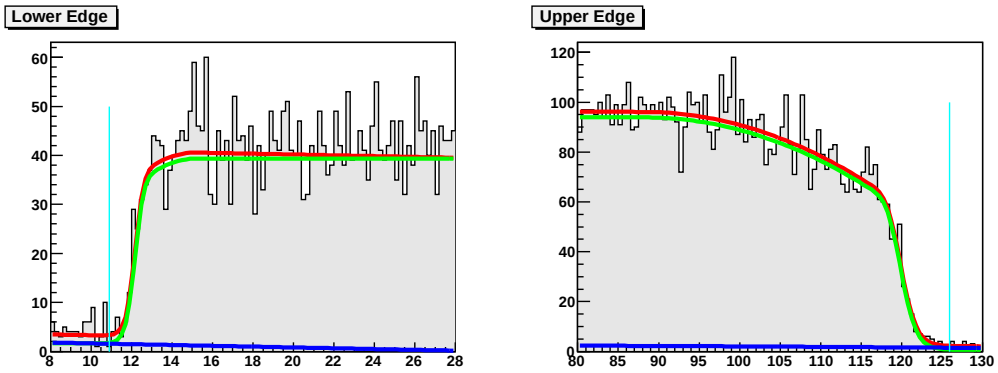

Figure 8.18: Fitting the edges of muon energy spectrum of data for an integrated luminosity of 100 fb^{-1} with the a_1 parameter fixed in the LDC00Sc model.

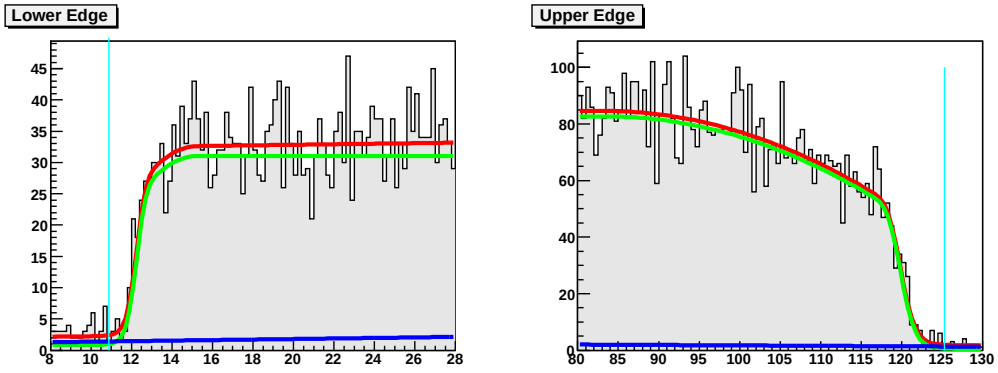

Figure 8.19: Fitting the edges of muon energy spectrum of data for an integrated luminosity of 100 fb^{-1} with the a_1 parameter fixed in the LDC01_05Sc model.

of 100 fb^{-1}. The fitting results are plotted in Fig. 8.18 and Fig. 8.19. The figures show the edges of muon energy spectrum from both signals and backgrounds. The dark (blue) lines indicate the backgrounds shapes. The light (green) lines are fitting functions for signals after background subtraction. And the red lines are the sums of background and signal distributions.

The Fermi-Dirac distribution parts in Eq. (8.12) and Eq. (8.13) have no intersections with the x axis. So we require that the endpoint energy E is given by

$$\frac{a_2}{1+\exp(\frac{a_0-E}{a_1})} = \epsilon, \tag{8.14}$$

where ϵ is a small value. We take $\epsilon = 1$ when the integrated luminosity is 900 fb^{-1}, which means the number of events should equal 1. For data of 100 fb^{-1}, the value of ϵ is scaled according to the integrated luminosity. With this requirement, we obtain $E_- = 10.91 \pm 0.15$ GeV, $E_+ = 125.89 \pm 0.35$ GeV in the LDC00Sc model and $E_- = 10.89 \pm 0.19$ GeV,

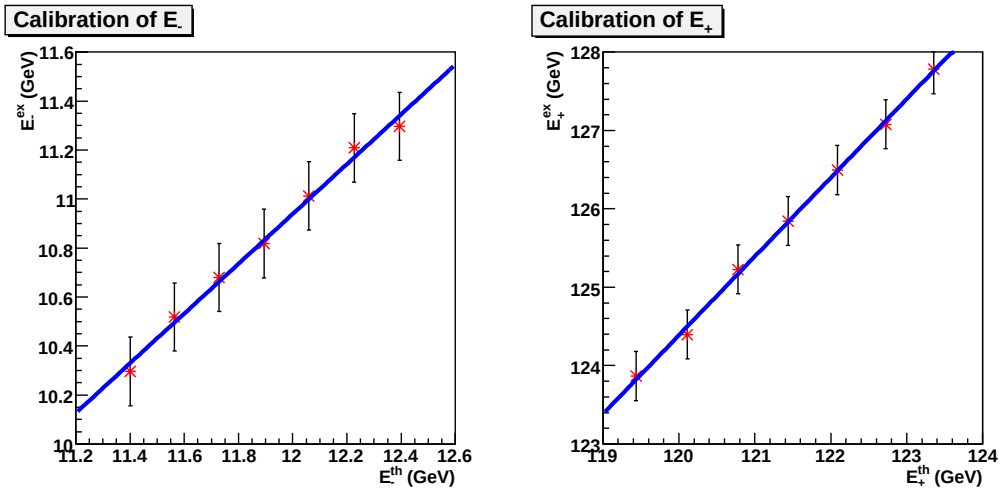

Figure 8.20: The fitting results of calibration for data in the LDC00Sc model.

$E_+ = 125.28 \pm 0.31$ GeV in the LDC01_05Sc model.

These end point energies can not be used directly in the calculation of masses, as the end points shifted due to the ISR, beamstrahlung and the resolution of detectors. Calibration is required. From Eq. (8.8), we can predict the end points when the masses of $\tilde{\mu}_R$ and $\tilde{\chi}_1^0$ are known. From the MC analysis of signal samples corresponding to different mass hypotheses, the relation between true and measured end points is established. The calibration lines are plotted in Fig. 8.20 and Fig. 8.21. Each point is based on the analysis of MC data for an integrated luminosity of 900 fb^{-1} with the mass of $\tilde{\mu}_R$ varied by 0.5 GeV and the a_1 parameter fixed.

After the calibration, the masses of $\tilde{\mu}_R$ and $\tilde{\chi}_1^0$ can be extracted. The results together with statistical errors are listed in Tab. 8.8. All of the calculated masses in both detector models are consistent with the input value, and the statistical error of masses is smaller than 1% with data for an integrated luminosity of 100 fb^{-1}. The larger statistical error obtained for the LDC01_05Sc model compared to LDC00Sc is explained by less efficient tracking system with the reduced radius of TPC. Compared to the previous analysis based on fast simulation [79], larger uncertainties of the endpoint energies are obtained, consequently leading to larger statistical errors.

8.5.3 Estimation of systematic errors

Two sources of systematic errors are considered at the current stage within the LDC01_05Sc model. One comes from the cut conditions. By varying the cut values in reasonable ranges, the final analysis result will change.

The first cut limits the number of muons and charged particles in each event. A stricter cut can be set to require only 2 charged particles in each event. The analysis with this cut

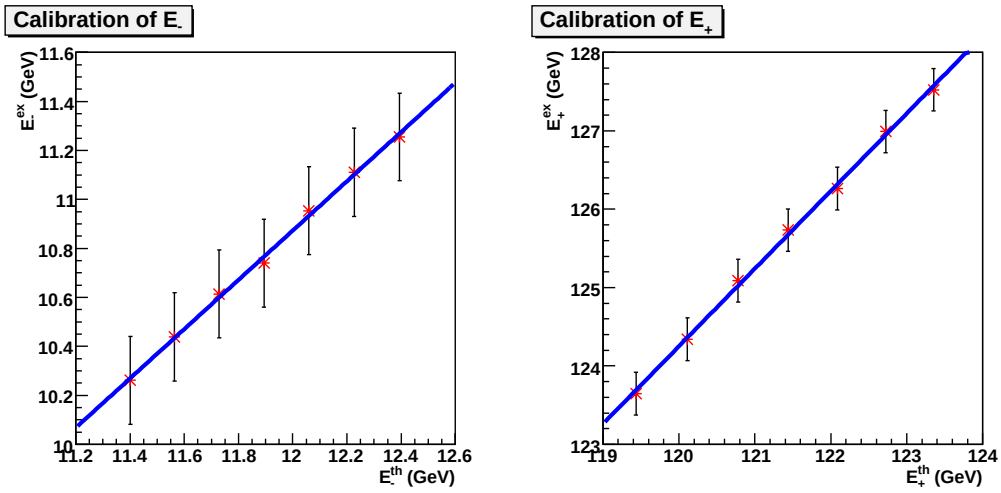

Figure 8.21: The fitting results of calibration for data in the LDC01_05Sc model.

Model	LDC00	LDC01_05Sc	Input
E_-	11.97 ± 0.15 GeV	12.02 ± 0.19 GeV	11.89 GeV
E_+	121.50 ± 0.35 GeV	121.04 ± 0.32 GeV	121.44 GeV
$m_{\tilde{\mu}_R}$	142.86 ± 0.76 GeV	143.33 ± 0.95 GeV	142.52 GeV
$m_{\tilde{\chi}_1^0}$	97.54 ± 0.51 GeV	98.03 ± 0.61 GeV	97.36 GeV

Table 8.8: The determined end point energies and masses of $\tilde{\mu}_R$ and $\tilde{\chi}_1^0$ and their true Monte Carlo values.

leads to a result of $\delta m_{\tilde{\mu}_R} = 0.40$ GeV and $\delta m_{\tilde{\chi}_1^0} = 0.38$ GeV.

The condition of the muons to be acoplanar can be modified. By taking the point resolution of the TPC at the ILC into account, this cut can be set as $\cos\alpha_{\mu\mu} < 1$. A result of $\delta m_{\tilde{\mu}_R} = 0.34$ GeV and $\delta m_{\tilde{\chi}_1^0} = 0.34$ GeV is obtained.

The cut on the direction of missing momentum is adjustable. Recognizing that the polar angle coverage of the vertex detector is $|\cos\theta| < 0.95$ for the inner layer and $|\cos\theta| < 0.9$ for the outer layer, the limitation on the direction of the missing momentum is set to be $|\cos\theta_{miss}| < 0.95$. Applying the new cut results in $\delta m_{\tilde{\mu}_R} = 0.23$ GeV and $\delta m_{\tilde{\chi}_1^0} = 0.21$ GeV.

Since the remaining two cuts on the missing energy and the recoil mass depend on the estimated values of $m_{\tilde{\mu}_R}$ and $m_{\tilde{\chi}_1^0}$, it is hard to determine the reasonable ranges of the two cuts. They are not considered at this time.

The momentum resolution of the ILC tracking system is another source of systematic error, because the energy of muon is given as the momentum measured by the tracking system. A momentum resolution of $\delta(1/p_t) \approx 5 \times 10^{-5}$ GeV^{-1} is required by the ILC. This value corresponds to $\delta p \sim 0.1$ GeV for a charged particle of 50 GeV. It can be treated as the systematic error from the tracking system.

By combining the above results, systematic errors of $\delta m_{\tilde{\mu}_R} = 0.58$ GeV and $\delta m_{\tilde{\chi}_1^0} = 0.56$ GeV are obtained. The values are comparable with the statistical errors. The total relative errors are slightly over the order of 1%.

8.5.4 Polar angle distribution of $\tilde{\mu}_R$

Once the masses of $\tilde{\mu}_R$ and $\tilde{\chi}_1^0$ are determined, we can study the polar angle distribution of smuons.

The key point is to extract the direction of $\tilde{\mu}_R$. We start from the decay process of a $\tilde{\mu}_R$ plotted in Fig. 8.22, in which α is the angle between the muon and the smuon, and β is the angle between the neutralino and the smuon. The momenta of the muons coming from the decay of smuons can be reconstructed. By applying momentum and energy conservation, we arrive at the following equations,

$$p_\mu \cos\alpha + p_{\tilde{\chi}_1^0} \cos\beta = p_{\tilde{\mu}_R}, \tag{8.15}$$

$$p_\mu \sin\alpha = p_{\tilde{\chi}_1^0} \sin\beta, \tag{8.16}$$

$$p_\mu + E_{\tilde{\chi}_1^0} = E_{\tilde{\mu}_R}, \tag{8.17}$$

$$p^2_{\tilde{\mu}_R} + m^2_{\tilde{\mu}_R} = E^2_{\tilde{\mu}_R}, \tag{8.18}$$

$$p^2_{\tilde{\chi}_1^0} + m^2_{\tilde{\chi}_1^0} = E^2_{\tilde{\chi}_1^0}, \tag{8.19}$$

where $p = |\mathbf{p}|$ is the absolute value of momentum, E is the energy of the particle. The equations can be solved because $p_\mu, m_{\tilde{\chi}_1^0}, m_{\tilde{\mu}_R}$ are known if we neglect the ISR and beamstrahlung.

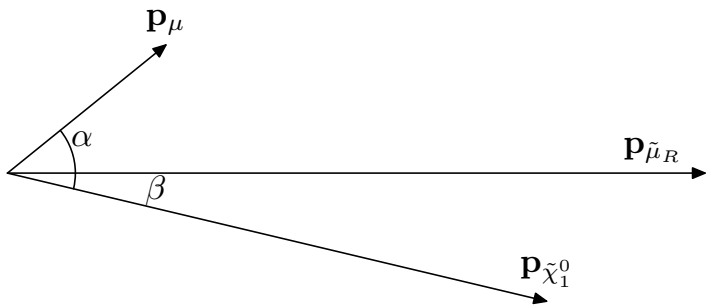

Figure 8.22: The decay of a smuon.

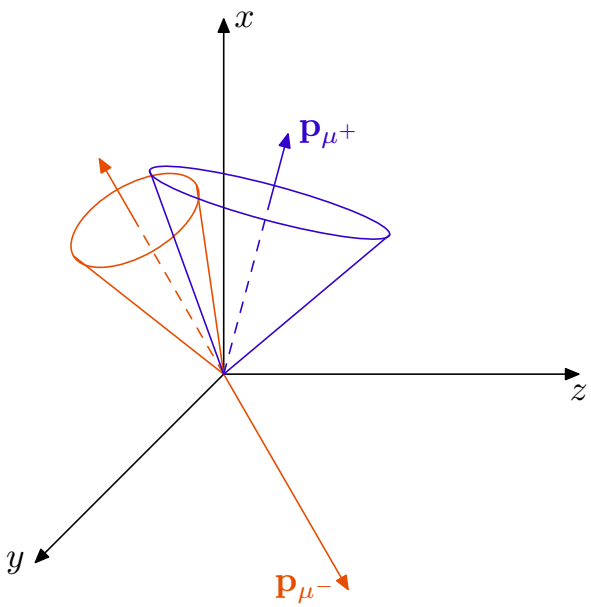

Figure 8.23: Using the intersections of two cones to determine the direction of the smuons.

We are only interested in α. The direction of the smuon lies on a cone whose axis is the direction of the muon with the apex angle equal 2α. Recognizing the production of smuons, the two smuons should go back-to-back if the initial total momentum is 0. For each smuon pair production event, we can get two cones. And if we flip one of the cones, we will get two intersection lines, just as plotted in Fig. 8.23. The solution of the intersection of two cones is discussed in detail in Appendix C. The smuon is parallel to one of the lines. But we can not distinguish the two solutions. Fortunately, the distribution of the false solution is different from that of the right one. So we can use the information from Monte Carlo simulation to find the distribution of the wrong solution and remove it from the final results. Fig. 8.24 shows the polar angle distribution of smuons with background and false solutions. The false solution is found out by comparing the two solutions with the smuon momentum extracted from the MC data in each event. Once the distribution of false solutions is obtained, it can be subtracted in the realistic data analysis by being normalized to the very edge of the twofold solution distribution, i.e. at ± 1 of $\cos\theta$.

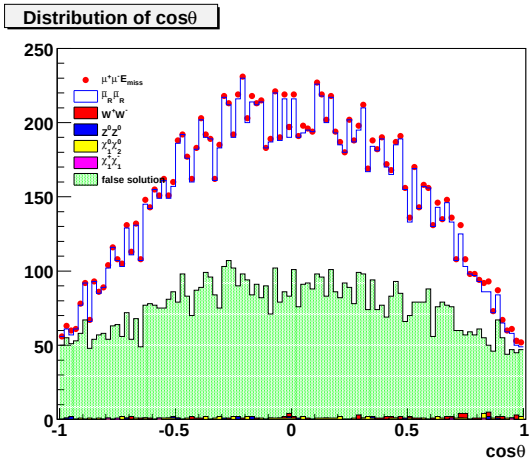

Figure 8.24: The polar angle distribution of the smuons with contribution from backgrounds and false solutions. The shadow part gives the distribution of false solution.

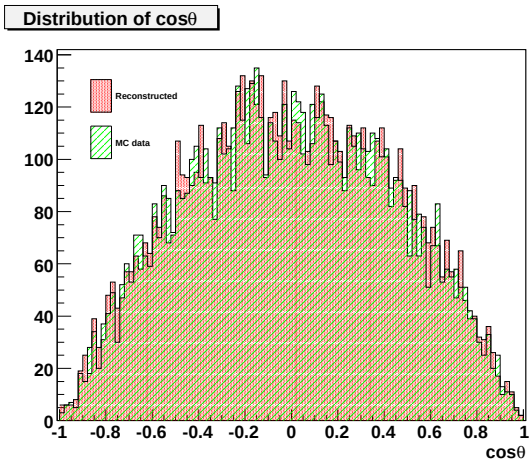

Figure 8.25: The distribution of the right solution and the polar angle distribution of $\tilde{\mu}_R^+$ from MC data.

The solution is tested by plotting the distribution of the "right" solution together with that from the MC data. It is shown in Fig. 8.25. The two distributions are compatible, and satisfy the distribution given by Eq. (8.11). The final angular distribution of $\tilde{\mu}_R$ follows a $\sin^2\theta$ dependence and indicates the scalar nature of the produced particle.

Chapter 9

Summary

DEPFET (DEPleted Field Effect Transistor) is one of the promising technologies for the vertex detector at the ILC due to its excellent signal-to-noise ratio, good radiation tolerance and many other features. In this thesis, we discussed the detailed simulation of the DEPFET vertex detector at the ILC and studied the impact parameter resolution with the simulation codes. We also analyzed test beam data for the two-track resolution of a DEPFET prototype telescope. The production of SUSY smuons at the ILC is studied with full simulation and reconstruction.

The detailed simulations of the DEPFET based vertex detector in two ILC detector concepts are implemented as drivers within the framework of Mokka, which is a Geant4-based full simulation program. In the LDC concept, the vertex detector has a five-layer barrel structure composed of ladders. The corresponding driver provides realistic and detailed description of the DEPFET sensors, support frames and steering chips of the ladders. The ladders are rotated and translated to their proper positions to form the barrel. Since no mechanical detailed concept for the support system of the vertex detector exists, a simplified description to the outer support shells is implemented. The parameters used to describe the detector geometry are stored in MySQL database and read on-the-fly when running Mokka. The detector geometry can be changed easily by modifying the content of the database so that the performance of the device can be evaluated for different design. In the SiD concept, a barrel vertex detector with endcap disks is proposed. The barrel part has similar structure to that in LDC. Thus a detailed description of the barrel part is implemented. For the endcap disks, only the sensors are implemented. A detailed implementation of the beam pipe following the SiD outline is also given. The driver for the DEPFET vertex detector in LDC is employed in the study of the impact parameter resolution. For sensors with a thickness of 50 μm and a pixel size of 25×25 μm^2, the DEPFET vertex detector does well meet the ILC requirement on the impact parameter resolution of

$$\sigma(IP_{r\phi}) = 5 \oplus \frac{10}{p \cdot \sin^{3/2}\theta}. \tag{9.1}$$

A DEPFET telescope consisting of 5 DEPFET modules was set up for the first time in

the beam test at CERN in 2006 with pions of 180 GeV. Analysis of the test beam data started from the extraction of the raw signals of each pixel. Pedestal and noise in each pixel are calculated by the decomposition of the raw signal. Common mode noise is calculated and removed while reading out. Seeds are searched in all the DEPFET modules in each event. Hot pixels are removed by inspecting the frequency of each pixel being recognized as a seed. A seed together with its neighbor pixels, called a cluster, are used to calculate the hit position. Correlations between the positions of hits on different DEPFET modules in each event are studied. With the correlations, hits on different DEPFET modules are projected to one DEPFET module. Thus tracks can be reconstructed using a rough model. A strict alignment was performed with the reconstructed tracks and alignment parameters were obtained. The analysis on the two-track resolution is performed by merging tracks from different events into one, move them closer and perform hit searching and track finding. One of the DEPFET module is not used in the final analysis due to its different geometrical size of pixels. Hit finding efficiency is optimized by using smaller clusters after the study of cluster shapes. The alignment parameters are used in the tracking procedure. The analysis results shows that two tracks can be separated in about 45% of the events in which there is only one pixel between the seeds of two tracks in DEPFET module 2 in either direction. That means the smallest possible distance of two tracks is twice the length of the pixel in either direction. The analysis provides important information for the development of reconstruction programs.

In the study of smuon production, a PYTHIA based event generator with ISAJET support is used for the generation of signal and backgrounds from SUSY and the Standard Model. Full simulation is done by using the Mokka program with two detector models for the TESLA and LDC concepts separately. Tracking is the key in the reconstruction because it provides the momentum information of the charged particle. To suppress the backgrounds, several cuts are selected and applied. The S/N ratio increases by a factor of 6 after the cuts. The masses of $\tilde{\mu}_R$ and $\tilde{\chi}_1^0$ can be calculated with the end point energies of the flat energy spectrum of the reconstructed muons. Two functions, each composed of three segments, are used to fit the lower and upper edges of the muon energy spectrum. Some parameters of the functions are fixed by fitting the high statistic MC data after background subtraction. Calibration is done through the analysis of MC data with different values of $m_{\tilde{\mu}_R}$. The calculated $m_{\tilde{\mu}_R}$ and $m_{\tilde{\chi}_1^0}$ are consistent with the input value. Systematic errors stemming from cuts and tracking system are estimated. The total relative errors are slightly above 1%. The calculated masses are used in the study of $\tilde{\mu}_R$'s polar angle distribution. After removing the false solution with the help of MC data, the $\sin^2\theta$ dependence property of the distribution indicates the scalar nature of $\tilde{\mu}_R$.

Appendix A

The geometry of DEPFET ladders

In this Appendix, we summarize the parameters used in the simulation of DEPFET ladders.

A ladder is treated as the combination of four components – the sensor, the steering chips, the upper support frame and the lower support frame. The sensor and steering chips are implemented as boxes. For each of them, three parameters are used to define the length, width and thickness. Compared to the sensor and steering chips, the two support frames are more complex. The schematic views of the support frames are illustrated in Fig. A.1 and Fig. A.2. Both frames can be treated as boxes with large etching hole(s). Besides the parameters related to the box, additional parameters are used to specify the length, width and positions of etching hole(s).

The parameters are listed in Tab. A.1. Some parameters are shared by several components. The two support frames have same length and width. The upper support frame has the same thickness as that of the sensor. The etching hole in the upper support frame and the sensor share the same geometrical parameters.

With the parameters, the offset of a ladder, d_o[1] can be written as

$$d_o = l_{\frac{1}{2}s} + 2(l_{\frac{1}{2}f} - l_{\frac{1}{2}s} - y_{\frac{1}{2}}) + \frac{t_2 - R + \Delta + (R + t_1)\cos\frac{2\pi}{n}}{\sin\frac{2\pi}{n}}, \tag{A.1}$$

where n is the number of ladders in this layer, t_2 is the distance from the sensor center to the bottom of the support frame, R is the distance from the original point to the sensor plane, Δ is the distance between the edge and the surface of two adjacent ladders, t_1, $l_{\frac{1}{2}s}$, $l_{\frac{1}{2}f}$ and $y_{\frac{1}{2}}$ are used to represent "sensor_half_thickness", "sensor_size_half_y", "frame_size_half_y" and "frame_chipside_half_y", respectively.

[1] See section 6.2.3 in chapter 6.

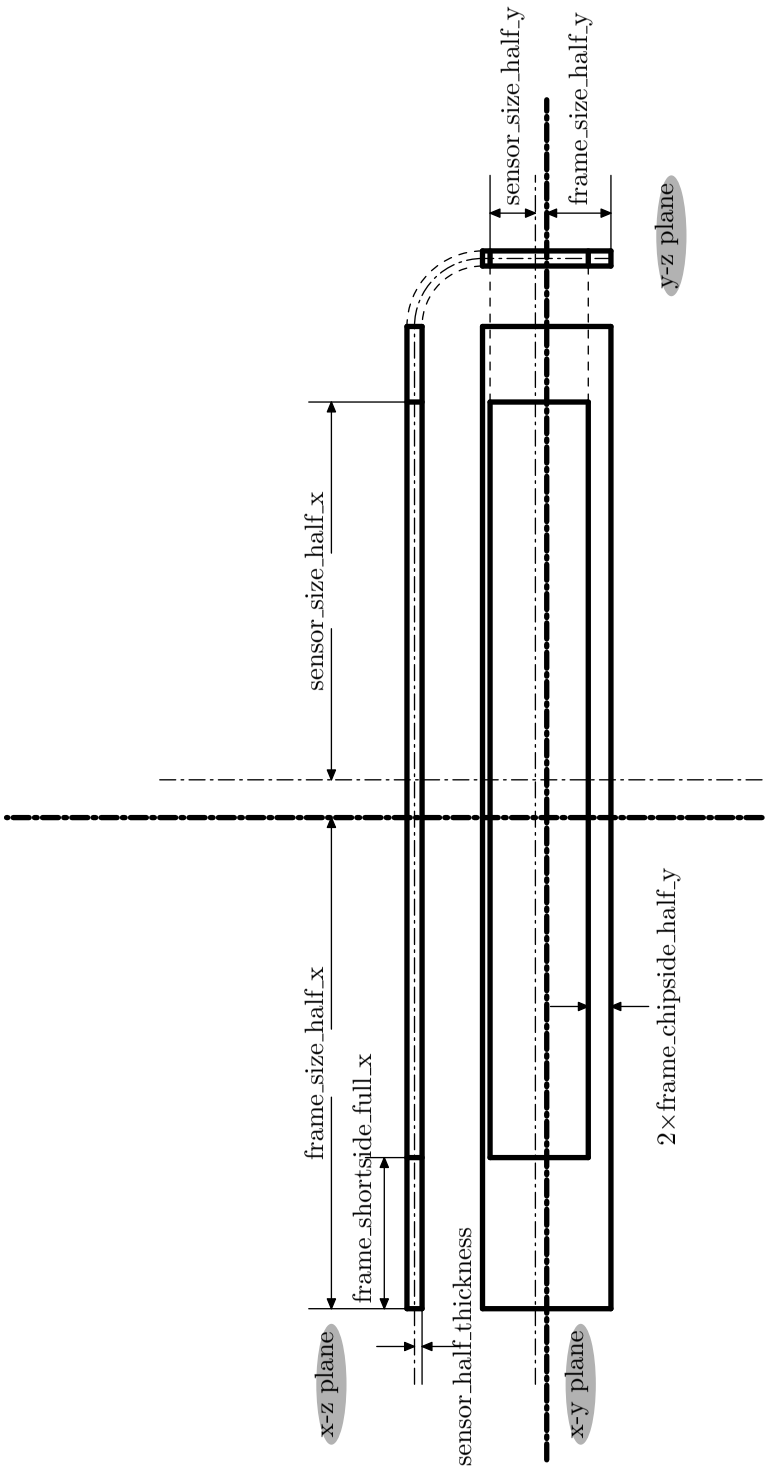

Figure A.1: The schematic view of the upper support frame.

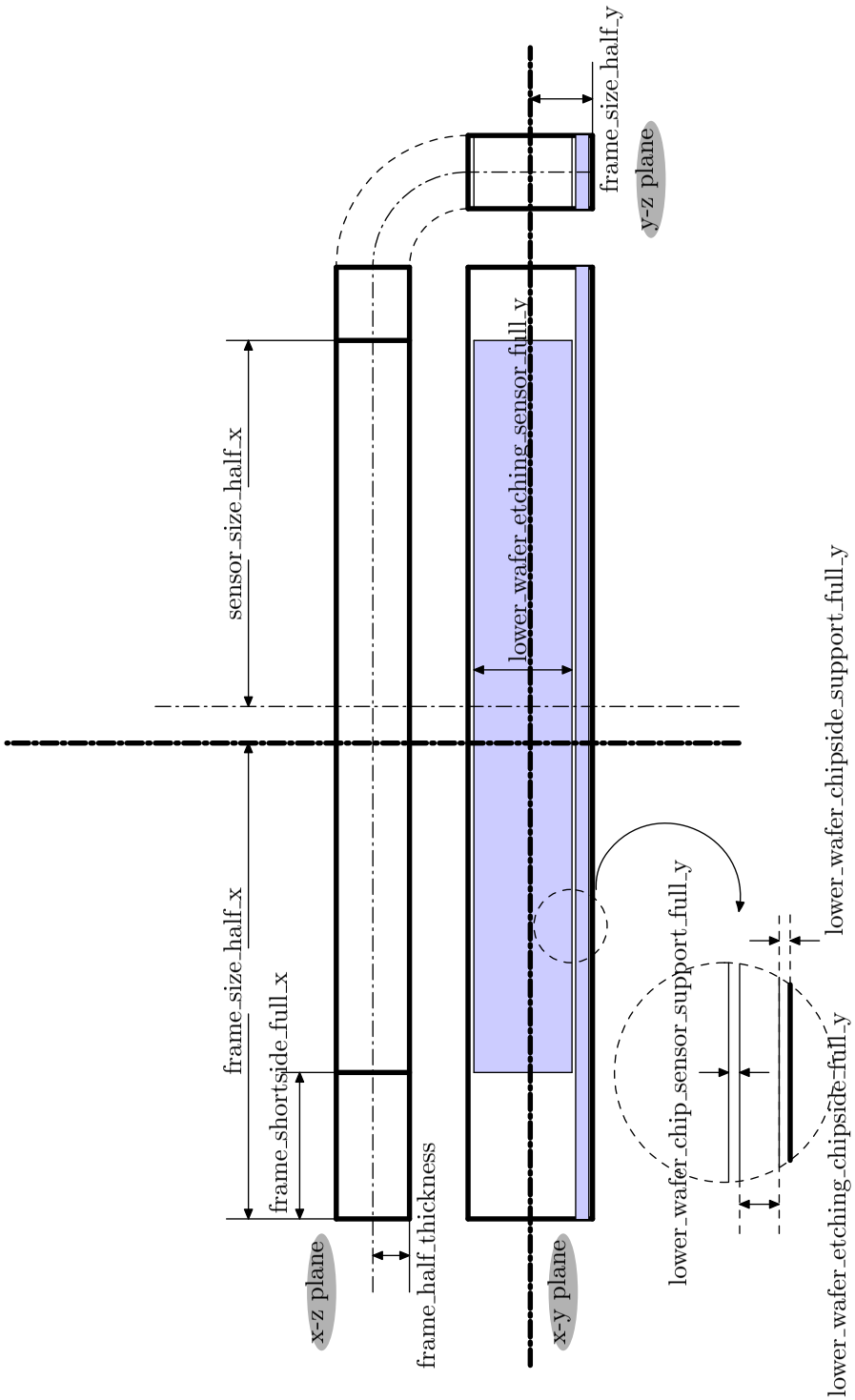

Figure A.2: The schematic view of the lower support frame.

Component	Parameter	Description
sensor	sensor_size_half_x	Half length of sensor.
	sensor_size_half_y	Half width of sensor.
	sensor_half_thickness	Half thickness of sensor.
steering chips	chip_size_half_x	Half length of chips.
	chip_size_half_y	Half width of steering chips.
	chip_half_thickness	Half thickness of steering chips.
support frames	frame_size_half_x	Half length of support frames.
	frame_size_half_y	Half width of support frames.
	frame_chipside_half_y	Half distances from the long edge of sensor to the edge of frames in the side where chips are placed.
	frame_shortside_full_x	Distance from the short edge of sensor to the edge of frames.
	frame_half_thickness	Half thickness of the lower support frame.
	lower_wafer_etching_sensor_full_y	Full width of the wider etching hole in the support frame.
	lower_wafer_chip_sensor_support_full_y	Distance between two etching holes in the lower support frame in y direction.
	lower_wafer_etching_chipside_full_y	Full width of the narrower etching hole in the support frame.
	lower_wafer_chipside_support_full_y	Distance from the edge of narrower etching hole to the edge of lower support frame.

Table A.1: The parameters used to define the geometry of a DEPFET ladder.

Appendix B

Using ISAJET in a PYTHIA based event generator

This Appendix is about the installation and use of ISAJET in PYTHIA based event generator for the production of SUSY events. PYTHIA version 6.4 and ISAJET version 7.75 are used by default.

In general, user's own event generator is always based on PYTHIA . PYTHIA has an interface enabling the user's program to call the ISAJET routines for SUSY generation. That is done by substituting some of the PYTHIA libraries with ISAJET libraries.

B.1 Compilation of ISAJET

The first step is to build ISAJET . The newest version can be found in `http://www.hep.fsu.edu/~isajet/`. The patchy source file `isajet.car` and the `Makefile` should be downloaded to build the library.

The Makefile may be edited according to the compiler and libraries in the system. Then enter

```
make libisajet.a
```

to start compiling. The result of compiling is a static library `libisajet.a`. Three object files should be extracted from the library archive by using the

```
ar x libisajet.a visaje.o
ar x libisajet.a sugra.o
ar x libisajet.a ssmssm.o
```

commands. These files will be used to replace the files with same names in the PYTHIA library.

B.2 Compilation of PYTHIA

For PYTHIA 6.4, routines are placed in different files. So we can delete three files from PYTHIA source tree, named `visaje.f, sugra.f` and `ssmssm.f`. Then we can compile the rest file to get the PYTHIA library by typing

```
make lib
```

The static library `libpythia.a` will be obtained. After that, we can insert the three object files extracted from the ISAJET library to this library with commands

```
ar r libpythia.a visaje.o
ar r libpythia.a sugra.o
ar r libpythia.a ssmssm.o
```

Now all the libraries are ready for use in the user's own generator.

B.3 Compilation of user's own generator

When compiling the user's own generator, both of the two static library files `libpythia.a` and `libisajet.a` must be linked.

B.4 Using ISAJET in the program

The interface to ISAJET can be accessed by set the option `IMSS`(1) = 12 or `IMSS`(1) = 13. If `IMSS`(1) = 12, only the mSUGRA model of ISASUSY can be accessed. The five parameters required by the mSUGRA model should be set manually. If `IMSS`(1) = 13, all the ISASUSY models can be used, but a ISAJET input file must be used to provide the parameters necessary for the initialization of ISASUSY. The detailed introduction of the parameters can be found in the PYTHIA manual.

Appendix C

Intersection of cones

C.1 Basic Formulas

This section is about the equation that defines points on a cone. In the simplest case the apex of the cone is placed at the origin and the axis of the cone is the z-axis. The equation of the point on the cone is given by

$$\begin{cases} x{=}b\tan\frac{\alpha}{2}\cos\eta \\ y{=}b\tan\frac{\alpha}{2}\sin\eta \\ z{=}b \end{cases} \tag{C.1}$$

where α is the apex angle of the cone, η and b are parameters.

Ordinary cones with apex placed at the original point can be obtained by rotating the special cone according the polar angle θ and azimuthal angle ϕ of its axis. It is done in two steps:

1. Rotate the special cone around y-axis for θ;

2. Rotate it around the z-axis for ϕ.

So the points on the cone can be described by the original parametric equation acted on by two rotation matrices,

$$\begin{pmatrix} x \\ y \\ z \end{pmatrix} = R_z(\phi)R_y(\theta)\begin{pmatrix} x_0 \\ y_0 \\ z_0 \end{pmatrix} \tag{C.2}$$

C.2 Intersection of two cones

Let's consider two cones, c_1 and c_2, whose apexes are placed at the origin. Assume that the two cones have intersections. The intersections must be two straight lines intersecting at the origin. We want to know the polar angles and the azimuthal angles of the two lines. This can be done by finding one point (except the origin itself) on the line. As the point is on both cones, we have a relation not regarding the orientation of the axis,

$$\frac{b_1}{\cos\frac{\alpha_1}{2}} = \frac{b_2}{\cos\frac{\alpha_2}{2}} \tag{C.3}$$

By taking b_1 to be 1, we have

$$b_2 = \frac{\cos\frac{\alpha_2}{2}}{\cos\frac{\alpha_1}{2}}. \tag{C.4}$$

To simplify the calculation, we can rotate both of the cones by making the axis of cone c_1 coincide with z-axis. That is the reverse rotation to that defined by Eq. C.2. Then the equation of the points on c_1 have the simple form given by Eq. C.1. But for the points on c_2, the points are given by

$$\begin{pmatrix} x_2 \\ y_2 \\ z_2 \end{pmatrix} = R_y(-\theta_1)R_z(\phi_2 - \phi_1)R_y(\theta_2) \begin{pmatrix} x_{02} \\ y_{02} \\ z_{02} \end{pmatrix} \tag{C.5}$$

Then we can extract the points by solving the equation

$$R \begin{pmatrix} \frac{\cos\frac{\alpha_2}{2}}{\cos\frac{\alpha_1}{2}} \tan\frac{\alpha_2}{2}\cos\eta_2 \\ \frac{\cos\frac{\alpha_2}{2}}{\cos\frac{\alpha_1}{2}} \tan\frac{\alpha_2}{2}\sin\eta_2 \\ \frac{\cos\frac{\alpha_2}{2}}{\cos\frac{\alpha_1}{2}} \end{pmatrix} = \begin{pmatrix} \tan\frac{\alpha_1}{2}\cos\eta_1 \\ \tan\frac{\alpha_1}{2}\sin\eta_1 \\ 1 \end{pmatrix} \tag{C.6}$$

where R is the rotation matrix, and η_1 and η_2 are values we desired.

η_2 can be solved from the equation

$$R_{31}\frac{\cos\frac{\alpha_2}{2}}{\cos\frac{\alpha_1}{2}}\tan\frac{\alpha_2}{2}\cos\eta_2 + R_{32}\frac{\cos\frac{\alpha_2}{2}}{\cos\frac{\alpha_1}{2}}\tan\frac{\alpha_2}{2}\sin\eta_2 + R_{33}\frac{\cos\frac{\alpha_2}{2}}{\cos\frac{\alpha_1}{2}} = 1, \tag{C.7}$$

or

$$R_{31}\sin\frac{\alpha_2}{2}\cos\eta_2 + R_{32}\sin\frac{\alpha_2}{2}\sin\eta_2 + R_{33}\cos\frac{\alpha_2}{2} - \cos\frac{\alpha_1}{2} = 0. \tag{C.8}$$

It has the form of

$$G\cos\eta_2 + H\sin\eta_2 + I = 0. \tag{C.9}$$

If $H = 0$, we have $\cos\eta_2 = -I/G$, and $\sin\eta_2 = \pm\sqrt{1-\cos^2\eta_2}$. If $H \neq 0$, we have

$$(G^2 + H^2)\cos^2\eta_2 + 2GI\cos\eta_2 + I^2 - H^2 = 0. \tag{C.10}$$

The equation has two solutions. The positions of the two points can be obtained by substituting the results in the parametric equation Eq. C.2.

Bibliography

[1] **NLC ZDR Design Group and NLC Physics Working Group** Collaboration, S. Kuhlman *et al.*, *Physics and technology of the Next Linear Collider: A Report submitted to Snowmass '96*, hep-ex/9605011.

NLC Collaboration, N. Phinney *et al.*, *2001 report on the Next Linear Collider: A report submitted to Snowmass '01*, . Prepared for APS / DPF / DPB Summer Study on the Future of Particle Physics (Snowmass 2001), Snowmass, Colorado, 30 Jun - 21 Jul 2001.

[2] *GLC project: Linear collider for TeV physics*, . KEK-REPORT-2003-7.

[3] e. . Richard, F., e. . Schneider, J. R., e. . Trines, D., and e. . Wagner, A., *TESLA Technical Design Report Part I: Executive Summary*, hep-ph/0106314.

ECFA/DESY LC Physics Working Group Collaboration, J. A. Aguilar-Saavedra *et al.*, *TESLA Technical Design Report Part III: Physics at an e+e- Linear Collider*, hep-ph/0106315.

e. . Behnke, T., e. . Bertolucci, S., e. . Heuer, R. D., and e. . Settles, R., *TESLA Technical Design Report. Pt. IV: A detector for TESLA*, . DESY-01-011, ECFA-2001-209.

[4] J. E. Augustin *et al.*, *Linear Collider, Final International Technology Recommendation Panel report*, 2004. http://www.fnal.gov/directorate/icfa/ITRP_Report_Final.pdf.

[5] R. Heuer, *Parameters for the Linear Collider*, 2003. http://www.fnal.gov/directorate/icfa/LC_parameters.pdf.

[6] e. . Brau, James *et al.*, *International Linear Collider Reference Design Report. 1: Executive summary. 2: Physics at the ILC. 3: Accelerator. 4: Detectors*, 2007. ILC-REPORT-2007-001.

[7] T. Abe *et al.*, *SiD detector outline document*, 2006. Link from http://hep.uchicago.edu/∼oreglia/siddod.pdf.

[8] http://www.ilcild.org.

[9] http://www.4thconcept.org.

[10] P. Fischer *et al.*, *A DEPFET based pixel vertex detector for the detector at TESLA*, . LC-DET-2002-004.

[11] P. W. Higgs, *Broken symmetries and the masses of gauge bosons*, *Phys. Rev. Lett.* **13** (1964) 508–509.

P. W. Higgs, *Spontaneous Symmetry Breakdown Without Massless Bosons*, *Phys. Rev.* **145** (1966) 1156–1163.

F. Englert and R. Brout, *Broken symmetry and the mass of gauge vector mesons*, *Phys. Rev. Lett.* **13** (1964) 321–322.

G. S. Guralnik, C. R. Hagen, and T. W. B. Kibble, *Global conservation laws and massless particles*, *Phys. Rev. Lett.* **13** (1964) 585–587.

[12] S. Weinberg, *Implications of Dynamical Symmetry Breaking*, *Phys. Rev.* **D13** (1976) 974–996.

S. Weinberg, *Implications of Dynamical Symmetry Breaking: An Addendum*, *Phys. Rev.* **D19** (1979) 1277–1280.

E. Gildener, *Gauge Symmetry Hierarchies*, *Phys. Rev.* **D14** (1976) 1667.

L. Susskind, *Dynamics of Spontaneous Symmetry Breaking in the Weinberg- Salam Theory*, *Phys. Rev.* **D20** (1979) 2619–2625.

e. . 't Hooft, Gerard *et al.*, *Recent Developments in Gauge Theories. Proceedings, Nato Advanced Study Institute, Cargese, France, August 26 - September 8, 1979*, . New York, Usa: Plenum (1980) 438 P. (Nato Advanced Study Institutes Series: Series B, Physics, 59).

[13] A. Djouadi *et al.*, *International Linear Collider Reference Design Report Volume 2: PHYSICS AT THE ILC*, arXiv:0709.1893 [hep-ph].

[14] **LHC/LC Study Group** Collaboration, G. Weiglein *et al.*, *Physics interplay of the LHC and the ILC*, *Phys. Rept.* **426** (2006) 47–358, [hep-ph/0410364].

[15] A. Djouadi, *The anatomy of electro-weak symmetry breaking. I: The Higgs boson in the standard model*, *Phys. Rept.* **457** (2008) 1–216, [hep-ph/0503172].

[16] **LEP Working Group for Higgs boson searches** Collaboration, R. Barate *et al.*, *Search for the standard model Higgs boson at LEP*, *Phys. Lett.* **B565** (2003) 61–75, [hep-ex/0306033].

[17] **LEP** Collaboration, J. Alcaraz *et al.*, *Precision Electroweak Measurements and Constraints on the Standard Model*, 0712.0929.

[18] **Particle Data Group** Collaboration, W. M. Yao *et al.*, *Review of particle physics*, *J. Phys.* **G33** (2006) 1–1232.

[19] B. W. Lee, C. Quigg, and H. B. Thacker, *Weak Interactions at Very High-Energies: The Role of the Higgs Boson Mass*, *Phys. Rev.* **D16** (1977) 1519.

[20] J. R. Ellis, M. K. Gaillard, and D. V. Nanopoulos, *A Phenomenological Profile of the Higgs Boson*, *Nucl. Phys.* **B106** (1976) 292.

J. D. Bjorken, *Weak Interaction Theory and Neutral Currents*, 1976. in Proc. of Summer Inst. on Particle Physics, Stanford, Calif., SLAC Report 198.

B. L. Ioffe and V. A. Khoze, *What Can Be Expected from Experiments on Colliding e+ e- Beams with e Approximately Equal to 100-GeV?*, *Sov. J. Part. Nucl.* **9** (1978) 50.

D. R. T. Jones and S. T. Petcov, *Heavy Higgs Bosons at LEP*, *Phys. Lett.* **B84** (1979) 440.

[21] R. N. Cahn and S. Dawson, *Production of Very Massive Higgs Bosons*, *Phys. Lett.* **B136** (1984) 196.

K.-i. Hikasa, *HEAVY HIGGS PRODUCTION IN e+ e- AND e- e- COLLISIONS*, *Phys. Lett.* **B164** (1985) 385.

G. Altarelli, B. Mele, and F. Pitolli, *Heavy Higgs Production at Future Colliders*, *Nucl. Phys.* **B287** (1987) 205–224.

W. Kilian, M. Krämer, and P. M. Zerwas, *Higgs-strahlung and WW fusion in* $e\ +e\ -$ *collisions*, *Phys. Lett.* **B373** (1996) 135–140, [hep-ph/9512355].

[22] K. J. F. Gaemers and G. J. Gounaris, *Bremsstrahlung production of higgs bosons in* e^+e^- *collisions*, *Phys. Lett.* **B77** (1978) 379.

A. Djouadi, J. Kalinowski, and P. M. Zerwas, *Higgs radiation off top quarks in high-energy* e^+e^- *colliders*, *Z. Phys.* **C54** (1992) 255–262.

A. Djouadi, J. Kalinowski, and P. M. Zerwas, *Measuring the* $Ht\bar{t}$ *coupling in* e^+e^- *collisions*, *Mod. Phys. Lett.* **A7** (1992) 1765–1769.

[23] G. J. Gounaris, D. Schildknecht, and F. M. Renard, *Test of Higgs boson nature in* $e^+e^- \to HHZ$, *Phys. Lett.* **B83** (1979) 191.

V. D. Barger, K.-m. Cheung, A. Djouadi, B. A. Kniehl, and P. M. Zerwas, *Higgs bosons: Intermediate mass range at* e^+e^- *colliders*, *Phys. Rev.* **D49** (1994) 79–90, [hep-ph/9306270].

V. A. Ilyin, A. E. Pukhov, Y. Kurihara, Y. Shimizu, and T. Kaneko, *Probing the H**3 vertex in e+ e-, gamma e and gamma gamma collisions for light and intermediate Higgs bosons*, *Phys. Rev.* **D54** (1996) 6717–6727, [hep-ph/9506326].

A. Djouadi, H. E. Haber, and P. M. Zerwas, *Multiple Production of MSSM Neutral Higgs Bosons at High– Energy* $e\ +e\ -$ *Colliders*, *Phys. Lett.* **B375** (1996) 203–212, [hep-ph/9602234].

[24] D. J. Miller, S. Y. Choi, B. Eberle, M. M. Muhlleitner, and P. M. Zerwas, *Measuring the spin of the Higgs boson*, *Phys. Lett.* **B505** (2001) 149–154, [hep-ph/0102023].

[25] M. Krämer, J. H. Kühn, M. L. Stong, and P. M. Zerwas, *Prospects of measuring the parity of Higgs particles*, *Z. Phys.* **C64** (1994) 21–30, [hep-ph/9404280].

[26] A. Djouadi, *The anatomy of electro-weak symmetry breaking. II: The Higgs bosons in the minimal supersymmetric model*, *Phys. Rept.* **459** (2008) 1–241, [hep-ph/0503173].

[27] S. Heinemeyer, W. Hollik, and G. Weiglein, *Electroweak precision observables in the minimal supersymmetric standard model*, *Phys. Rept.* **425** (2006) 265–368, [hep-ph/0412214].

[28] J. R. Espinosa and M. Quiros, *Gauge unification and the supersymmetric light Higgs mass*, *Phys. Rev. Lett.* **81** (1998) 516–519, [hep-ph/9804235].

[29] Y. A. Gol'fand and E. P. Likhtman, *Extension of the Algebra of Poincare Group Generators and Violation of p Invariance*, *JETP Lett.* **13** (1971) 323–326.

J. Wess and B. Zumino, *Supergauge Transformations in Four-Dimensions*, *Nucl. Phys.* **B70** (1974) 39–50.

[30] J. Wess and J. Bagger, *Supersymmetry and supergravity*, . Princeton, USA: Univ. Pr. (1992) 259 p.

[31] H. P. Nilles, *Supersymmetry, Supergravity and Particle Physics*, *Phys. Rept.* **110** (1984) 1–162.

H. E. Haber and G. L. Kane, *The Search for Supersymmetry: Probing Physics Beyond the Standard Model*, *Phys. Rept.* **117** (1985) 75–263.

S. P. Martin, *A supersymmetry primer*, hep-ph/9709356.

M. Drees, R. Godbole, and P. Roy, *Theory and phenomenology of sparticles: An account of four-dimensional N=1 supersymmetry in high energy physics*, . Hackensack, USA: World Scientific (2004) 555 p.

[32] P. Fayet, *Spontaneously Broken Supersymmetric Theories of Weak, Electromagnetic and Strong Interactions*, *Phys. Lett.* **B69** (1977) 489.

G. R. Farrar and P. Fayet, *Phenomenology of the Production, Decay, and Detection of New Hadronic States Associated with Supersymmetry*, *Phys. Lett.* **B76** (1978) 575–579.

[33] A. H. Chamseddine, R. Arnowitt, and P. Nath, *Locally Supersymmetric Grand Unification*, *Phys. Rev. Lett.* **49** (1982) 970.

R. Barbieri, S. Ferrara, and C. A. Savoy, *Gauge Models with Spontaneously Broken Local Supersymmetry*, *Phys. Lett.* **B119** (1982) 343.

L. J. Hall, J. D. Lykken, and S. Weinberg, *Supergravity as the Messenger of Supersymmetry Breaking*, *Phys. Rev.* **D27** (1983) 2359–2378.

[34] B. C. Allanach *et al.*, *The Snowmass points and slopes: Benchmarks for SUSY searches*, in *APS / DPF / DPB Summer Study on the Future of Particle Physics (Snowmass 2001)*, 2002. hep-ph/0202233.

[35] R. Hawkings and K. Monig, *Electroweak and CP violation physics at a linear collider Z-factory*, *Eur. Phys. J. direct* **C1** (1999) 8, [hep-ex/9910022].

[36] T. Behnke *et al.*, *ILC Reference Design Report Volume 4 - Detectors*, arXiv:0712.2356 [physics.ins-det].

[37] E. Boos, V. Ilyin, A. Pukhov, M. Sachwitz, and H. Schreiber, *Branching Fraction Measurements of the SM Higgs with a Mass of 160 GeV at Future e^+e^- Colliders*, . LC-PHSM-2000-035.

[38] H.-J. Yang and K. Riles, *Impact of tracker design on Higgs and slepton measurements*, physics/0506198.

[39] T. Barklow, *Physics Impact of Detector Performance*, 2005. in LCWS05, Stanford.

[40] **ACFA Linear Collider Working Group** Collaboration, K. Abe *et al.*, *Particle physics experiments at JLC*, hep-ph/0109166.

[41] **American Linear Collider Working Group** Collaboration, T. Abe *et al.*, *Linear collider physics resource book for Snowmass 2001. 4: Theoretical, accelerator, and experimental options*, hep-ex/0106058.

[42] I. G. Knowles and G. D. Lafferty, *Hadronization in Z0 decay*, *J. Phys.* **G23** (1997) 731–789, [hep-ph/9705217].

[43] M. G. Green, S.L., Lloyd, P. Ratoff, and D. Ward, *Electron-positron physics at the Z*. Institute of Physics Publishing, 1998.

[44] M. A. Thomson, *Particle flow calorimetry at the ILC*, *AIP Conf. Proc.* **896** (2007) 215–224.

[45] M. A. Thomson, *Progress with Particle Flow Calorimetry*, 0709.1360.

[46] T. Behnke *et al.*, *The LDC detector concept*, *Pramana* **69** (2007) 697–702.

[47] **GLD Concept Study Group** Collaboration, K. Abe *et al.*, *GLD detector outline document*, physics/0607154.

[48] A. Herve *et al.*, *Status of the CMS magnet*, . Prepared for 17th International Conference on Magnet Technology (MT-17), Geneva, Switzerland, 24-28 Sep 2001.

[49] L. Andriček *et al.*, *DEPFET Pixel Vertex Detector for the ILC*, . ILC VXD Review, FNAL.

[50] J. Kemmer and G. Lutz, *New Detector Concepts*, *Nucl. Instrum. Meth.* **A253** (1987) 365–377.

[51] J. Kemmer *et al.*, *Experimental confirmation of a New Semiconductor Detector Principle*, *Nucl. Instrum. Meth.* **A288** (1990) 92–98.

[52] W. Neeser *et al.*, *The DEPFET pixel BIOSCOPE*, *IEEE Trans. Nucl. Sci.* **47 No.3** (2000) 1246–1250.

[53] C. Sandow *et al.*, *Clear-performance of linear DEPFET devices*, *Nucl. Instrum. Meth.* **A568** (2006) 176–180.

[54] F. Gaede, T. Behnke, N. Graf, and T. Johnson, *LCIO: A persistency framework for linear collider simulation studies*, physics/0306114.

[55] P. Mora De Freitas and H. Videau, *Detector simulation with Mokka/GEANT4: present and future*, . LC-TOOL-2003-010.

[56] http://polzope.in2p3.fr:8081/MOKKA.

[57] **GEANT4** Collaboration, S. Agostinelli *et al.*, *GEANT4: A simulation toolkit*, *Nucl. Instrum. Meth.* **A506** (2003) 250–303.

[58] J. Allison *et al.*, *Geant4 developments and applications*, *IEEE Trans. Nucl. Sci.* **53** (2006) 270.

[59] F. Gaede, *Marlin and LCCD: Software tools for the ILC*, *Nucl. Instrum. Meth.* **A559** (2006) 177–180.

[60] http://ilcsoft.desy.de/portal/software_packages/gear.

[61] T. Krämer, *Track Parameters in LCIO*, . LC-DET-2006-004.

[62] O. Wendt, F. Gaede, and T. Krämer, *Event reconstruction with MarlinReco at the ILC*, physics/0702171. LC-DET-2007-001.

[63] http://www.mysql.com.

[64] T. Sjostrand, S. Mrenna, and P. Skands, *PYTHIA 6.4 physics and manual*, *JHEP* **05** (2006) 026, [hep-ph/0603175].

[65] E. . Altarelli, G., E. . Sjostrand, T., and E. . Zwirner, F., *Physics at LEP2: Vol.2*, . CERN-96-01.

[66] M. Thomson, *Particle Flow with PandoraPFA*, 2007. in LCWS07, Hamburg.

[67] M. Thomson, *LDC01Sc and PandoraPFA*, 2008. in ILD Workshop, Zeuthen.

[68] A. Raspereza, $ZH \to l^+l^-X$ *Analysis*, 2008. in ILD Workshop, Zeuthen.

[69] A. Raspereza, *Simulation Studies of VXD Performance*, 2006. in LCWS06, Bangalore.

[70] R. Kohrs *et al.*, *Development of a prototype module for a DEPFET pixel vertex detector for a linear collider*, *IEEE Trans. Nucl. Sci.* **52** (2005) 1171–1175.

[71] L. Reuen *et al.*, *Performance of a DEPFET prototype module for the ILC vertex detector*, *IEEE Trans. Nucl. Sci.* **53** (2006) 1719–1725.

[72] R. Kohrs *et al.*, *First test beam results on DEPFET pixels for the ILC*, *Nucl. Instrum. Meth.* **A565** (2006) 172–177.

[73] J. J. Velthuis *et al.*, *A DEPFET based beam telescope with submicron precision capability*, *IEEE Trans. Nucl. Sci.* **55** (2008) 662–666.

[74] J. Treis *et al.*, *A modular PC based silicon microstrip beam telescope with high speed data acquisition*, *Nucl. Instrum. Meth.* **A490** (2002) 112–123, [physics/0210004].

[75] J. Velthuis *et al.*, *Tracks in a multitrack environment*, . DEPFET Collaboration internal report.

[76] M. Mathes. PhD thesis, University of Bonn, December, 2007.

[77] A. Freitas, A. von Manteuffel, and P. M. Zerwas, *Slepton production at e^+e^- and e^-e^- linear colliders*, *Eur. Phys. J.* **C34** (2004) 487–512, [hep-ph/0310182].

[78] T. Tsukamoto, K. Fujii, H. Murayama, M. Yamaguchi, and Y. Okada, *Precision study of supersymmetry at future linear e^+e^- colliders*, *Phys. Rev.* **D51** (1995) 3153–3171.

[79] H.-U. Martyn, *Study of Sleptons - Supersymmetry Scenario SPS 1*, . LC-PHSM-2003-071.

[80] N. Phinney, *ILC reference design report: Accelerator executive summary*, *ICFA Beam Dyn. Newslett.* **42** (2007) 7–29.

[81] M. Jimbo, *Study of slepton pair production with polarized e^- beams at future colliders*, . TMCP-92-1.

[82] F. E. Paige, S. D. Protopopescu, H. Baer, and X. Tata, *ISAJET 7.69: A Monte Carlo event generator for pp, anti-p p, and e^+e^- reactions*, hep-ph/0312045.

[83] H. Baer, F. E. Paige, S. D. Protopopescu, and X. Tata, *Simulating supersymmetry with ISAJET 7.0 / ISASUSY 1.0*, hep-ph/9305342.

[84] N. Ghodbane and H.-U. Martyn, *Compilation of SUSY particle spectra from Snowmass 2001 benchmark models*, hep-ph/0201233.

[85] T. Ohl, *CIRCE version 1.0: Beam spectra for simulating linear collider physics*, *Comput. Phys. Commun.* **101** (1997) 269–288, [hep-ph/9607454].

List of Figures

List of Tables

Acknowledgements

It is my pleasure to express my thanks to who supported me during the past three years of my PhD work.

First of all, I would like to thank my official supervisor Prof. Allen Caldwell for offering me the opportunity to work in the ILC project. I benefitted a lot from his lectures on statistics and computational physics.

I also would thank my day-to-day supervisor Dr. Ariane Frey for suggesting the topic of my thesis, for her continuous support and encouragement. Her advice is of great help in my work.

I'm extremely grateful to Dr. Aliaksei Raspiareza for sharing his research experience. I learned a lot from the helpful discussions covering almost all the topics of HEP experiments.

Special thanks go to all the members of the ILC-DEPFET collaboration, in particular to Dr. Jaap Velthuis, Robert Kohrs and Lars Reuen for their help in the DEPFET test beam analysis, and to Dr. Hans-Günther Moser and Ladislav Andricek for the constructive discussions at our group meeting.

I would like to thank Dr. Hans-Ulrich Martyn for his warmhearted reply to my questions in the research. The reply has been crucial in the analysis of smuon productions.

I would like to thank Andreas Moll for helping me to translate the abstract of this thesis to German.

I wish to thank all the people who are working for the IMPRS program, especially Dr. Jochen Schieck, Dr. Frank Steffen and Ms. Franziska Rudert, for their hard work in organizing the nice lectures, workshops and summer schools of IMPRS.

I would thank Vasiliy Lvovich Morgunov for his encouragement when I was dispirited at the death of my grandmother.

I'm indebted to my housemate Zhang Jianhui for our discussions in theoretical physics. The constructive discussions help me deepen my understanding of nature.

I must say thanks to all my friends from inside and outside the institute, especially to Yuan Jianming and Liu Xiang, who made my life in Munich more enjoyable.

At the last, I want to thank my mother and grandmother with deep sorrow. They passed by in the last two years. Without their unconditional love and support, it would have been impossible for me to have the chance to start my thesis.